Development of Micro-machined Microwave and Terahertz Antennas

A Dissertation

Presented to

The faculty of the School of Engineering and Applied Science

University of Virginia

In Partial Fulfillment

Of the requirements for the degree of

Doctor of Philosophy of Electrical Engineering

By

Yuxin Wang

Dec 2022

APPROVAL SHEET

This

Dissertation

is submitted in partial fulfillment of the requirements
for the degree of

Doctor of Philosophy

Author: Yuxin Wang 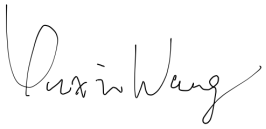

This Dissertation has been read and approved by the examing committee:

Advisor: N. Scott Barker

Advisor:

Committee Member: Robert M. Weikle, II

Committee Member: Arthur W. Lichtenberger

Committee Member: Steve M. Bowers

Committee Member: Brad Campbell

Committee Member:

Committee Member:

Accepted for the School of Engineering and Applied Science:

Jennifer L. West, School of Engineering and Applied Science

December 2022

Dedication

To my families and friends, who always encouraged and supported me.

Abstract

Nowadays, antennas at microwave and terahertz frequencies are used in various applications, such as mobile phones, communication systems on aircraft, ships and vehicles, medical applications, remote sensing, and so on. Therefore, demands on antenna design like small physical size, low weight, wideband and multiband, reconfigurable capabilities are increasingly required. Micro-machined technology can satisfy the needs of modern antenna designs.

This work discusses two antenna designs, micro-machined 3D foldable antenna and micro-machined THz antennas. The research in this work is to create antennas needed to extend the capabilities of existing wireless systems and provide them access to the Terahertz region of the spectrum. The core contribution of this work is using micro-machining techniques to create antennas for high-frequency applications, improve antenna performance and develop antenna integration methods.

This dissertation first shows a 3D cube antenna at 10 GHz using a silicon-based micro-machined fabrication method in which the 3D cubic shape allows IC packaging inside the cube's hollow interior. The 3D structure is also beneficial in opening up the internal volume for other uses, such as storage for batteries. Next, this dissertation shows the HFSS simulation and micro-machined fabrication processing for the 3D antenna and measures the antenna performance, including return loss, gain, radiation pattern, and efficiency.

The second part of the dissertation designs silicon-based micro-machined THz antennas integrated with waveguide and probe housing at WR 6.5 (110-170 GHz) and WR 2.2 (325-500 GHz). These antennas are fabricated on a silicon-on-insulator (SOI) substrate with a 15-μm thick

device layer for substrate modes reduction. The antenna geometry is integrated with the waveguide by the E-plane probe for THz antenna measurement and over-the-air (OTA) measurement. Simulation and measurement can demonstrate that the 15-μm SOI is a good platform for packaging and antenna integration for millimeter-wave and THz ICs. Besides, the geometry with T-wave probe housing is an integration solution with waveguide-fed devices for antenna measurement and OTA measurement. Using a single probe housing with different types of the antenna chips, the geometry in this work can generate different far fields based on variable demands using a single probe housing.

Acknowledgments

First, I would like to express my sincere gratitude to my advisor Prof. Barker for this continuous support of my study and related research in my master program and PhD program, for his patience, motivation, and immense knowledge. His guidance helped me in all the time of research from 2015 to 2022. I could not have imagined having a better advisor and mentor for my PhD study.

My sincere thanks also go to Prof. Weikle and Dr. Lichtenberger, who provided valuable support and suggestions. Through weekly group meetings, they both have advised me a lot in terms of doing research and helped me accomplish much in every way.

Additionally, I'd like to thank other staff, graduate students and friends who helped me generously in my research group and other groups: Michael Cyberey, Matthew Bauwens, Yukang Feng, Hanyu Tsao, Linli Xie, Christopher Moore, Dustin Widmann, Michael Eller, Noah Sauber, Zahraa Rizk, Keye Sun, Jizhao Zang, Qinglong Li, Yang Shen, Yiwei Peng, Dekang Chen, Keyu Man, Bowen Lu, and Allen Zou.

Last but not the least, I would like to thank my cat, Guldan, and my parents, Xin Zhang and Yunfei Wang, for supporting me spiritually throughout writing this thesis and my life in general.

Contents

List of Figures

List of Tables

Chapter 1

1. Introduction

The terahertz frequency band is generally defined at the 0.1-10 THz frequency band with a wavelength of 0.03-3 mm. According to the IEEE standard, the THz wave is defined at 0.3-10 THz [1]. Figure 1.1 shows that the THz band is between microwaves and infrared light [2]. THz frequencies have excellent characteristics, such as wide available bandwidth. For example, if the THz wave can be used as the signal carrier transmitted by the antennas, the information transfer rate may reach a new level, even at Tbps [3]. In addition, THz waves have advantages over millimeter waves and light waves. Compared to millimeter waves, the usable frequency band is wider, and the confidentiality and anti-interference performance is better. Compared to light waves, the penetration of THz waves is stronger [4]. Thus, based on the THz waves' unique characteristics, the THz antennas' best performance is their wide operating bandwidth.

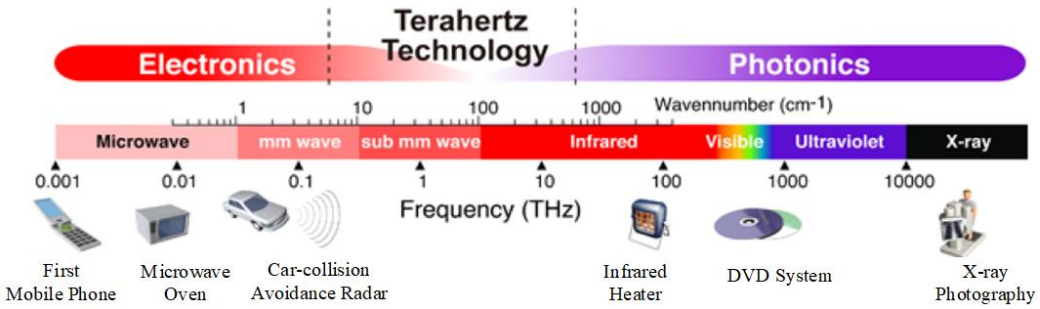

Figure 1.1 The position of the THz wave in the electromagnetic spectrum [2].

1.1 Terahertz Technology and Applications

The application space of the Terahertz frequency band is widening as more interested groups are joining the research efforts. All these applications are linked by the characteristics of the Terahertz band, such as wide bandwidth. Figure 1.2 shows these applications, including imaging, spectroscopy, material characterization, and communication.

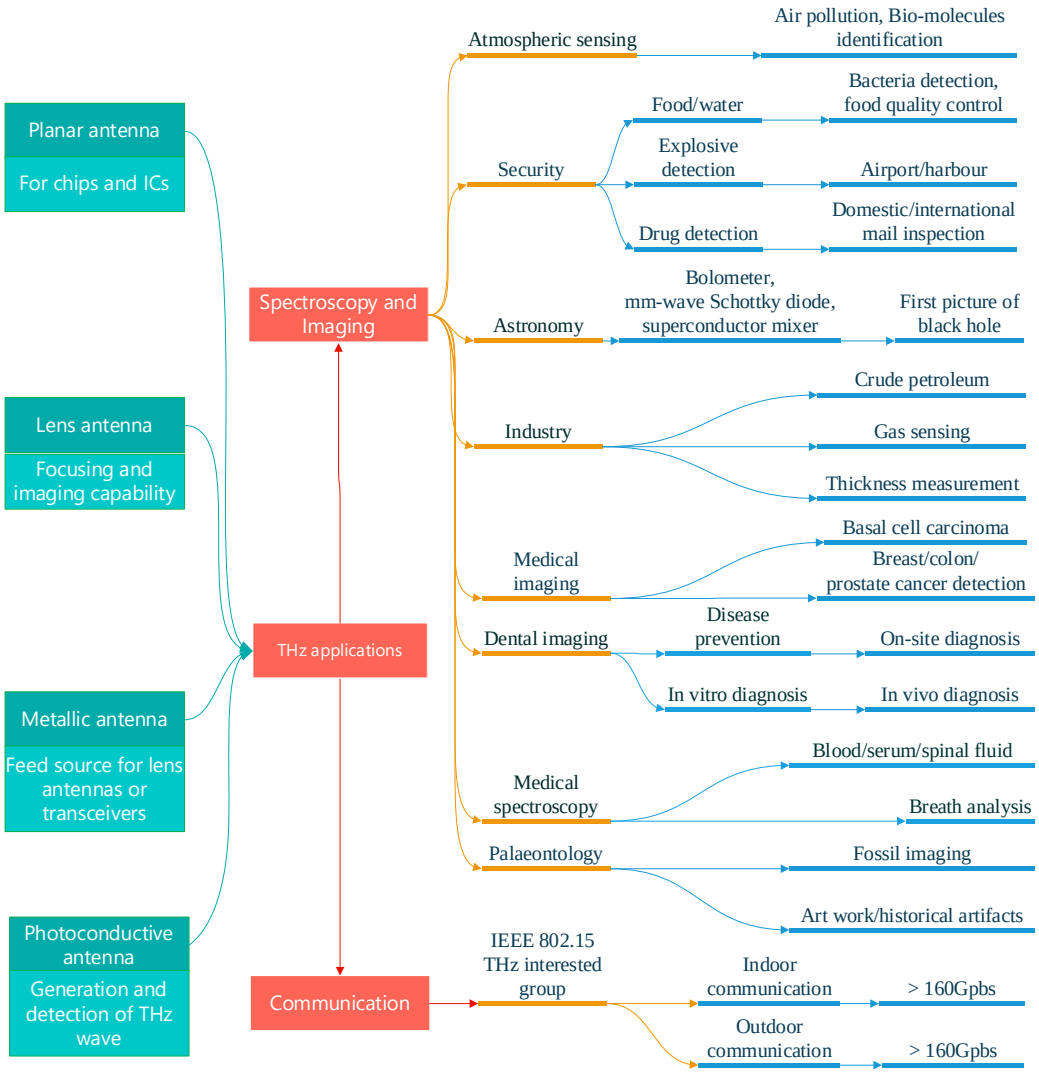

Figure 1.2 THz applications categories.

THz technology brings a significant advantage to communication because the increasing demand for unoccupied bandwidth for wireless communication systems leads to extending operation frequencies toward the THz frequency range [5]. For example, the bandwidth is as wide as 2 GHz in the 245 GHz band, while in the 2.45 GHz ISM band, the allocated bandwidth is merely 100 MHz [6]. To support THz technology research, the Institute of Electrical and Electronics Engineers (IEEE) created standards, including IEEE802.15, for various THz communication systems in 2007 [7]. Due to the availability of larger bandwidths at these frequencies, high-performance point-to-point wireless connections can benefit for communication in rural areas, communication between buildings during disasters, and high-data-rate delivery for uncompressed video. Now data rates reaching 100 Gbps or higher have been demonstrated with several potential device technologies, including not only III-V heterojunction bipolar transistors (HBTs) and high-electron-mobility transistors (HEMTs) but also silicon complementary metal-oxide-semiconductor (CMOS) and photonic transmitters [8].

There are three typical design approaches for THz communication transmitters. (1) All electronics method: The THz signals are generated by multiplying the output of a Gunn diode oscillator or a synthesized microwave generator at 30-100 GHz [9]. The average output power of a few tens of microwatts can be achieved at 1.7 to 1.9 THz. (2) Photonic techniques: the optical signal whose intensity is first generated using infrared lasers, and then it is encoded by an electro-optic (EO) or electro-absorption (EA) modulator [10]. (3) THz lasers such as quantum cascade lasers (QCLs): the QCLs can operate at around 1 THz with low-temperature and strong magnetic field [11]. Direct modulation of the QCLs is possible at modulation frequencies of over 10 GHz [12].

There are two typical design approaches for THz communication receivers. (1) Schottky barrier diodes are used in diode detectors for the direct detection, and (2) heterodyne detection with a Schottky diode mixer and a local oscillator (LO) signal source which provides higher sensitivity [5].

THz spectroscopy and imaging are the other promising fields undergoing extensive research in recent years. The use of THz for medical and biomedical imaging has the benefits of low-energy levels of the radiation as well as high spectral resolution compared to mm-wave and microwave imaging. THz imaging has been applied to analyze breast tumors [13], skin hydration and skin cancer [14], and liver cancer [15], as shown in Figure 1.3. It was also demonstrated that THz radiation could benefit dental imaging to identify and monitor tooth-decay [16].

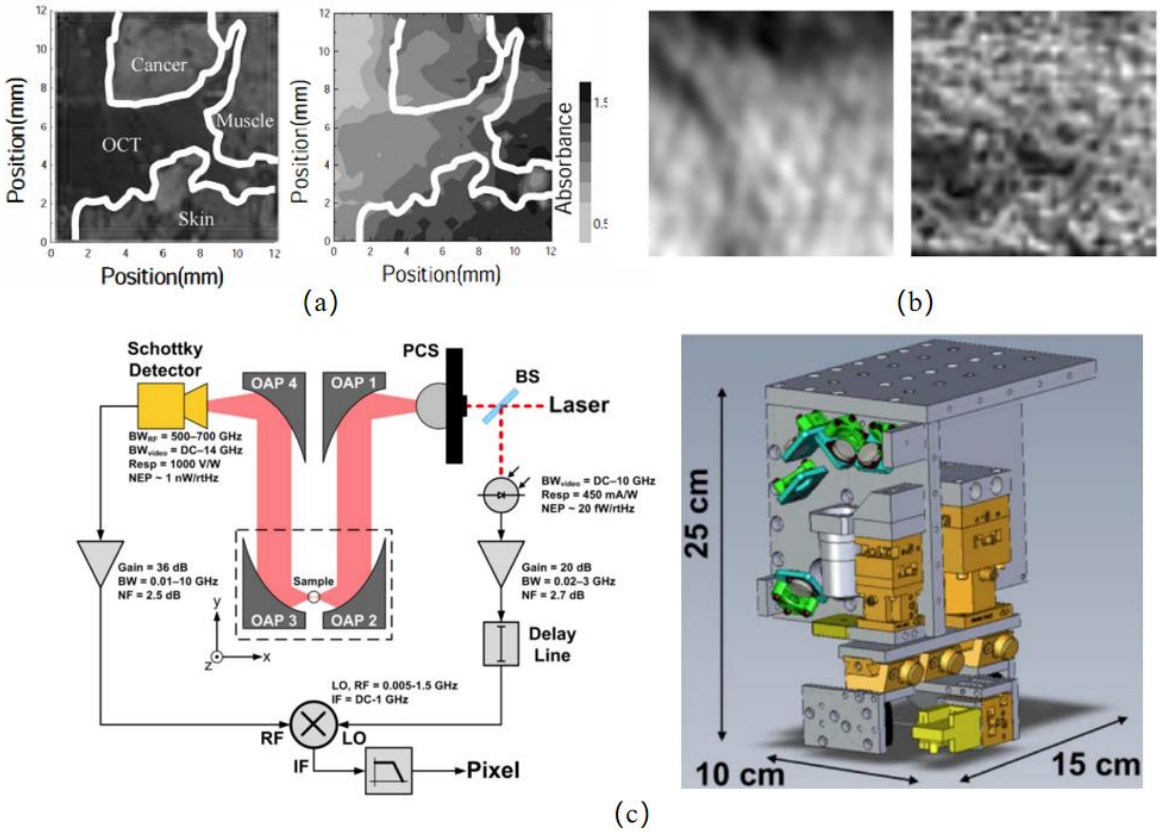

Figure 1.3 THz Spectroscopy and imaging. (a) Visible image and THz absorption image of the cancer tumor sample [11]. (b) Rough surface scattering from *ex vivo* porcine skin [14]. (c) Block diagram of the THz imaging system and its CAD model [14].

THz imaging also has excellent potential in homeland security and defense applications because THz waves can penetrate through clothing, paper, and wood. It has been demonstrated that the spectra of more than 15 explosives and related compounds have been demonstrated from 0.1 to

10 THz with use of terahertz time-domain spectroscopy (TDS) and Fourier transform infrared (FTIR) spectroscopy [17]. In addition, a 675 GHz solid-state electronic system with mechanical scanning was demonstrated for explosive detection at a stand-off distance of 25 m [18]. Due to the same reason, it also has tremendous applications in industrial quality control, electronics, food, and agricultural industry, which have currently working prototypes based on expensive optics-based THz systems [19], [20], [21], [22].

Another key application of THz system is radio astronomy. The THz spectrum contains detectable spectral lines that are important diagnostics for both the physical and chemical conditions of the gas and the sources of energy within astrophysical environments [23]. These spectral probes include rotational lines from simple molecules (e.g., CH, OH, CO, NH_3, H_2O) and the ground state fine-structure lines from abundant atoms and ions (e.g., C, C+, N+, and O) [24]. These lines are well explored in both galactic and extragalactic environments. For example, the Event Horizon Telescope collaboration captured the first Black Hole image through the THz radio telescope by the Event Horizon Telescope collaboration in 2019 [25].

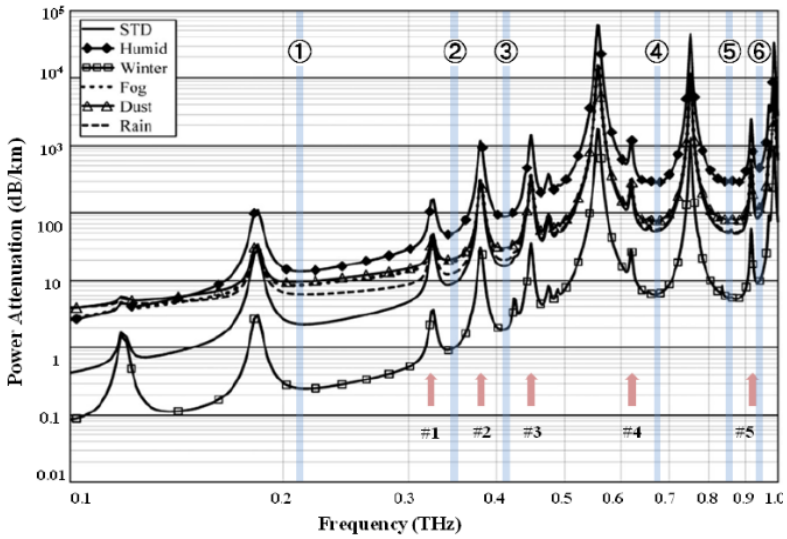

Figure 1.4 Atmospheric attenuation at sea level for different conditions such as fog, dust, rain [26]

One of the main limitations of realizing terahertz applications compared to the millimeter-wave band is the atmospheric path loss. This loss is affected by various atmospheric conditions such as rain, fog, and pollution, which affect the propagation of electromagnetic waves. Figure 1.4 shows a plot of attenuation loss (dB/km) from 100 GHz to 1000 GHz [26]. It can be noted that THz propagation is largely influenced by atmospheric conditions. However, there is less atmospheric attenuation (below 100 dB/km) at specific frequency ranges known as "windows". If a THz communication system is not designed to operate within these windows, it could be confined to indoor communication. Below 1 THz, this window appears around 220 GHz, 300 GHz, 350 GHz, 410 GHz, 650 GHz, and 850 GHz [27].

The development of most of these THz applications depends on the availability of low-cost, high-yield technology. Integrated silicon technology can provide unparalleled THz signal processing power with ultra-small form factors, high reliability, and low cost. A variety of researchers have developed new techniques to push silicon beyond its cut-off frequencies into the THz frequency spectrum [28]. Still in the early path of its growth, many papers speculate that at least a significant chunk of THz electronics will go the silicon way [29]. The goal of this thesis is to design micro-machined Si-based antennas for microwave and THz wireless systems and provide integration methods with waveguide-fed devices, semiconductor devices, and ICs.

1.2 Organization of the Dissertation

The thesis is organized as follows. Chapter 2 reviews the ever-increasing and diverse micro-machined antenna category for various demands, including beam steering, multiband, efficiency improvement, miniaturization, and integration methods, and reviews the four main types of micro-machined THz antennas: horn antennas, lens antennas, photoconductive antennas, and planar antennas. Chapter 2 also shows the previous work on 3D antenna and antenna integration methods. This dissertation develops the micro-machined antenna design, including micro-machined 3D antenna, micro-machined terahertz antenna, and antenna integration methods with ICs and waveguides.

Chapter 3 presents a 3D meandered-line foldable 3D antenna for ICs and Internet of Things (IoT) systems. This chapter discusses the 3D meandered-line dipole antenna design and simulation. This chapter also proposes the micro-machined fabrication processing for silicon-based foldable antenna geometry. The antenna measurement, including S11, gain, radiation pattern, and efficiency, is shown. The last section analyzes the measurement results and compares between the 3D antenna in this dissertation and other previous work.

Chapter 4 discusses the design of micro-machined waveguide-fed planar antennas for THz applications. Section 4.1 explains how the E-plane probes and the proposed geometry work. Next, antenna designs and simulations are shown in Section 4.2, including quasi-Yagi antennas, tapered slot antennas, and loop antennas. Section 4.3 approaches silicon and metal micro-machined processing to fabricate antennas on a thin dielectric substrate and realize substrate mode reduction. The antenna measurements and analysis are shown in Section 4.4, including return loss, gain, and radiation patterns. Finally, analysis and conclusions are drawn in Section 4.5. These antenna designs

are demonstrated as an integration method with waveguide and ICs.

In Chapter 5, conclusions are drawn for this micro-machined 3D antenna and THz antenna design. Finally, future work is discussed, including the new antenna geometry and the potential applications.

Chapter 2

2. Review of Micro-Machined Antennas

An antenna is a transitional device that forms an interface for energy traveling between a circuit and free space. Nowadays, the development of wireless communications has been an important driving force for advancing antenna technology [30]. Antennas for transceivers are used in a wide range of applications, from terminal devices, such as mobile phones, to advanced communication systems on aircraft, ships, vehicles, medical applications, remote sensing, global navigation satellite systems, and so on. Furthermore, the promise of 5G and future generation systems will expand the possibilities of mobile networks. All these aspects will put more demands on innovations in antennas.

Micro-machined fabrication is increasingly central to modern technology. It has a wide range of applications, such as micro-volume reactors, micro-electromechanical systems (MEMS), and optical components [31]. The most widely used materials for micro-machined processing are silicon, polymers, metal, and ceramics. The micro-machined processing methods include lithography, etching, bulk micro-machining, surface micro-machining, wire-bonding, etc. [32].

Demands on antenna design like small physical size, low weight, low cost, wideband and multiband, and reconfigurable capabilities are increasingly required. Micro-machined technology can satisfy the needs of modern antenna designs. As shown in Figure 2.1, Section 2.1 shows the review and development of micro-machined planar antennas in microwave and terahertz frequency

ranges based on variable demands since micro-machined technology is mainly applied to planar antennas. Section 2.2 discusses different types of micro-machined antennas widely used in the THz band. 3D antennas and foldable antennas are reviewed in Section 2.3. A review of integration methods with waveguide and ICs are respectively discussed in Sections 2.4 and 2.5. This thesis will show the development of the silicon-based micro-machined 3D cube antenna in Chapter 3 and several THz antennas, which can be integrated with waveguides using E-plane probes in Chapter 4. The antennas designed in Chapter 3 and Chapter 4 provide a good platform for packaging and antenna integration for microwave and THz ICs.

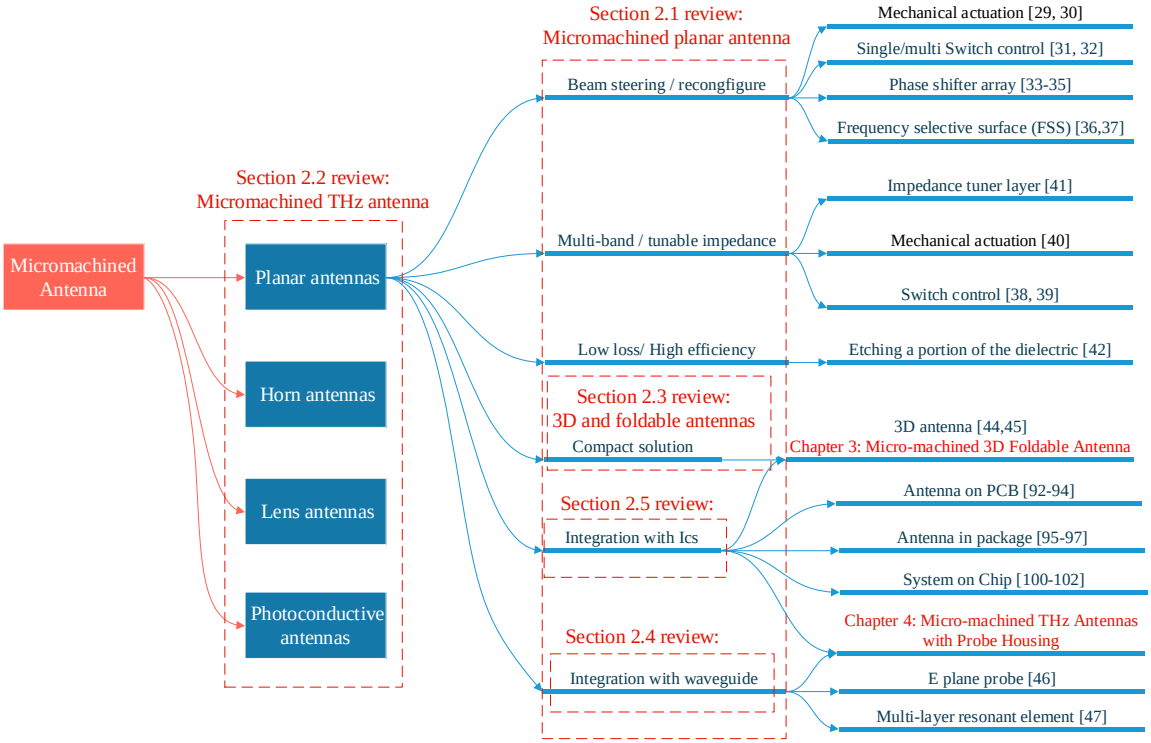

Figure 2.1 Outline of Chapter.

2.1 Review of Micro-machined Antennas

As shown in Figure 2.1, this section shows the review and development of micro-machined planar antennas based on variable demands, including beam steering, multiband, efficiency improvement, minimization, integration with ICs and waveguide.

An actuated V-band antenna array for beam steering [33] is demonstrated, with an external magnetic force being used for actuation [34], [35], shown in Figure 2.2(a). A 2 by 2 array is realized on a single platform, having two degrees of freedom of motion with the aid of orthogonal benzocyclobutene (BCB) torsion bars attached to BCB frames. Here, 40 μm thick magnetic strips are placed on the edges beneath both the antenna array and outer Silicon support frame. Using COTS solenoids, with a 700 mA bias current, a scan angle of ±20° is achieved.

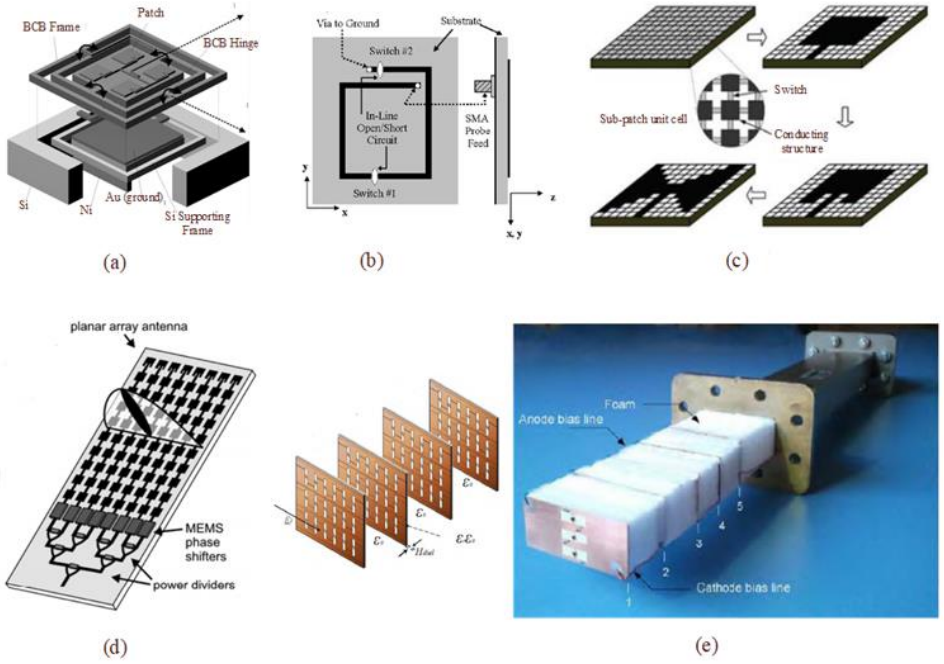

Figure 2.2 Geometry of antennas for beam steering. (a) [34], (b) [36], (c) [37], (d) [38], (e) [41].

Micro-machined switches are another solution for beam steering when designing micro-machined antennas. Paper [36] designs a microstrip spiral antenna with two switches, as shown in Figure 2.2(b). When switch one is closed while switch two is open, the antenna works at 3.7 GHz in the end-fire mode. Switching one open and two closed reconfigures the antenna to the broadside configuration working at 6 GHz. Hence it successfully demonstrates the two features of frequency and pattern reconfigurability.

Another switch method [37] on beam steering comprises some unit cells in Figure 2.2(c). A single unit cell consists of a small conducting patch of metal and four RF micro switches. The switches are used to control the flow of current to the nearest neighboring unit cell. The composite antenna can be configured to different types of antennas by switching the switch ON or OFF. MEMS can also be employed in phased array antennas [38], [39]. A more straightforward solution, see Figure 2.2(d), is to provide MEMS phase shifters and power dividers. Sometimes [40], a double-sided substrate can accommodate the patches on one side and variable phase shifters on the other.

A frequency selective surface [41], [42] for beam steering is a spatial filter that exhibits distinct resonant filtering characteristics, depending on the format and the geometries' dimensions. As a spatial filter, these structures can allow or block the propagation of an incident EM wave within a specific frequency band and then control the radiation pattern (see Figure 2.2(e)).

Switches can also be employed for multiband micro-machined antennas. Paper [43] demonstrates micro-machined MEMS switches in patch antennas designed at 10GHz, as shown in Figure 2.3(a). This antenna is connected to slots via MEMS switches and the resonant frequency changes to 12.5 GHz by actuating these switches. In another multiband method [44], the radiating structure is constant, as shown in Figure 2.3(b). Only by changing the matching, the antenna operating frequency changes from 5.2 GHz and 6.4 GHz.

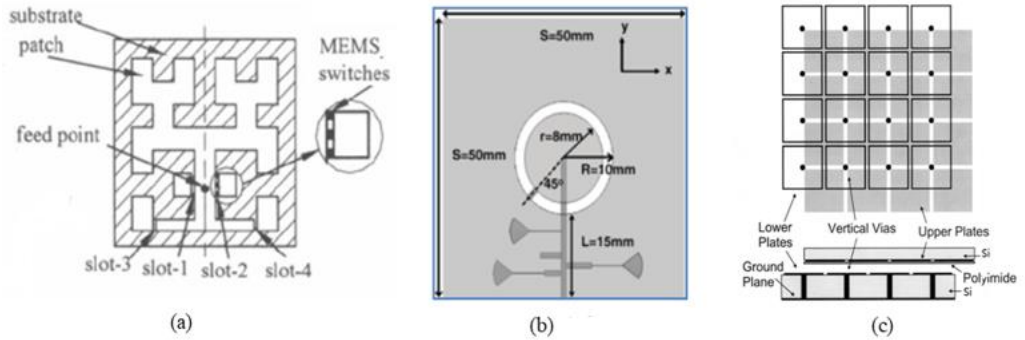

Figure 2.3 Geometry of antennas for multi-band and tunable impedance. (a) [43], (b) [44], (c) [45].

A tunable impedance surface [45] consists of two printed circuit boards: a high-impedance ground plane and a separate tuning layer. The tuning layer is moved across the stationary high-impedance surface to vary the capacitance between the overlapping plates and tune the surface's resonance frequency, as shown in Figure 2.3(c).

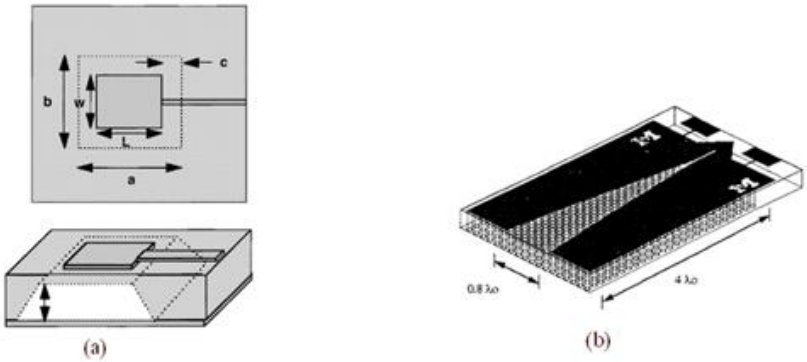

Figure 2.4 Geometry of antennas for efficiency improvement. (a) [47], (b) [48].

For low loss and high efficiency, by etching a portion of the dielectric or strategically choosing the density of via-holes underneath an antenna, a dielectric constant between 1 and ε_r can be synthesized [47]. Microstrip antennas' efficiency at 12-13 GHz has increased from 55% to 85% using such techniques (see Figure 2.4(a)). Moreover, micro-machining techniques have been used to synthesize photonic bandgap materials on high-resistivity Silicon (see Figure 2.4(b)). The holes create an “exclusion” of electromagnetic modes in the dielectric substrate, and therefore,

dramatically increase the radiation efficiency of planar antennas [48].

Because of the requirements of smaller chip sizes for antennas at GHz frequency or above, antenna designs for highly integrated chips are shifting from conventional discrete designs to antenna-in-package (AiP) solutions. Paper [49] shows an IBM 60-GHz chip using AiP. As shown in Figure 2.5(a), a three-layer cavity facilitates chip mounting and efficient utilization of available space for signal routing. The radio chip adheres to the cavity base of the package ground plane. The signals from the chip are connected to the antenna through bondwires in a GSG configuration.

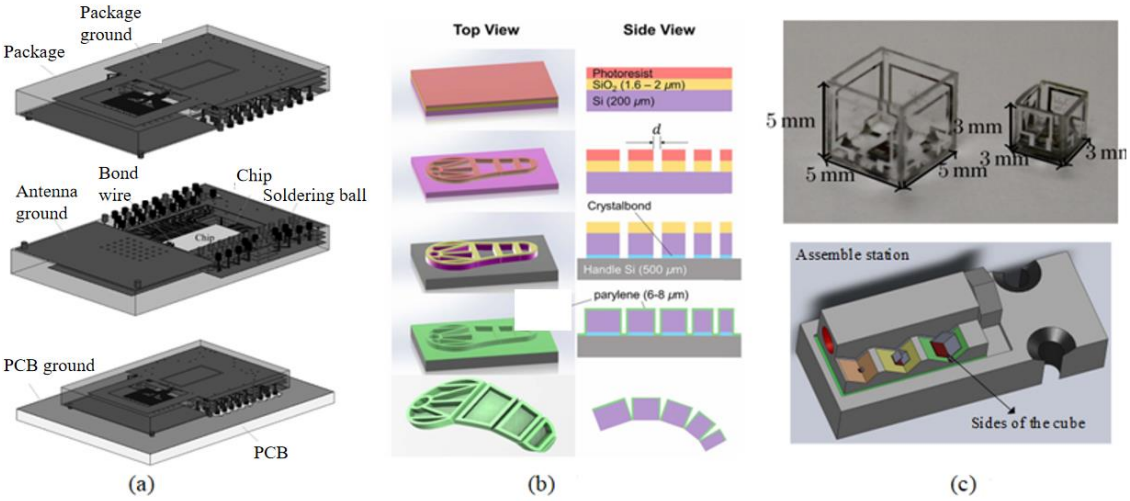

Figure 2.5 Geometry of antennas for antenna package. (a) [49], (b) [50], (c) [51].

Another method to develop small-size antennas for chips at high frequency is the 3D antenna and foldable planar antenna instead of regular planar antennas with large sizes. In paper [50], a Silicon wafer is etched into individual pieces, then assembled and folded using Crystalbond adhesive (see Figure 2.5(b)). [51] also adopts Pyrex glass as the 3D antenna substrate, but it assembles individual sides of the cube with silver epoxy (see Figure 2.5(c)). More details on 3D antenna technology and proposed 3D antenna design are shown in Section 2.3 and Chapter 3.

Since test equipment for the millimeter-wave band most commonly has a waveguide interface due to low loss and the capability for simple integration of different devices, the integration between the planar antenna feed and the metallic waveguide is necessary. The general coupled transition structure is based on electromagnetic coupling using an E-plane probe [52], patch antennas [53] (see Figure 2.6 (a) and (b)), and other radiating elements. More details on integration are shown in Section 2.4 and Chapter 4.

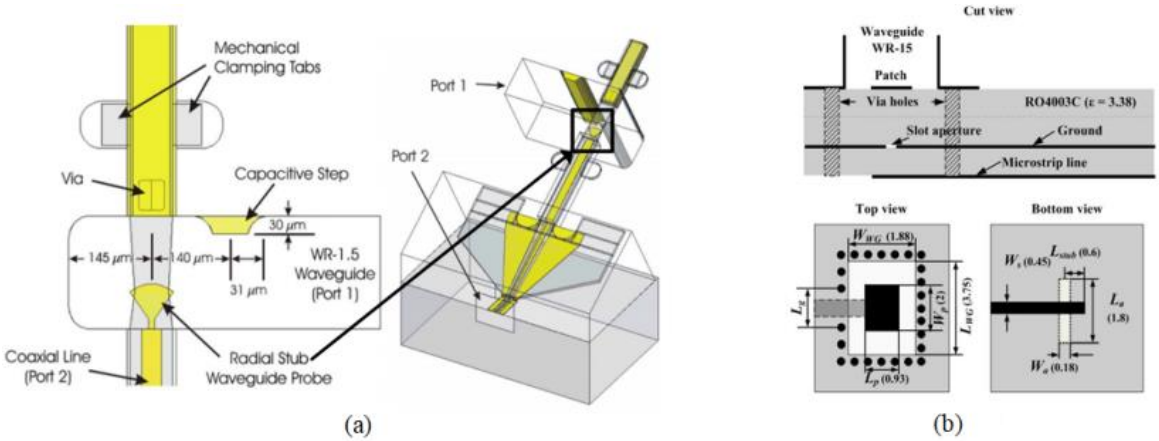

Figure 2.6 Geometry of integration with waveguide (a) [52], (b) [53].

2.2 Review of Micro-machined Terahertz Antennas

Terahertz frequency is generally defined at the 0.1-10 THz frequency band with a wavelength of 0.03-3 mm. Section 2.1 has discussed the review of micro-machined planar antennas from microwave to THz frequency. Considering substrate, fabrication processing, and applications in the THz frequency range, the most widely used micro-machined antennas are THz horn antennas, THz lens antennas, THz photoconductive antennas, and THz planar antennas. This section shows the review and development of these THz micro-machine antennas in Figure 2.7.

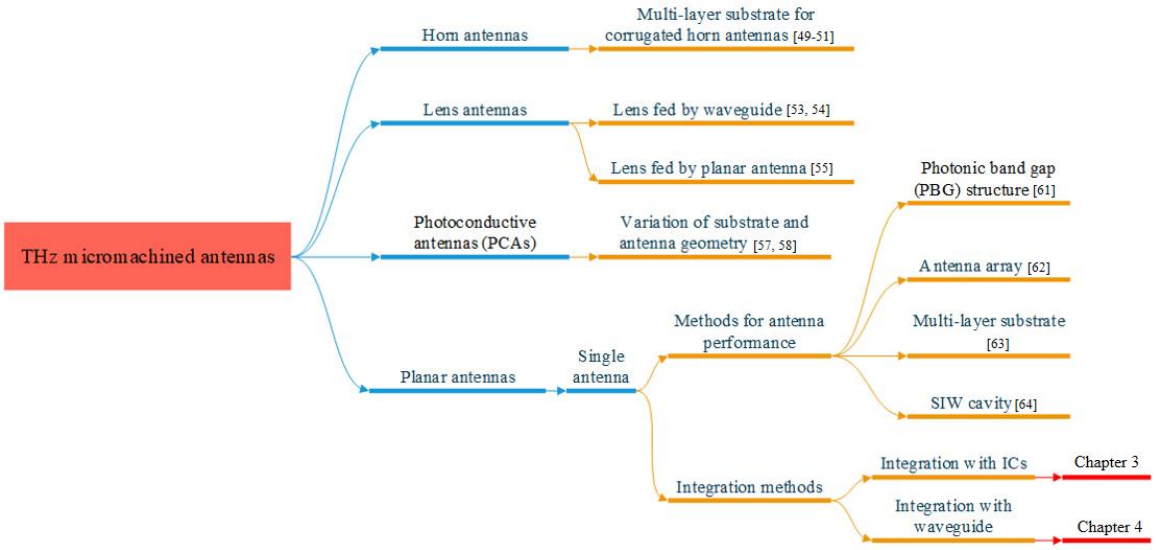

Figure 2.7 Micro-machined THz antenna categories.

In a high-speed THz communication system, the horn antenna can be used as a standalone antenna or as a feed source for a lens antenna or a transmitting antenna. Due to its simple structure, high gain, and wide frequency band, horn antennas have been widely used in high gain THz antennas. Although most horn antennas are fabricated by mechanically metal processing, some studies still exist on the new micro-machined technology of horn antennas. The antenna [54] operates at 300 GHz and uses a cavity in a multi-layer ceramic substrate and a surrounding via barrier to form a feed

hollow waveguide (see Figure 2.8 (a)). Similarly, [55], [56] also proposes a corrugated horn antenna using silicon-based micro-machined technology (see Figure 2.8 (b, c)).

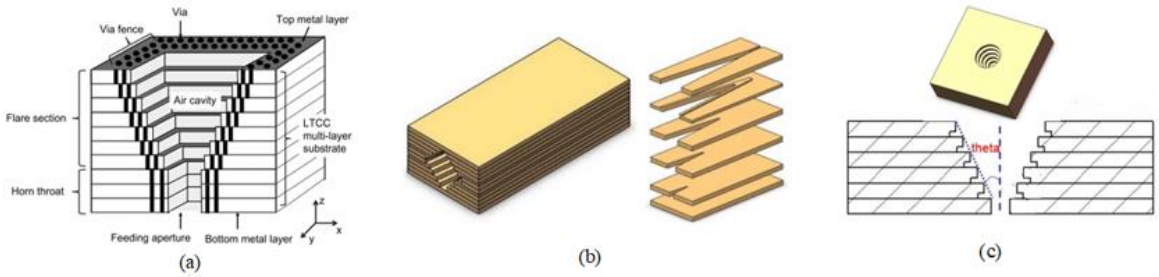

Figure 2.8 Geometry of micro-machined THz horn antennas. (a) [54], (b) [55], (c) [56].

The lens has the capabilities of focusing and imaging to improve the THz antennas' performance, such as reducing sidelobe levels and cross-polarization levels, achieving good directivity, and high gain. The dielectric lens is fabricated using a low-loss dielectric, typically thick in the middle of the lens and thin around the lens with focusing and imaging characteristics [57]. The dielectric lens can be fabricated in different shapes, such as ellipsoidal, hemispherical, over-hemispherical, and expanded hemispherical. The lens can be fed by waveguides and micro-machined planar antennas. [58], [59] are integrated arrays of extended hemispherical silicon lenses fed by leaky waveguides (see Figure 2.9 (a, b)). A logarithmic plane spiral feeds the lens working at 0.625 THz in [60] (see Figure 2.9 (c)). By appropriately changing the length and diameter of the lens, the far-field radiation beam can be controlled and optimized to achieve the target bandwidth.

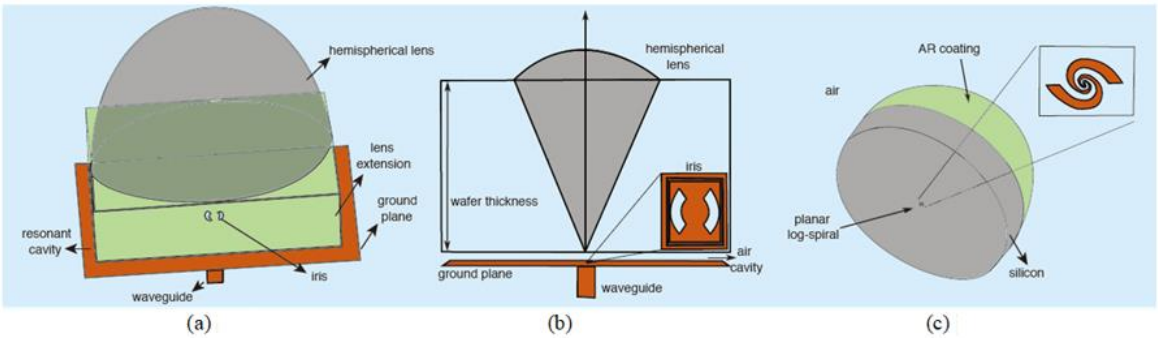

Figure 2.9 Geometry of micro-machined THz lens antennas. (a) [58], (b) [59], (c) [60].

The photoconductive antennas (PCAs) are used for the generation and detection of the THz wave. When a laser beam is irradiated on a photoconductive semiconductor (such as GaAs and InP) switch, an electron-hole pair is generated therein. If there is an external electric field in the photoconductive switch gap, usually generated by the DC voltage, a current is formed [61]. Many novel circuits for pulsed photoconductive sources are designed to show the coupling between the photoconductive gap and the antennas [62], [63]. Photoconductive antennas with different geometries, including H-dipole antennas, bow-tie antennas, and logarithmic spiral antennas, are shown in Figure 2.10.

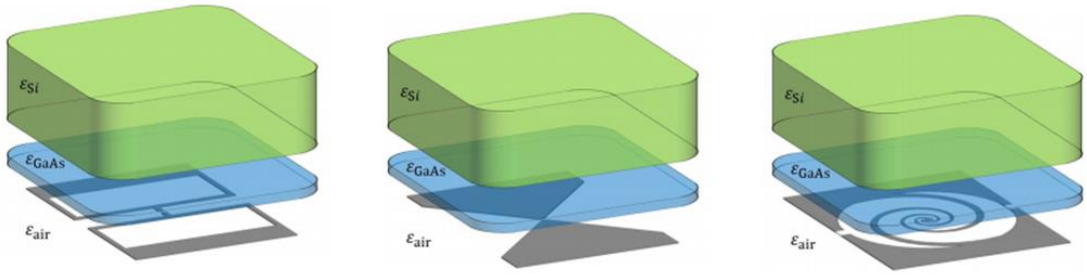

Figure 2.10 PCA geometries and structures [62], [63].

The planar antenna structure offers a greater potential when considering integration compatibility with planar devices. A planar antenna is designed with a thin dielectric substrate with a metal patch. The planar antenna is small, lightweight, simple to be manufactured, wearable, and suitable for massive production. There are many types of planar antennas developed.

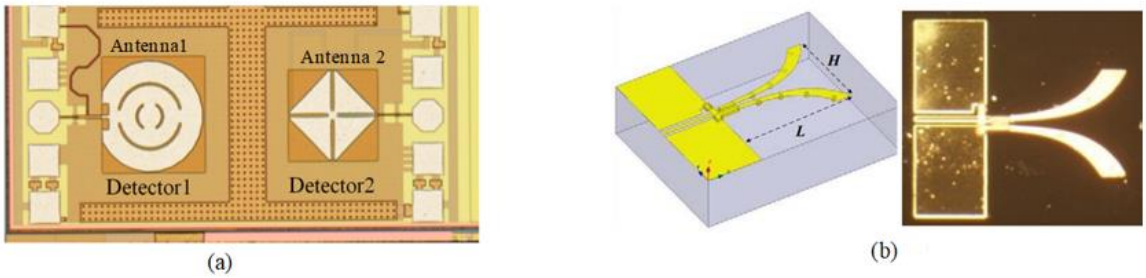

Figure 2.11 Geometries of single Si-based planar antennas. (a) [64], (b) [65].

Paper [64] proposes two Silicon-based microstrip patch antennas at 300 GHz with different slot shapes, circular double arc slot antenna (CDASA) and diamond diagonal slot antenna (DDSA), whose resonant frequency is around 300 GHz (see Figure 2.11 (a)). In Figure 2.11 (b), paper [65] shows a CPW-feed Silicon-based Vivaldi antenna working at 130 GHz.

The electromagnetic bandgap material can be used as the substrate of the antenna to reduce substrate loss. As shown in Figure 2.4 in Section 2.1, the holes create an "exclusion" of electromagnetic modes in the substrate and, therefore, dramatically increase the radiation efficiency of planar antennas [48].

In paper [67], patch microstrip antenna arrays of five elements are designed at 0.835, 0.635, and 0.1 THz using liquid crystalline polymer (LCP) substrate material (see Figure 2.12 (a)). It reveals that the number of array elements would be significantly reduced by using a multilayered substrate compared to the single substrate layer. The application of the multilayered substrate material in the terahertz antenna design has been discussed in [68] (see Figure 2.12(b)). Another solution to improve planar antenna performance is the substrate integrated waveguide (SIW). An SIW cavity associated with a patch antenna can be used to prevent surface waves. In paper [72], a proposed SIW cavity-backed array, as shown in Figure 2.12(c), consists of a stack of two substrates: the top substrate for the patches and the bottom substrate for the SIW cavities.

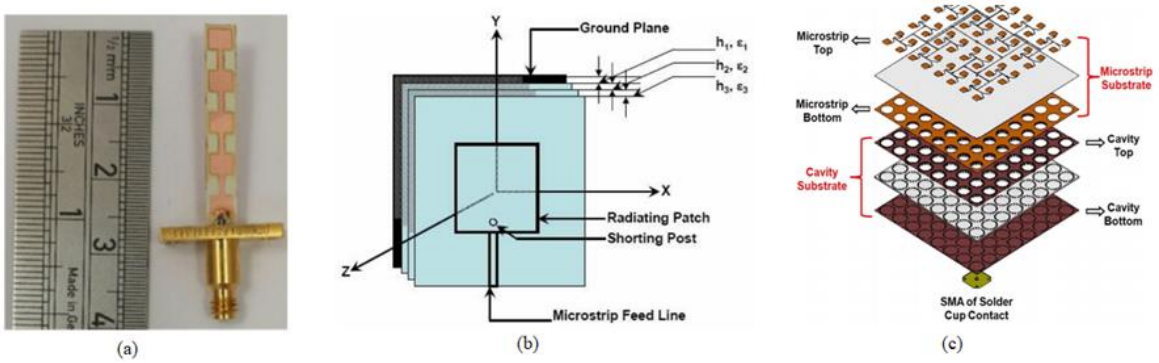

Figure 2.12 Geometries of microstrip antennas using PBG and DGS substrate. (a) [67], (b) [68], (c) [72].

In conclusion, this section gives a general review of THz horn antennas, THz lens antennas, THz photoconductive antennas, and THz planar antennas using micro-machined technology after the review and development of micro-machined planar antennas in millimeter-wave and terahertz frequency range is presented in Section 2.1. The future research directions of THz antennas mainly include these aspects: (1) Research on substrate materials: Traditional THz materials are silicon-based materials, but their indirect bandgap properties determine that silicon-based materials are difficult to be applied to nonlinear devices and active devices. Subsequently, the emergence of semiconductor materials such as silicon carbide, silicon nitride, and gallium arsenide with a direct bandgap, are also made up for this problem [4], (2) Research on antenna performance: One main obstacle to THz communication is the atmospheric attenuation. As the free space path loss is physically inevitable, increasing the gain of the transceiver antennas is used to compensate the free space path loss [69]. Therefore, in THz communications, the larger operating bandwidth and atmospheric path loss require the antennas to have broadband, high gain, and high efficiency performance, (3) Research on integration method: the packaging technology and integration method (such as CMOS, SiGe, mHEMT and etc) are necessary for THz on-chip antennas. For example, paper [70] presented an eight-element 0.37-0.41-THz phased-array transmitter by using 45-nm CMOS silicon on insulator technology. Besides, paper [71] proposed a 0.525-0.556-THz radiating source with a dielectric lens antennas mounted on top of the chip in 28-nm CMOS technology.

2.3 Review of 3D Antennas and Foldable Antennas

The first challenge of antenna for ICs is that the design method is shifting from conventional discrete designs to new integration methods with chips because of the requirements of smaller chip sizes at GHz frequency or above. 3D antenna is also a good solution for antennas for ICs when considering the miniaturizing size.

Another advantage of the 3D antenna is its compact size. Most of the antennas currently integrated with ICs are planar [73], [74], [75] because of their low cost and easy fabrication. However, these antennas have large cross-sectional areas and occupy most of the overall IC volume. Therefore, 3D antenna design is preferred for minimization technology because the antenna meanders on the 3D surface and the 3D cubic shape allows IC packaging inside the cube's hollow interior.

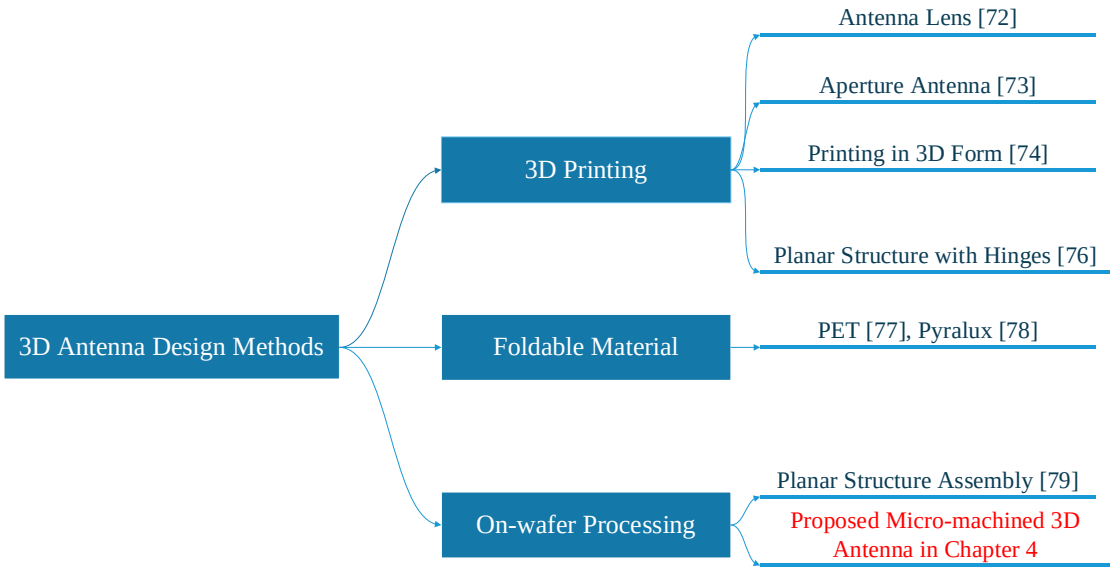

Figure 2.13 3D antenna categories.

Besides, sensor nodes and communication ICs employ either monopole/dipole antennas or planar patch antennas [76], [77], [78], and thus the directivity is limited to one dimension. Employing novel fully 3D structures, such as a cube, allows for the easy placement of planar antennas on multiple faces, enabling transceiving signals in multiple directions.

This section shows the review of 3D antenna design methods (See Figure 2.13). First, 3D printing is widely used in the 3D antenna fabrication method. 3D printing is the technology of building physical objects up layer by layer, based on a detailed digital blueprint [79]. It has been widely used in antenna lens and aperture antenna implementation. Paper [80] describes a 28-35 GHz antenna with an alumina lens. It adopts Polymer stereolithography (SLA) to produce the 3D-printed lens (see Figure 2.14(a)). In [81], two different metals and related 3D printing technologies are studied for aperture antennas. The first one is stainless steel by binder jetting and sintering. The second one is the Cu-Sn by selective laser melting (SLM). These two designs have no capability of housing the IC chips within the structure (see Figure 2.14(b)).

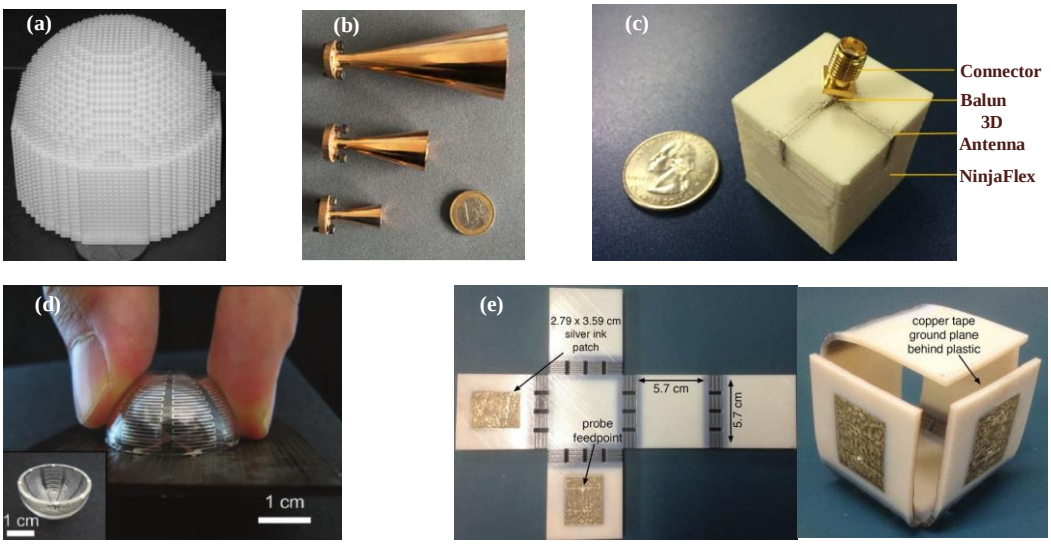

Figure 2.14 Geometry of 3D-printed antennas. (a) [80], (b) [81], (c) [82], (d) [83], (e) [84].

Paper [82] shows a 3D-printed antenna at 2.45 GHz for sensors, the substrate is printed by NinjaFlex filament, and the dipole arms are made by electrically conductive adhesive (ECA), of which the main composition is Silver (see Figure 2.14(c)). A 1.7 GHz electrically small antenna is shown in [83]. Silver is printed on the hemispherical surface by inkjet printing (see Figure 2.14(d)).

Like 3D-printed with foldable hinges, many flexible materials have been used as 3D antenna substrates. [85] shows a 2.45 GHz quasi-Yagi antenna of which the substrate is 0.175 mm thickness PET, and the metal is silver conductive ink (see Figure 2.15 (a)). And for the dipole antenna working at 17.2 GHz in [86], PCBs connected by Pyralux is folded into a cube (see Figure 2.15 (b)).

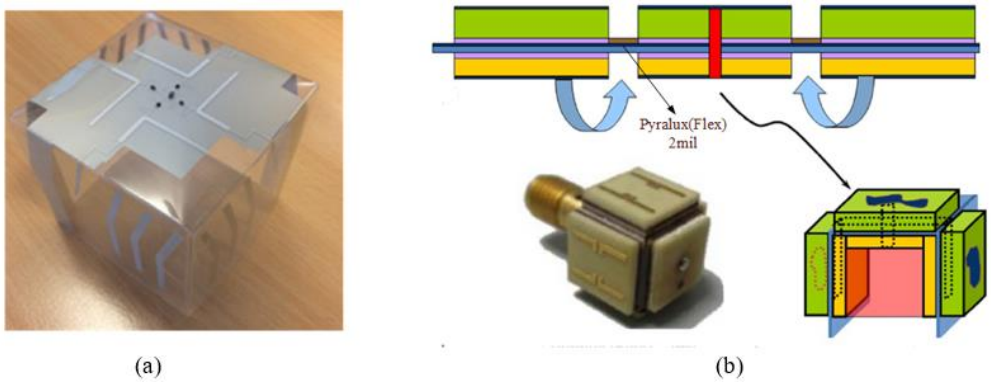

Figure 2.15 Geometry of foldable material antennas. (a) [85], (b) [86].

Paper [87] proposes a 3D antenna design using standard fabrication methods. Five pieces of planar Pyrex glass are antenna substrate, and Aluminum is deposited on the glass's surface. Then pieces of glass are assembled into a cube on an assembly stage with silver epoxy (see Figure 2.16).

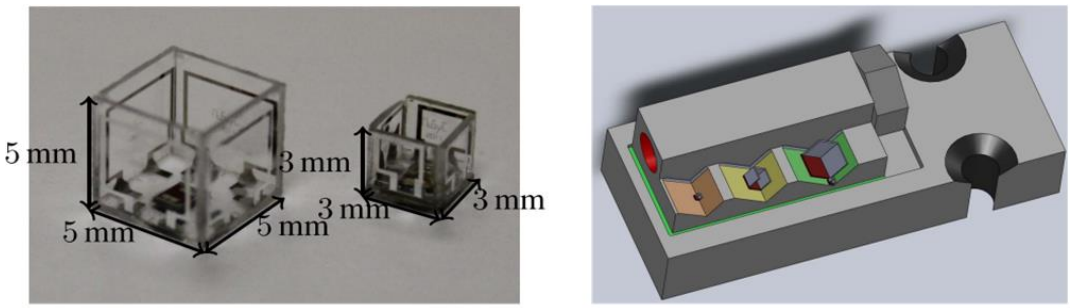

Figure 2.16 Geometry of glass-based 3D antenna and its assembly stage [87].

The advantages of the 3D printing technology include timesaving and the capability to fabricate the complex structure with multiple materials, which are out of the standard fabrication methods' capability. However, there are some disadvantages of this technology compared to standard micro-machined fabrication methods. As shown in Table 2.1 [88], [89], [90], it can be seen that the minimum feature size, printing resolution, and surface roughness of 3D printing are larger than these values in Silicon-based wafer processing, which are challenges for antennas at GHz technology or above. According to the records in UVa Microfabrication Laboratories (UVML), AZ4620 photoresist is used for lithography processes by MJB4 mask aligner, which typically gives around 6.2μm thickness at 4 krpm spin speed and has a resolution limit of about 6μm for minimum achievable line width. AZ4330 photoresist gives about 3.3μm thick photoresist at 4krpm spin speed and can work with finer features. A minimum line width of 4μm and a gap of 2μm has been achieved under good contact conditions.

The antenna substrate by 3D printing is limited to a low permittivity polymer, which means that the planar antenna dimension is larger than the Silicon-based antenna. Thus, Chapter 3 develops a 3D cube antenna using Silicon-based micro-machined fabrication methods, which has the capability of housing ICs within the structure. More analysis and comparisons between the proposed antenna and other 3D antennas are shown in the next chapter.

Table 2.1 3D Printing and Micro-machined Processing Technologies Comparison.

Technology	Printed material	Minimum feature size (um)	Minimum layer thickness (um)	Resolution (um)	Minimum surface roughness (um)
Stereolithography (SLA)	Liquid photopolymer resin	100	16	+/-150	0.15
Fused deposition modeling (FDM)	Thermoplastic filament	178	178	+/-178	13
Selective laser sintering (SLS)	Thermoplastic, ceramic powder	150	100	+/-250	1.8
Selective laser melting (SLM)	Metal powder	40-200	30	+/-200	2
Material jetting (MJ)	Photopolymer, wax	100	13	+/-25	1
Binder jetting (BJ)	Plastic, metal, and ceramic	100	90	+/-130	4
MJB4 mask aligner*	AZ4620 on Si AZ4330 on Si	6 4	6.2 3.3	<1 <1	NA
MJB4 mask aligner*	AZ4330 on Si	4	3.3	NA	NA
E beam lithography*	Ti, Au	NA	Ti: 1Å/s Au: 1.5Å/s	NA	<10Å
Sputter 3*	Ti, Au	NA	Ti: 0.5Å/s Au: 1Å/s	NA	<10Å
Electrical Au plating*	Au	NA	Depends on voltage control	NA	<100nm

The data of technology mark with * is recorded by researchers in IFAB in University of Virginia.

2.4 Review of THz Antennas Integration Methods with Waveguides

Many millimeter-wave and THz systems and modules are based on ICs and planar devices. However, devices such as aperture antennas and high-quality-factor (HQ) filters based on waveguide technology are also required. Furthermore, THz test equipment most commonly has a waveguide interface due to low loss and simple integration of different devices. Thus, the integration between the planar antenna feed and the metallic waveguide is necessary.

Paper [91] demonstrates a dielectric probe operating in the sub-terahertz range with an example band of 190-220 GHz. High-resistivity silicon technology is deployed for this non-TEM mode probe development as it presents a viable low-loss material. A T-shape alignment dowel is used to integrate the silicon probe with the waveguide block. The probe can be used to measure and characterize the low permittivity-based dielectric waveguide transmission line (see Figure 2.17). The cross section of the dielectric rod waveguide is 915 μm by 640 μm.

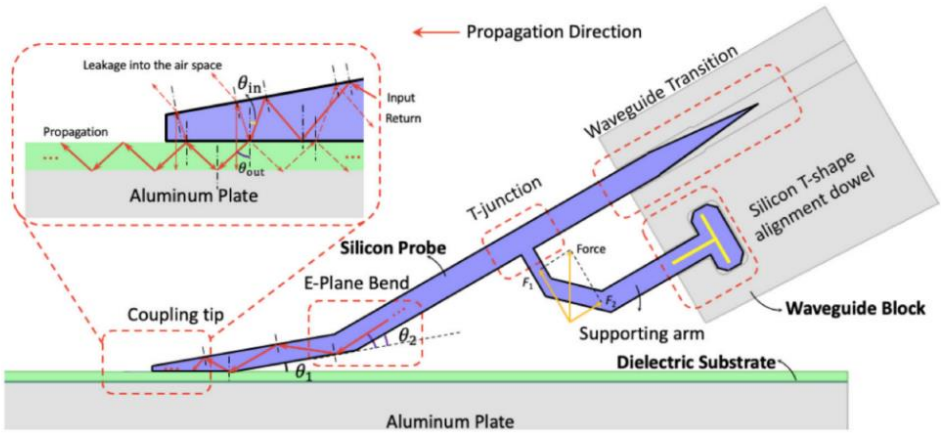

Figure 2.17 Silicon-based dielectric probe structure and its working principle at 200 GHz [91].

The general coupled transition structure is based on electromagnetic coupling using an E-plane probe for different applications. Paper [92] proposed a micro-machined probe for submillimeter-

wave on-wafer measurements using a fan-shaped E plane probe (see Figure 2.18 (a)). Patches are designed as E plane probes in paper [93], [94], [95] for the integration with monolithic microwave integrated circuits (MMIC) (see Figure 2.18 (b)), THz triplers (see Figure 2.18 (c)), and a WR 2.2 coupler (see Figure 2.18 (d)). These E plane probes are designed to be perpendicular to wave propagation direction in waveguides. Thus, the end of waveguides is λ/4 far from the E plane probe for wave propagation in one direction.

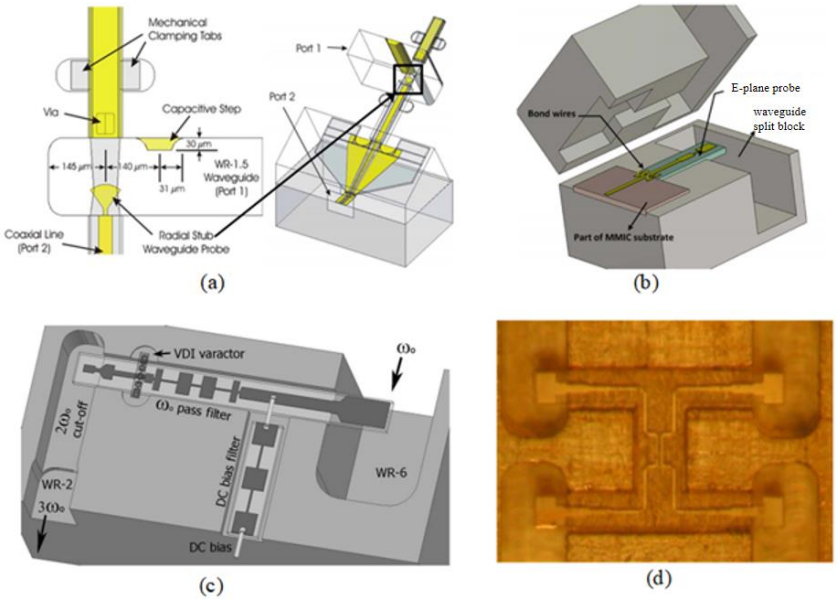

Figure 2.18 Geometries of E plane probes and applications. (a) [92], (b) [93], (c) [94], (d) [95].

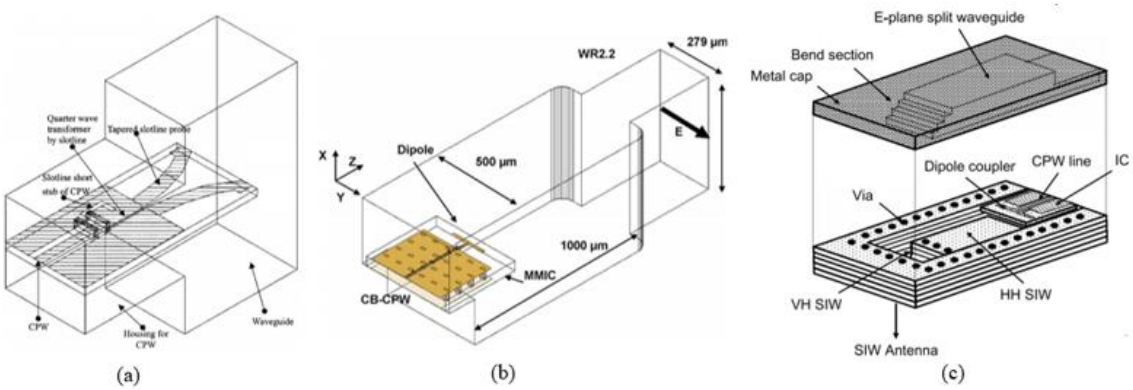

Figure 2.19 E plane probes with different radiating element geometries. (a) [96], (b) [97], (c) [98].

Other radiating elements are also used for E plane probes. Paper [96] in Figure 2.19 (a) proposes a CPW to waveguide transition consisting of a tapered slot line probe and a slot line to a CPW line matching section. In paper [97], a 340-380 GHz CPW-waveguide transition for MMIC packaging is demonstrated using a dipole probe (see Figure 2.19 (b)). Paper [98] presents a THz antenna-in-package solution that connects an IC to an SIW antenna by a dipole probe. An H-plane bend is investigated for the SIW antenna (see Figure 2.19 (c)).

The chapter follows the idea in the paper [84] and shows E-plane probes for the WR6.5 waveguide and WR2.2 waveguide in Chapter 4. The proposed E-plane probes are the transition between proposed THz antennas and probe housing to achieve antenna measurement and far-field applications.

2.5 Review of Millimeter-wave Frequency and THz Antennas Integration with ICs

In the last couple of decades, semiconductor devices and integrated circuits (ICs) have been greatly advanced and investigated for various millimeter-wave frequency and THz applications, such as imaging, security, and wireless communications. In the meantime, researchers have been exploring ways on mm-wave and THz antenna design as well as packaging those electronic devices and integrated circuits. The antenna is used to provide stable signal transceiving between a circuit and free space, and sometimes it is expected to provide a physical housing for devices and integrated circuits (ICs). However, as frequency increases, researchers face several challenges associated with signal loss, dimensions, and fabrication when considering the integration between antennas and ICs [99]. This section provides a brief review of recent progress in packaging and antenna integration for millimeter-wave frequency and THz ICs.

At millimeter-wave frequency and low THz range, the horizontal integration is "antenna on PCB," which implements antenna on the PCB [100], [101]. This method offers the option of using the best technology for each component. For example, digital circuits are best suited to complementary metal-oxide-semiconductor (CMOS) technology, power amplifiers may use III–V compound semiconductor technology, and antennas function efficiently on low-loss printed circuit boards (PCBs) such as FR-4, Duroid, etc. The horizontal integration results in the well-known multichip modules (MCMs), as shown in Figure 2.20(a) [102]. This approach consumes considerable chip area, which is a major disadvantage with the ever-reducing size of cellular and other wireless devices.

With increasing frequency, the approach of vertical integration with smaller dimensions using

the antenna-in-package (AiP) provides a useful alternative to “antenna on PCB,” e.g., a 64-element antenna array for D band communication [103], a phased array mixing silicon and III-V chiplets [104], and an 89 GHz superstrate antenna stacking an antenna layer directly on the back side of a silicon-based IC [105]. Even in this case, the antennas, whose dimensions are on the order of wavelengths, are usually the largest components of the system [106].

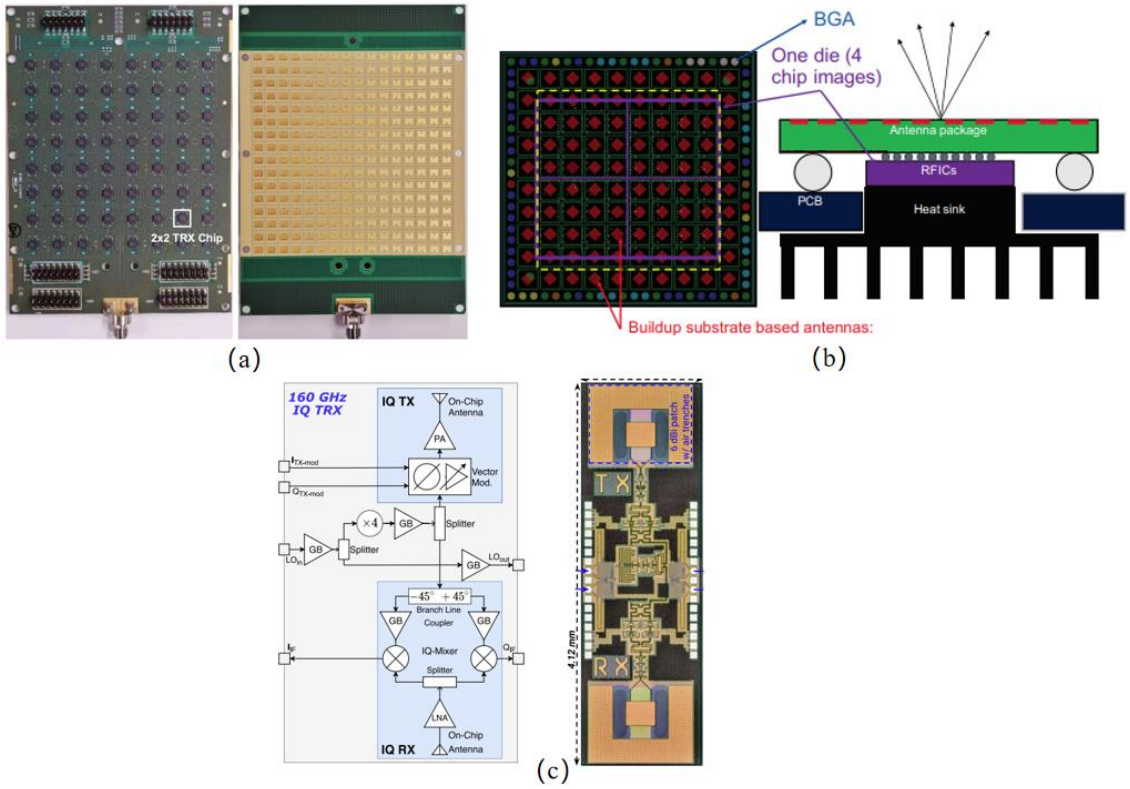

Figure 2.20 Implementation diagram of (a) antenna on PCB [102], (b) antenna in package (AiP) [103], (c) system on chip (SoC) [109].

Furthermore, to overcome increasing cost and losses of flip-chip bonding [107], the system-on-chip (SoC) approach has triggered significant interest, as it allows on-chip integration of digital baseband and complete RF front ends. At the same time, the application push toward the higher frequencies, particularly millimeter-waves above 100 GHz (120 GHz ISM band [108], W/D band (75-170 GHz) [109], and J band (220-325 GHz) [110]), has reduced antenna sizes to only a few millimeters, making it both possible and practical for on-chip implementation.

SoC offers several advantages compared to the antenna-in-package integration. (1) SoC doesn't need the impedance matching network between RF front-end and antenna since both can be co-designed in such a way that their impedances are conjugately matched, which results in a lower cost and a reduction in system volume. (2) SoC avoids the need of lossy and unpredictable interconnects between antenna/RF front-end section, such as flip-chip bonding and wire bonding. These interconnects cause the system loss, especially at mm-Wave and THz frequency. (3) SoC helps in achieving a higher system bandwidth as they introduce smaller parasitic losses because of the absence of the metal interconnects. (4) SoC provides a high power-efficiency of the system because of the reduced dielectric losses and minimum reflection of the signal [112]. (5) SoC makes the design cycle of the wireless system shorter [113] since they enable a co-design approach of the antenna and RF front end.

The SoC implementation in mm-Wave and THz frequency bands has its own advantage compared to other integration methods. First, the antenna size is compact. Second, silicon-based CMOS technologies, the preferred choice for SoC design, have proved their potential for mm-Wave and THz applications with the innovative developments [114], [115], [116]. Some most prominent applications include: mm-Wave transceivers for MIMO-based 5G wireless systems, IoT wireless devices and systems, wireless sensor network nodes, biomedical implants, RF energy harvesting, wireless power transfer, wearable devices, and so on.

There are still challenges to silicon-based SoC at mm-wave and THz frequency because of the values of the permittivity and resistivity of the silicon substrates. Typical commercial CMOS technology substrate has high permittivity (ε_r=11.8) and low resistivity (10 Ω -cm) [117]. Due to small distance in CMOS process (≈16 μm [118]) between the top metal and Si substrate and low resistivity of Si substrate, antenna radiations and EM waves find a low resistive path through the

substrate and a major percentage of these EM waves is dissipated in it. It is beneficial for wireless ICs because a high-performance transceiver needs a substrate that prevents the signal from being radiated outside the substrate. It also prevents the latch up problem in ICs [107].

However, the high permittivity and low resistivity are not suitable for a high-performance antenna in the SoC design. The result is lower EM radiation into the air, causing a drastic degradation in the antenna's gain and efficiency.

Thus, an opposite set of performance criteria for the antenna and other components of transceiver systems in terms of silicon substrate properties is a major challenge. Moreover, the high permittivity of silicon substrates enables surface waves and high back radiation which severally degrade the antenna's radiation. To solve these problems, the antenna design is realized using a silicon-on-insulator (SOI) substrate with a 15-μm thick device layer as discussed in Chapter 4.

Chapter 3

3. Development of Micro-machined 3D Foldable Antennas

The recent advances in very-large-scale integration (VLSI), micro-electromechanical systems (MEMS), and wireless communications have driven many researchers towards innovative wireless sensor networks (WSNs) and communication ICs [119], [120]. The WSNs and ICs are composed of sensors to feel the environment's physical characteristics and transceivers to communicate with other ICs. These ICs have numerous applications, such as wireless communication and environmental monitoring. The first challenge of antennas for ICs is that the design method is shifting from conventional discrete designs to new integration methods with chips because of the requirements of smaller chip sizes at GHz frequency or above. Except for antenna-in-package (AiP) solutions discussed in Chapter 1, the 3D antenna is also a good solution for ICs when considering miniaturizing size.

Most of the antennas currently used for wireless sensor node applications are planar [121], [122], [123] because of their low cost and easy fabrication. However, these antennas have large cross-sectional areas and occupy most of the overall IC volume. Therefore, the 3D antenna design is preferred because the 3D cubic shape allows IC packaging inside the cube's hollow interior. The 3D

structure is also beneficial in opening the internal volume for other uses, such as storage for batteries.

Besides, sensor nodes and communication ICs employ either monopole/dipole antennas or planar patch antennas [124], [125], [126], and thus the directivity is limited to one dimension. Employing novel fully 3D structures, such as a cube, allows for the easy placement of planar antennas on multiple faces, enabling transceiving signals in multiple directions.

The motivation for this section is to develop small-size antennas for CMOS communication IC at high frequency. In Section 3.3, previous work on minimizing the dimension of the antenna is discussed. In this chapter, a Silicon-based micromachined 3D cube antenna is presented for ICs, since 3D antennas have a smaller size and have more available interior volume as storage for CMOS ICs and other elements.

3.1 Concept of 3D Antenna for Miniaturization and Internet of Things (IoT) ICs Packaging

The Internet of Things (IoT) is a distributed system for creating value out of data. It enables heterogeneous physical objects to share information and coordinate decisions. The impact of IoT in the commercial sector results in significant improvements in efficiency, productivity, profitability, decision-making, and effectiveness [127]. IoT transforms how products and services are developed and distributed and how infrastructures are managed and maintained. It is also redefining the interaction between people and machines. From energy monitoring in a factory [128] to tracking supply chains [129], IoT optimizes the equipment's performance and enhances workers' safety. It has allowed for more effective monitoring and coordination of manufacturing, supply chains, transportation systems, healthcare, infrastructure, security, operations, and industrial automation, among other sectors and processes.

The IoT applications and architecture are shown in Figure 3.1. There are three components that are required for the proper functioning of IoT [130]. (1) Hardware and technologies: It incorporate sensors, actuators, and other embedded devices and technologies. (2) Middleware: It comprises repository and data analytic tools. (3) Display: It comprises some presentation tools required for user interaction. At the hardware level, there are many integrated platforms for the developing and managing IoT products. For the examples in Figure 3.2, Samsung Artik [131] modules are based on ARM processors with attributes of their reduced complexity and low power consumption, making them suitable for IoT applications. Raspberry Pi [132] is another popular platform with a variety of uses. It is a small, powerful, education-oriented computer board designed for scientists, students, academicians, and enthusiasts to develop IoT projects. Antenna-in-package (AiP) technology, in which an antenna with a transceiver chip in a standard surface-mounted device, represents an

important antenna and packaging technology achievement for IoT hardware devices. This chapter shows a 3D antenna design for ICs used in IoT systems.

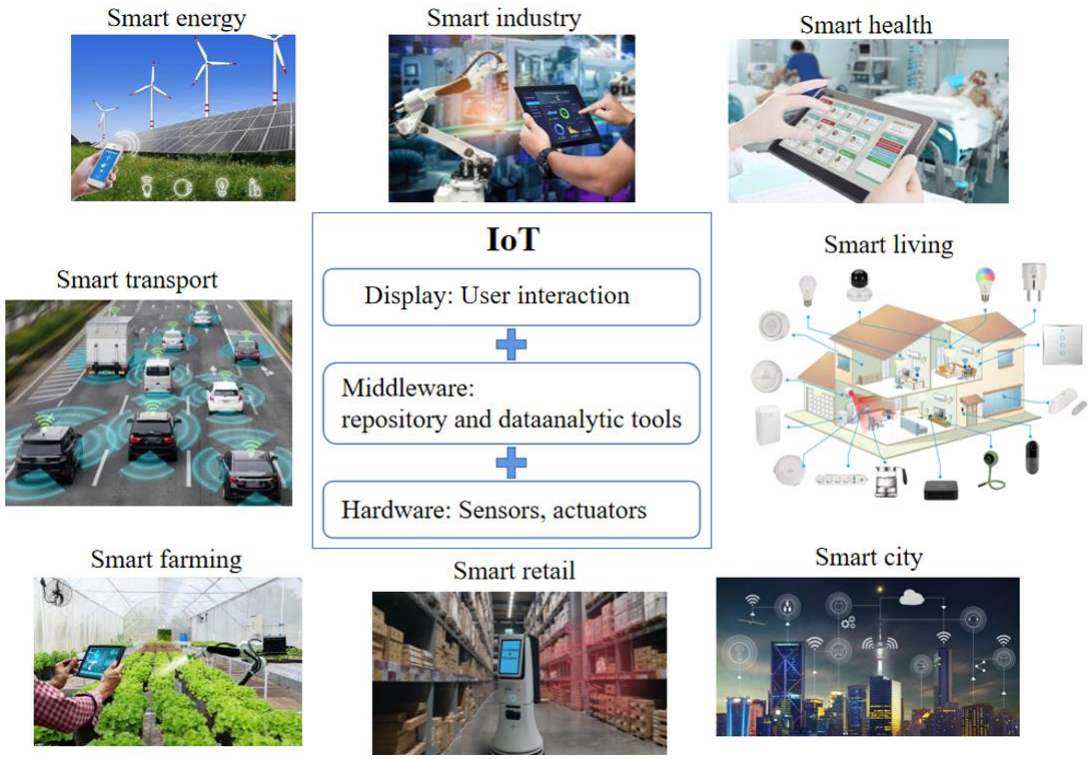

Figure 3.1 IoT Applications and Architecture.

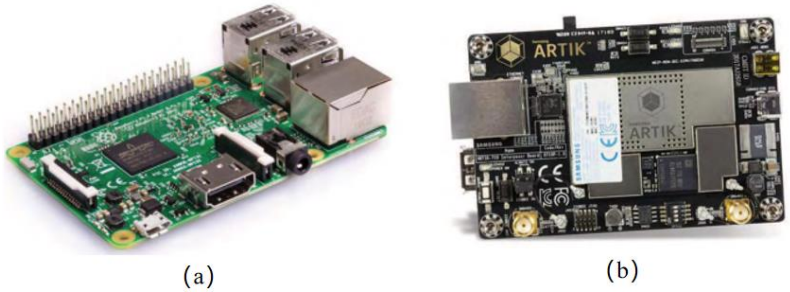

Figure 3.2 Examples of IoT platforms. (a) Raspberry Pi [132], (b) Samsung Artik [131].

The antenna structure concept is shown in Figure 3.3(a), which produces an omnidirectional pattern at 10 GHz. It has dimensions of 3 mm edge length, of which the cubic shape allows for CMOS IC packaging inside the cube's hollow interior. The prototype fabrication is performed on five planes

on a 50 μm thickness silicon substrate with two orthogonal meandered-line antenna arms on the same side of the substrate and then folded into the cubic structure and strengthened by straps [133].

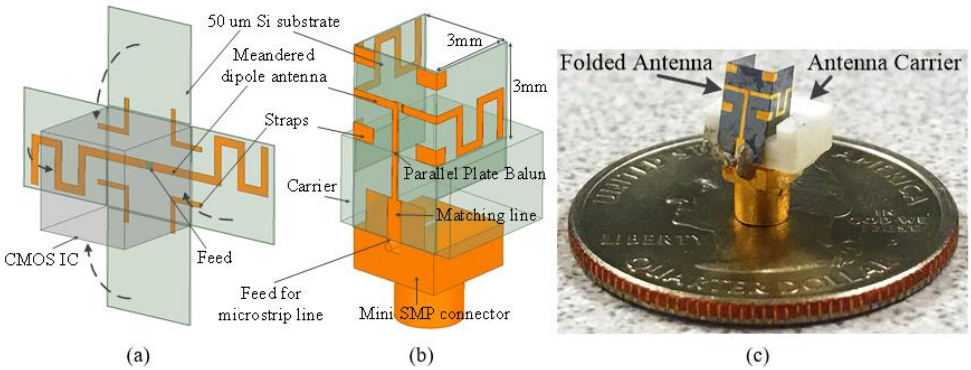

Figure 3.3 Geometry of Meandered-line Cube Antenna. (a) Concept Antenna for IC Packaging. (b) Antenna for Coaxial Connector. (c) The Proposed Antenna with a Quarter Coin.

The proposed antenna in Figure 3.3(b) is interfaced with a coaxial connector for antenna performance measurement. A λ/4 parallel plate balun is integrated on the substrate for transition and impedance matching. The Si substrate can be folded into the cubic structure and strengthened by 5 μm thick antenna arms and additional gold straps, and the whole assembly is inserted into a holder made by 3D printing. The folded antenna with a plastic holder is connected to an SMP connector by silver epoxy. (See Figure 3.3(c)).

3.2 Micro-machined 3D Meandered-line Foldable Antenna Design

The basic idea of antenna miniaturization techniques is to use the available space (or volume) efficiently to fit a larger radiating structure by incorporating additional dimensions in classical antennas [134]. Compared to the straight-wire dipole, meandered line technology allows for designing antennas with features such as small size and 3D packaging. Two symmetric arms of the antenna are meandered to reduce the dimension of the antenna.

An antenna is considered electrically small as a function of its overall size or occupied volume relative to the wavelength. A small antenna is one where $ka \leq 0.5$, where $k=2\pi/\lambda$ is the free space wavenumber, and a is the radius of an imaginary sphere circumscribing the antenna's maximum dimensions. Consider a straight-wire electric dipole at 10 GHz in free space with an overall length equal to 1.524 cm, its ka=1.59. In the proposed design, the antenna arms meander on a cube of 3 mm in length, and its ka=0.314. Thus, compared to the straight-wire dipole with large ka, meander line technology allows for designing antennas with small-size features.

Some papers discuss meandered-line antenna performance with different configurations and orders [135] (see Figure 3.4(a)). Paper [136] shows that all the antenna geometries exhibit similar behavior. With increasing total wire length, the resonant frequency, resonant radiation resistance, and resonant bandwidth decrease. Moreover, the lower gain is due to the high percentage of canceled radiated fields generated by horizontal segments of the meandered-line antenna [137]. In this design, a two-order orthogonal rectangular meandered dipole antenna is chosen for enhanced bandwidth and efficiency (see Figure 3.4(b)). Each side of the cube is 50 μm thickness Silicon, the feed of this dipole antenna is at the center of the top side, and dipole arms are extended from the top side and meandered

on the left and right side. HFSS is used to determine the width and length of meandered lines, the slot between two antennas, and the number of meandered sections.

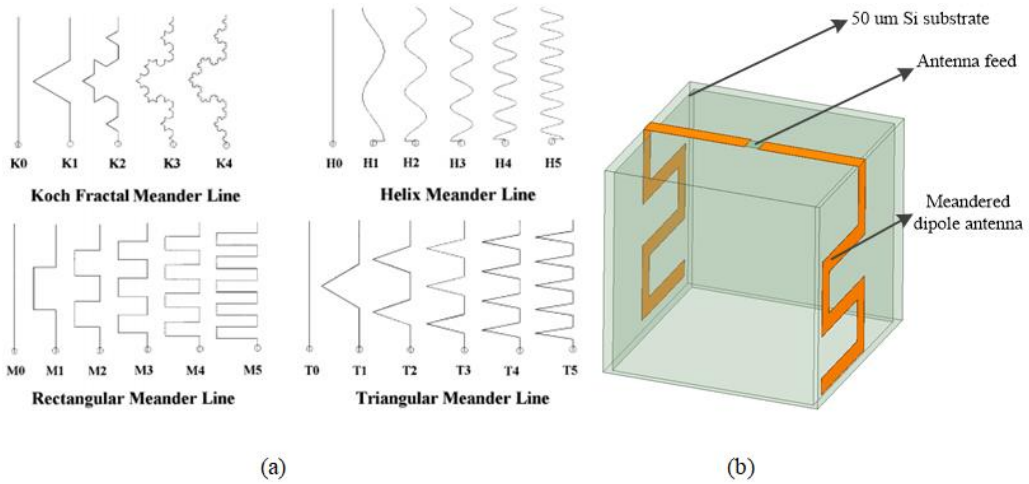

Figure 3.4 Geometry of Meandered Lines.
(a) Various Meandered-line Antennas' configuration. [135] (b) Proposed Meandered-line Dipole Antenna.

For antenna matching network design, a balun is used to transition the balanced and unbalanced signals. Antennas give a balanced feed but the connection to the receiver, such as a coaxial cable, is unbalanced. In this design, a λ/4 parallel plate balun is used to match antenna impedance (from 10-7.6j Ω to 50 Ω) and cancel the unbalanced current from the unbalanced coaxial feed line [138].

The geometry of the cube antenna with balun is shown in Figure 3.5(a). The left-hand side dipole arm is connected to the parallel plate balun, and the right-hand antenna arm goes through an etched via to generate the other parallel plate and is connected to the ground of the matching line. Besides, the 5 μm thickness antenna arms and straps are used to strengthen the cube's sides, and the plastic carrier is made by 3D printing. The dimensions of the dipole antenna and the parallel plate transformer are optimized by HFSS to match the input impedance to 50 Ω. The width and length of the feeding network are optimized for the best match to 50 Ω. Figure 3.5(b) shows the detailed dimensions: W1=0.22 mm, W2=0.63 mm, W3=0.2 mm, W4=0.5 mm, W5=2.2 mm, L1=1.55 mm,

L4=1.3 mm L2=2.535 mm, L3=4.35 mm.

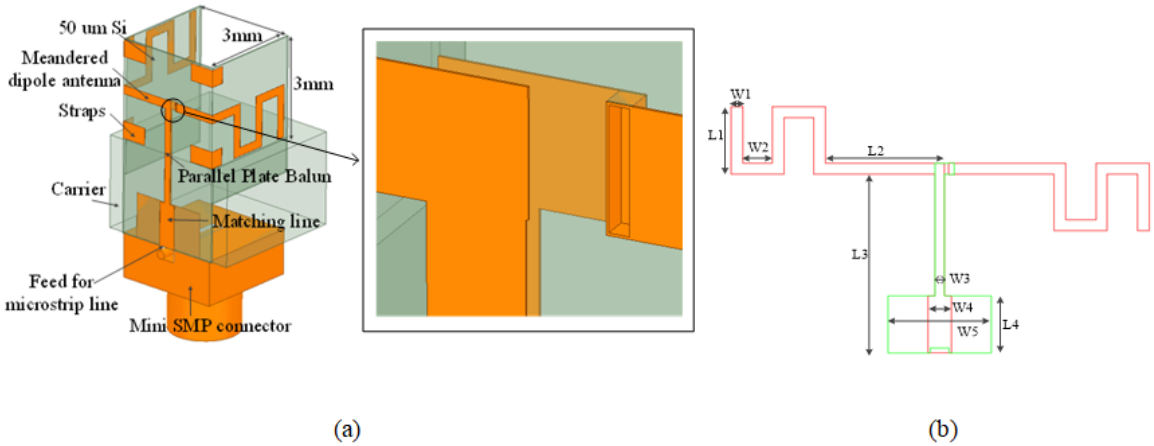

Figure 3.5 Geometry of Proposed Antenna. (a) Geometry of Proposed Antenna with 3D Printed Carrier and Mini SMP Connector. (b) Dimensions of Cube Antenna (red line: frontside gold, green line: backside gold).

3.3 Micro-machined 3D Antenna Fabrication Design

Unlike other papers that use 3D printing or liquid crystal polymer (LCP) for antenna substrate, this work presents a new fabrication approach based on Silicon processing in Figure 3.6.

First, a 50 μm thickness silicon wafer is cleaned, and there is a 4 μm thickness layer sputtered by Diode Sputter. The aluminum layer is used as additional strength and etch stop on the backside of the wafer. The wafer with Aluminum is placed on a larger carrier with black wax, and the via holes as well as alignment markers are etched in the first step (see Figure 3.6 (1, 2)). It is realized at the IFAB using the Oxford Instrument Plasmalab System 100 ICP-RIE etch tool. This process uses two gas species, SF_6 and C_4F_8, for the Bosch Si etch [139]. The SF_6 is the primary gas etchant that becomes ionized in the chamber to provide fluorine ions to actively etch the Si. The C_4F_8, though also releasing fluorine, is the passivation gas species that helps create a polymer chain deposited on the Si surface to protect it from chemical reactive etching. With sufficient RF power, the directionality of the accelerated fluorine ions supplied by the ICP-RIE tool means that the fluorine ions can physically remove the polymer chain at the horizontal planes of the Si surface. If the polymer growth is sufficiently robust and the energy of laterally scattered ions is sufficiently low, the polymer will remain on the vertical sidewalls [140]. As a result, the etch process occurs at the horizontal planes but is greatly reduced at the sidewalls. AZ330 photoresist is used for Bosch etch lithography processes, which typically gives around 3μm thickness at 4 krpm spin speed. The resulting process outcome can be very vertical sidewalls for patterns etched in Si, as shown in Figure 3.7 (a).

Next, a Ti-Au seedlayer is fabricated on the via hole sidewall and the front side of the wafer by Sputter 3 since plated gold does not adhere well to bare Si substrate, and it is also not possible to plate gold film directly on top of a Si wafer, The via holes are designed to make electrical connection

between the front-side and backside gold antenna radiator, thus gold plating inside the via holes is crucial for the proper functioning of the antenna. Furthermore, different from other evaporators, Sputter3 can evaporate the metallic seed layer on the side wall for plating gold (see Figure 3.6 (3)).

After the Si wafer is coated with a Ti/Au/Ti seed layer, it is then patterned with the photoresist. Different from the positive photoresist used in Bosch etch lithography, negative PR nLof2070 is used for the gold plating lithography (Figure 3.6 (4)). The first reason is that positive PR on the bottom of the via hole is insufficiently UV exposed because of the 50 μm height difference between the via bottom and the wafer surface. Thus, it's hard for positive PR to be developed to become photoresist openings. Conversely, the photoresist openings are the "dark" part of the lithography mask for negative PR. The second reason is that nLof2070 is one of the few photoresists whose thickness can be larger than 5 μm since the front-side and backside gold thickness is around 5μm.

One challenge of gold plating is that the plating rate is slow when Au is plated on the Ti layer. The top Ti at the plating area needs to be removed. A dry etch process in a Semigroup 1000-TP RIE etch tool is employed to achieve anisotropic Ti etch using etchant gas species SF_6. The revealed Au layer is open for electrical plating after that (see Figure 3.6 (5)).

When the gold plating is completed, the photoresist can be removed. Acetone is a good photoresist remover for positive PR, but 1:1 NMP and P-Grog are more efficient for positive PR removal. The Ti/Au/Ti seed layers beneath the plating photoresist should also be removed by sequentially performing a Ti dry etch, gold wet etch, and Ti dry etch. BOE is also a good wet etch solution for Ti. After seedlayer removal, Aluminum is etched by Al etchant type D at the rate of 0.1 μm/min (see Figure 3.6 (6)).

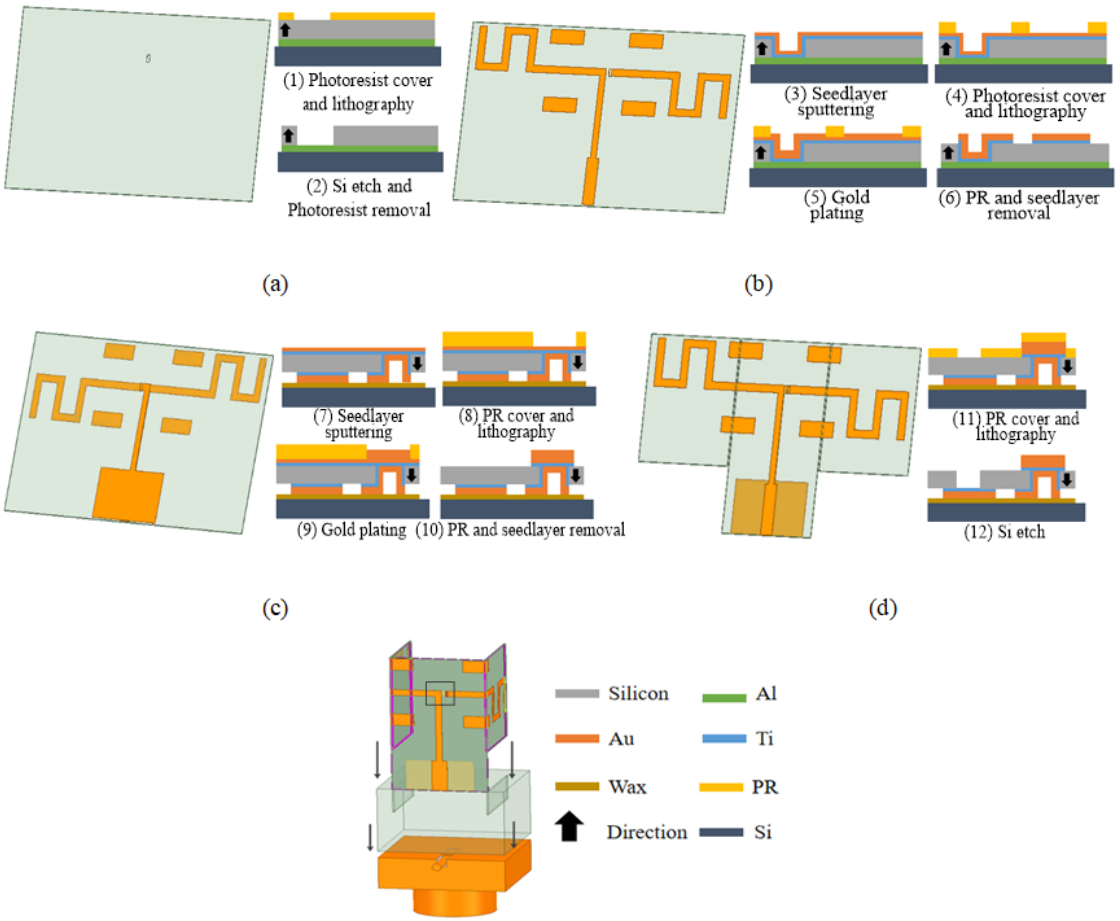

Figure 3.6 Cube Antenna Fabrication Process. (a) Si Etch for Via Hole. (b) Au Plating on the Front Side. (c) Au Plating on the Back Side. (d) Si Etch for Gap.

Backside fabrication is similar to the frontside process. 5 μm thickness gold is plated on the backside after Ti-Au seedlayer sputtering and lithography (Figure 3.6 (7-10)). Then the extents lithography is performed to define the cube contours using the photoresist as the etch mask, and two 60 μm width gaps are fabricated by Si etch (Figure 3.6(11-12)). Since the substrate thickness is 50 μm, the 60 μm width is a safe number for folding in the next step.

After fabrication, the left and the right-side silicon substrate are folded to ninety degrees and inserted into a plastic carrier made by 3D printing (Figure 3.6 (e)). The whole antenna system is then

placed on a mini SMP connector, which can be connected to a coaxial cable. The antenna is connected to the SMP signal pin using silver expoy.

Fabrication pictures under SEM are shown in Figure 3.7. An etched align marker is shown in Figure 3.7(a). Plated Au on the via hole sidewall and frontside silicon is shown in Figure 3.7(b). The plated Au of the dipole arm and matching network is shown in Figure 3.7(c, d).

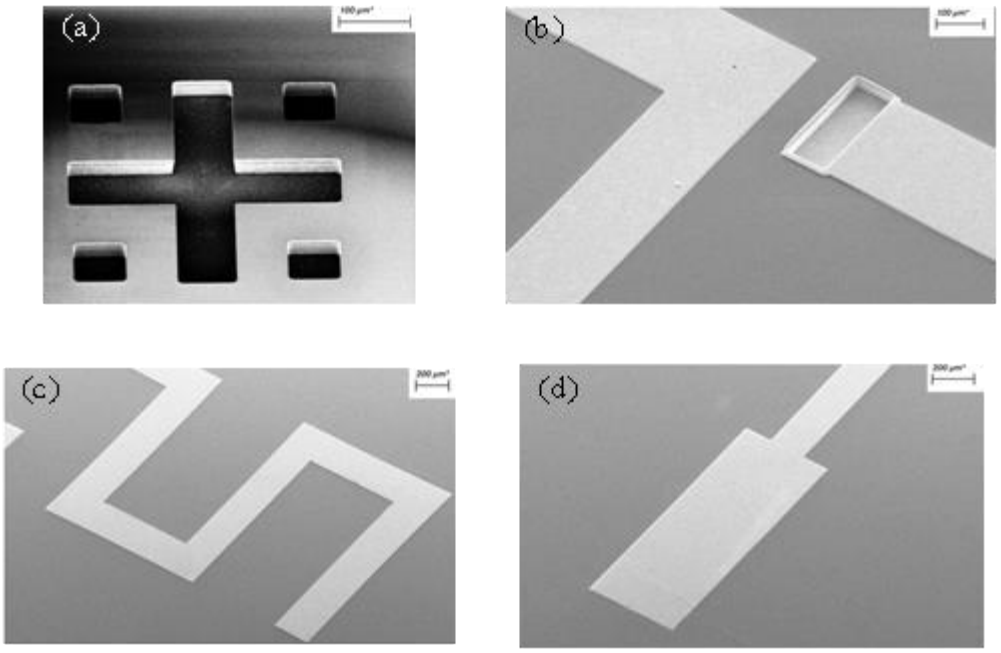

Figure 3.7 Antenna pictures under SEM. (a) Align marker. (b) Plated Au on the via hole and front side. (c) Plated Au of the antenna arm. (d) Plated Au of matching network.

3.4 Micro-machined 3D Antenna Measurement

After the antenna is connected to the mini SMP signal pin by silver expoy, the antenna assembly is fixed in a plastic rotation holder and placed in a microwave test chamber. The antenna gain can be calculated using S21 based on the Friis formula:

$$P_r = \frac{G_t G_r \lambda^2}{(4\pi R)^2} P_t \tag{3.1}$$

P_r and P_t are respectively receiving power and transmitting, of which the ratio can be measured by S21 ($S21^2=P_r/P_t$). R is the distance between the transmitting antenna and the antenna under test. The transmitting antenna in this measurement is the standard gain Satimo dual ridge antenna (see Figure 3.8). The S11 and gain are measured using a ZVA67 VNA after calibration.

Figure 3.9 shows the comparison between the measured and simulated reflection coefficient of the cube antenna with and without the additional 3D-printed holder and rotation stage. As seen, additional metal and lossy plastic parts could affect antenna efficiency and bandwidth. Although the resonant frequency shifts up by hundreds of megahertz, the measured data fit the simulated data.

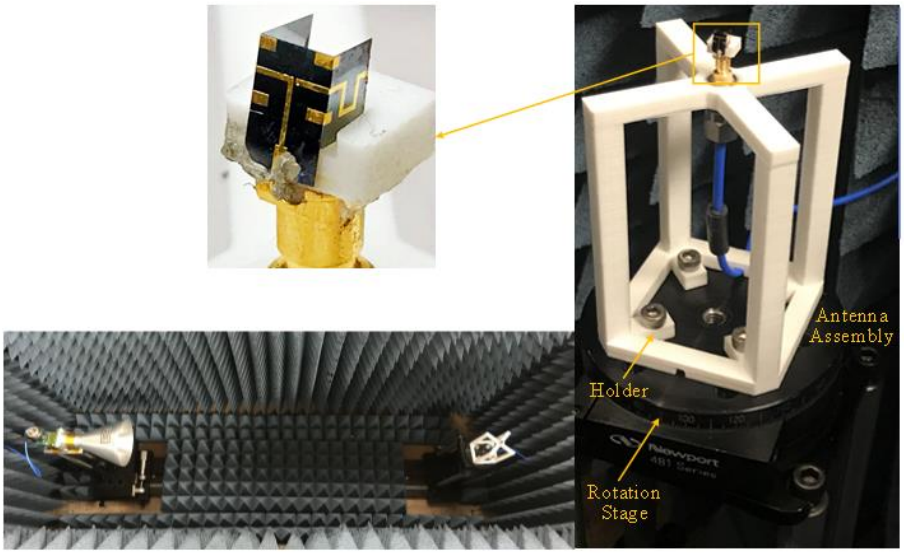

Figure 3.8 Antenna Measurement Setup.

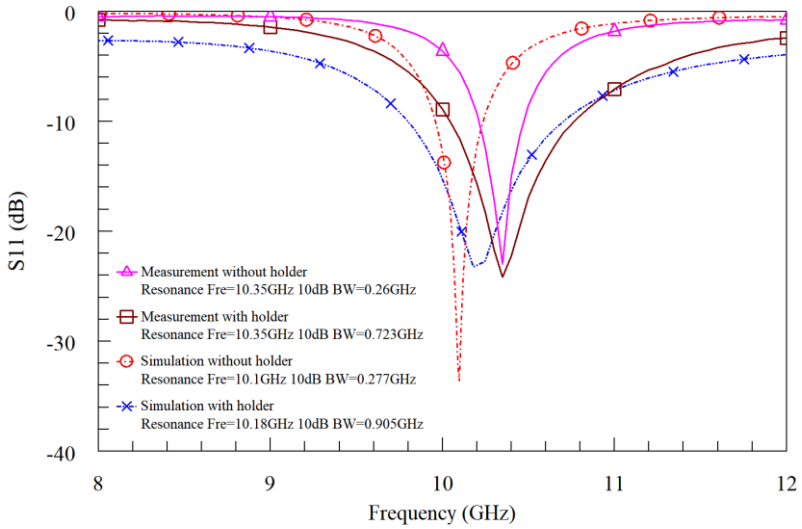

Figure 3.9 Simulated and Measured S11.

The comparison method is used to determine the antenna gain and radiation pattern. The antenna under test and a standard gain antenna in the microwave chamber are connected to a vector network analyzer. Fig. 2.9 shows the simulated and measured radiation patterns. The measured maximum gain is -3.5 dBi on E-plane and -1.38 dBi on H-plane. Although measured radiation patterns show more loss than simulated, the shape of the pattern is similar.

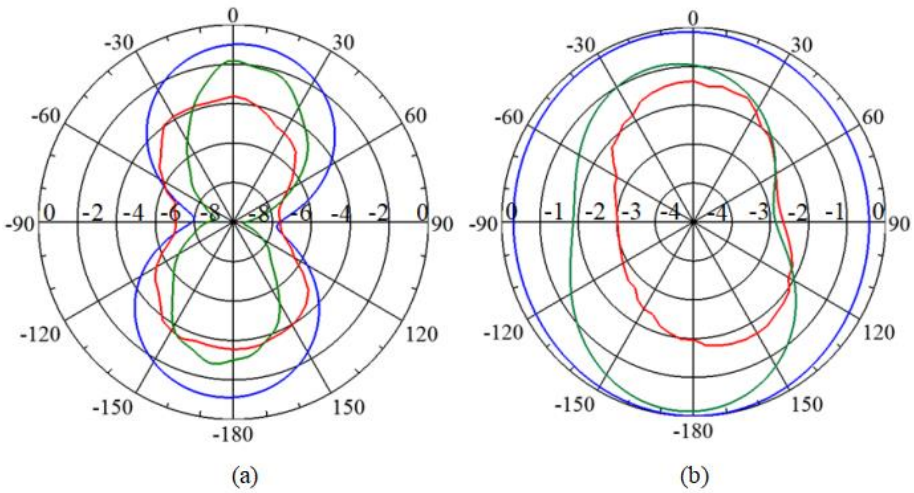

Figure 3.10 Measured Radiation Pattern of Cube Antenna (in dB).
(a) E-Plane Radiation Pattern. (b) H-Plane Radiation Pattern. (Blue line: simulation without the holder, green line: simulation with the holder, red line: measured radiation pattern).

Efficiency can be obtained by using the Wheeler Cap method [141]. The basic concept of Wheeler's method is to use the "radian sphere," which is the boundary between the near field and the far field of any small antenna to reject the radiation of the antenna under test. The radiation efficiency can be introduced by radiation power directly proportional to input power, where the input power is a combination parameter of radiation power and Ohmic loss power. Thus, if the loss mechanisms of the antenna can be modeled as a lossy resistance R_L in the equivalent RLC circuit of the antenna, the effect of the cap is shorting out the radiation resistance, allowing R_L to be separated from R_R. In this case the antenna can be represented as a series RLC circuit (See Figure 3.11(a)), such as the dipole antenna. In [142], there are two methods for the computation of the antenna efficiency based on the Wheeler cap. The first one is the constant-power-loss method for the electrically small antennas (<λ/10), this method assumes that the radiation resistance is small and the power lost in the lossy resistance is about the same whether the cap is in place or removed:

$$1 - \Gamma_1^2 = \frac{P_{Rad}+P_{Loss}}{P_{Total}} \text{ (Without cap)} \tag{3.2}$$

$$1 - \Gamma_2^2 = \frac{P_{Loss}}{P_{Total}} \text{ (With cap)} \tag{3.3}$$

$$\eta = \frac{P_{Rad}}{P_{Total}} = \frac{|\Gamma_2|^2-|\Gamma_1|^2}{1-|\Gamma_1|^2} \tag{3.4}$$

where P_{Rad} is the total radiated power, P_{Loss} is the loss power, P_{Total} is the total power input, Γ_1 is the reflection coefficient without Wheeler cap (measure in free space), Γ_2 is the reflection coefficient measurement with Wheeler cap.

And the second one is the constant-loss-resistor method for the moderate-length antennas which makes use of the quantities R_{Rad} and R_{Loss} in the Figure 3.11(a), given by

$$\eta = \frac{P_R}{P_{Total}} = \frac{R_{Rad}}{R_{Rad}+R_{Loss}} = \frac{(1-\Gamma_1)(1+\Gamma_2)}{(1+\Gamma_1)(1-\Gamma_2)} \tag{3.5}$$

where R_{Rad} is the radiation resistance, and R_{Loss} is the loss resistance.

The Wheeler cap in this measurement is made by a bullet shell with 9.5mm diameter and 15mm height, of which its radius is in the near field of the antenna. The cap is connected well to the ground of the SMP connector by a copper plane. As shown in Figure 3.11(b), the reflection coefficient without the Wheeler cap is -0.06 (S11= -24.12 dB), the reflection coefficient with the Wheeler cap is -0.757 (S11= -2.41 dB at 10.35 GHz (resonance frequency). Thus, the antenna efficiency is 55.8% at 10.35 GHz using the constant-power-loss Wheeler Cap method (Equation 3.2), and efficiency from 8-12 GHz is shown in Figure 3.11(c).

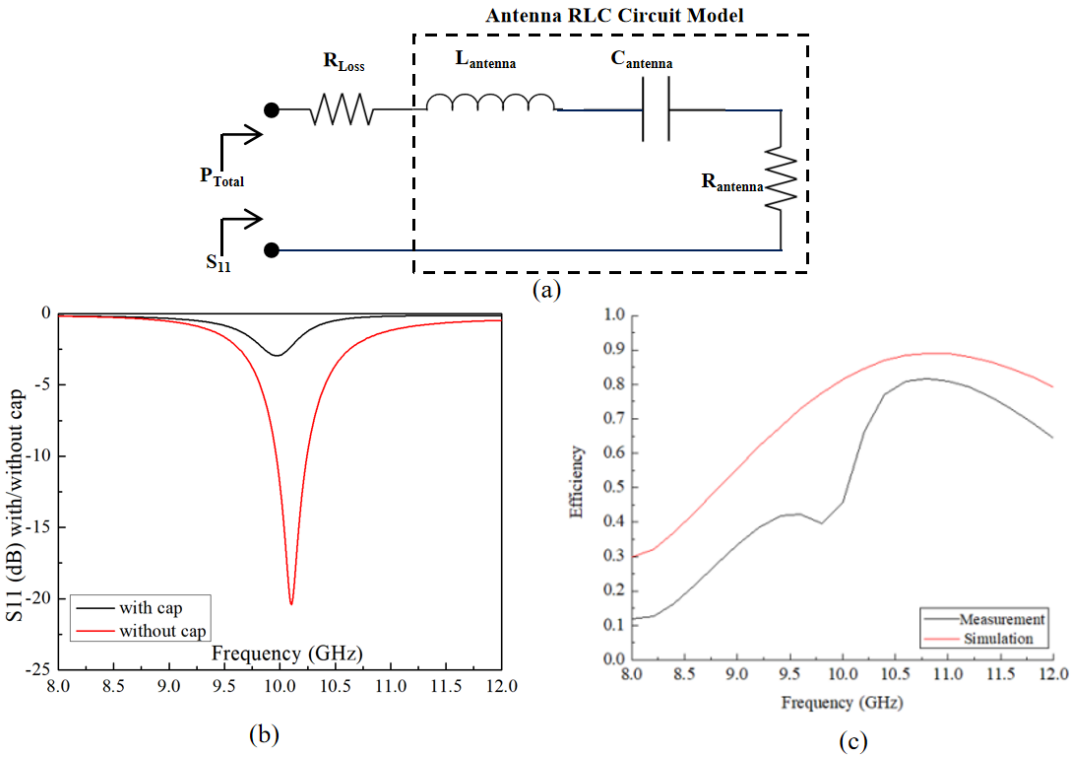

Figure 3.11 Antenna efficiency measurement. (a) Antenna circuit model with lossy resistance, (b) Measured S11 with/without the metal cap, (c) Simulated and measured efficiency.

For the constant-power-loss method, it should be noted that the measurements must be made at resonance, because the loss model is based on S_{11} values that are all-real, even though only their magnitudes are needed in the above equations [142]. Besides, efficiency cannot be measured

accurately by simply comparing input resistance when the AUT has a complicated parasitic. Paper [143] builds an antenna circuit model with parasitic resistance and reactance, the S11 with cap in this paper shows a kink with increasing of the parasitic reactance, which is similar to the measurement in Figure 3.11(b). The input impedance of the AUT in free space is 43.75Ω and the input impedance of the AUT with the cap is 7 Ω-5.15jΩ. Thus, additional reactance and parasitic is the reason that the measured antenna efficiency is inaccurate at no resonance frequencies because of the characteristic of the Wheeler cap method.

3.5 Analysis and Conclusion

This work first designs a 3D foldable antenna working for X-band (10 GHz) IoT ICs and provides a packaging solution for the chip. Since this design adopts a combination of 3D geometry and meandered line technology, the omnidirectional antenna in this work is electrically small (antennas with dimensions substantially smaller than a wavelength), and it can conserve overall IoT system volume and mass.

Table 3.1 shows a comparison between the micro-machined 3D meandered-line antenna in this work and other work on 3D antennas: For the 3D printing technology in [144], [145], [146] and other papers using non-micromachined methods [147], [148], the metal choice is limited (silver paste or silver ink) and metal used in standard fabrication methods, such as Au, Ni, and Ti, has not to be reported in 3D-printed antenna design. And some of the metal processing methods are not as precise as lithography. In [144], several traces are printed on the cube surface then electrically conductive adhesive (ECA) is filled into the traces. This hand-made method results in a 200 MHz frequency shift between simulation and measurement.

As discussed in Table 2.1, 3D printing technology has limited printing resolution, surface roughness, and low permittivity substrate (ε_r=2.98 in [144]). Thus, the 3D-printed antenna dimension is larger than the Silicon-based antennas using thinner wafers and more precise standard fabrication methods. The currently available substrate materials for 3D printing are also lossy relative to the other commercial microwave substrates (e.g., loss tangent=0.045 in [146]).

Paper [149] shows a 3D antenna assembled by planar antennas with silver epoxy. Although the planar antennas are fabricated by standard fabrication methods, the assembly is still made by uncontrollable hand-made methods. Paper [150] gives a 3D solution by folding Rogers/RT Duroid

6010. However, it cannot be generalized to most commercial substrates, such as FR-4 and Silicon.

Although this design has advantages in small resolution and dimensions, there are still some challenges with the micro-machined 3D antenna in this work. For the assembly of the 3D antenna, the hand assembly by tweezers, including soldering and assembling in a plastic holder, needs to be retired by a more precise method [151]. For example, the silver epoxy soldering generates a piece of irregularly shaped conductor at the antenna feed. Wire bonding technology could be another integration solution to replace silver epoxy. Considering a more precise assembly, it is also worth having a high-precision holder. As shown in Chapter 3, the gap in the 3D printed plastic holder is 60 μm. Due to the resolution limit of the 3D printer in the lab, the actual width of the gap is over 200 μm. This 3D printing resolution results in the assembly error and folding error.

In conclusion, this chapter designs an antenna working for X-band communication ICs and provides a packaging solution for the chip. Since this design adopts meandered line technology, *ka* is small compared to antennas in papers in Table 3.1. This design's beauty is that the dimensions of the antenna, including antenna arms, balun, and matching lines, can be redesigned for ICs with different dimensions. Changing the balun and the matching line's size will make the input impedance match to 50 Ohm at different frequencies. Thus, this design is ideal for most IC chip dimensions at the microwave frequency range.

Table 3.1 Antenna Performance Comparison

Paper	*ka**	Antenna type	Fabrication Method	Frequency	Performance
[144]	16.3	Dipole	NinjaFlex by 3D printing	2.6 GHz	10 dB RL BW: ~7.7%
[145]	2.5	Monopole	Glass and inkjet printing	1.7 GHz	10 dB RL BW: 12.6% Efficiency: 66%
[146]	4.9	Patch antenna	Foldable polymers by 3D printing Silver conductive ink	3.3-3.7 GHz	10 dB RL BW: 4.3% Peak gain: 4.2 dBi
[147]	2.5	Quasi-Yagi antenna	PET flexible substrate Silver conductive ink	2.45 GHz ISM band	10 dB RL BW: 10% Peak gain: 5.96 dBi
[148]	1.75	Dipole	PCB and Pyralux	2.45 GHz ISM band	Peak gain:2 dBi 10 dB RL BW: 2.7%
[149]	NA	Coil antenna	Standard fab method and silver epoxy	374MHz	NA
[150]	0.73 0.55	Dipole	PCB and stereolithography	2.45 GHz ISM band	Peak gain:2 dBi Efficiency: 78% 10 dB RL BW: 2.7%
This work	0.54	Dipole	Silicon processing	X-band (10 GHz)	Peak gain: -1.38 dBi Efficiency: 55.8% 10 dB RL BW: 7%

Chapter 4

4. Micro-machined Waveguide-fed Planar Antennas for THz applications

At THz frequencies (0.1-10 THz), a variety of integrated circuits (ICs) have been proposed for applications that are discussed in Chapter 1, such as communications, medical imaging and spectroscopy, remote sensing, and materials research [99]. All these aspects put more demands on innovations in THz antenna design and integration methods with THz transceivers.

At millimeter-wave frequencies, there is sufficient space for the horizontal integration of the "antenna on PCB" [100],[101] (See Figure 4.1(a)). However, with increasing frequency, the approach of vertical integration with smaller dimensions using the antenna-in-package (AiP) shown in Figure 4.1(b) provides a useful alternative to "antenna on PCB," e.g., a 64-element antenna array for D band communication [103], a phased array mixing silicon and III-V chiplets [104], and an 89 GHz superstrate antenna stacking an antenna layer directly on the back side of a silicon-based IC [105]. Furthermore, to overcome increasing cost and losses of flip-chip bonding [107], the system-on-chip (SoC) approach has triggered significant interest, as it allows on-chip integration of digital baseband and complete RF front-ends (See Figure 4.1(c)), the examples of this approach are described in Section 2.5.

There are still challenges to the silicon-based SoC approach at mm-wave and THz frequency because typical commercial CMOS technology substrates have low resistivity (10 Ω -cm) [152]. Due to the small distance in the CMOS process (≈15 μm [153]) between the top metal and Si substrate and the low resistivity of the Si substrate, the radiated fields find a low resistance path through the substrate and a significant percentage of the radiated fields are absorbed. This results in a drastic degradation in the antenna's gain and efficiency. One approach to address this problem is to adopt a silicon-on-insulator (SOI) substrate (>10k Ω -cm) with a high-resistivity device layer as a platform for both integrated circuits and antennas [154].

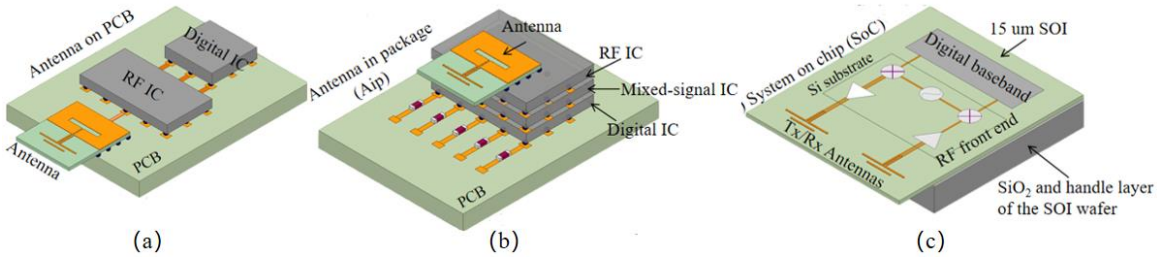

Figure 4.1 Implementation diagram of (a) antenna on PCB, (b) antenna in package (AiP), (c) system on chip (SoC) using the example of the quasi-Yagi antenna on 15 um SOI designed in this chapter.

Even with a high-resistivity substrate, there remain several challenges to achieving high-efficiency antennas. The first challenge with integrating THz antennas on-chip is that more power tends to be radiated into the dielectric substrate than into the air at approximately a ratio of $\varepsilon_r^{3/2}$:1 [155]. This effect can cause significant energy loss and decrease antenna radiation efficiency. In addition, the number of higher-order modes in the substrate also increases with the thickness of the substrate. For example, the normalized cutoff frequency of TM^z_m and TE^z_m modes in an ungrounded dielectric slab waveguide is given by [156]:

$$(f_c)_m = \frac{m}{4h\sqrt{\varepsilon_d \mu_d - \varepsilon_0 \mu_0}} \quad \text{m=0,1,2,3…} \tag{4.1}$$

where h is the half thickness of the substrate.

It can be seen that the cutoff frequency of a given mode is a function of the electrical constitutive parameters of the dielectric slab and its height. The modes are referred to as odd modes (when m = 0, 2, 4, ...), and even modes (when m = 1, 3, 5, ...). The dominant mode is the TM_0, of which the cutoff frequency is zero. Other higher-order modes can be cut off by selecting a smaller operation frequency or thinner substrates. For example, TM_1 and TE_1 modes in a silicon dielectric slab waveguide are suppressed only when the substrate thickness is thinner than 152 μm at 300 GHz. For broadside antennas (e.g., slot or dipole), this effect can be mitigated through using a dielectric spherical lens with an impedance matching layer [157]. However, a different solution is needed for end-fire antennas (e.g., tapered slot or quasi-Yagi in this paper). Some papers reduce the substrate modes by using low-permittivity substrates [158], electromagnetic band gap (EBG) materials [159] and backside-etching processing [160].

The second challenge is to measure planar antenna characteristics of AiP and SoC at the mm-wave frequency and THz range. One typical measurement setup is to mount the antenna fed by a GSG probe on a probe station. Some papers use absorbers [161] and low-permittivity chuck [162] to reduce the reflections caused by the probe station. Still, the probe-station-based measurement is susceptible to EM reflections from the environment, and only the radiation pattern in the upper half-space is measurable due to the metal stages. The other method uses coax connectors [163], waveguides [164], or other extending structures to hold the antenna in the free space so that the radiation patterns can be measured in both the upper and lower half-spaces. This free space measurement works for antennas fed by a probe up to 325 GHz [165]. However, it still has challenges in stabilizing the antenna chip and firmly fixing the extended structure [166]. Papers [167],[168] integrate antennas with diodes for this free space radiation pattern measurement, but it's hard for this geometry to measure the antenna performance, such as S11 and peak gain.

To suppress high-order modes, the antenna design in this paper is realized using a silicon-on-insulator (SOI) substrate with a 15-μm thick device layer and a micro-machining process that includes silicon processing and plated via-holes with metallization of front and backside [169]. This micro-machined SOI processing has multiple advantages including 1) the ability to effectively utilize electrically thin substrates (e.g., 15-mm silicon is < $\lambda_d/10$ to over 500 GHz); 2) the ability to selectively remove substrate to reduce coupling to substrate modes. (In this paper, the silicon substrate surrounding the two tapered slots of the TSA and the loop antenna radiator is selectively removed for substrate mode reduction); and 3) the ability to integrate via-holes and both front-side and back-side metallization that enables straightforward integration of antenna radiators, baluns, and matching networks. In addition, silicon substrates have good mechanical performance compared to other substrates like quartz and Gallium Arsenide, such as large elastic modulus (E=185 GPa) and yield strength (σ_{yield}=4500 MPa) compared to other substrate like single crystalline quartz (E=97 GPa, σ_{yield}=1700 MPa) and Gallium Arsenide (E=118 GPa, σ_{yield}=85 MPa) [170],[171], which is one of the reasons that thin silicon substrates are used for micro-machined THz probes [172]. Besides, the antenna chips shown in Figure 4.1 can be viewed as a model of a cantilever beam for the analysis of maximum stress and chip deflection. It has been proved that silicon can generate the most force and provide the most deflection before failure, as indicated by the higher modulus of resilience [173].The measured antenna performance in this paper demonstrates that the 15-μm SOI is a good platform for packaging and antenna integration methods for millimeter-wave and THz ICs shown in Figure 4.1. The antenna chip uses an E-plane probe to transfer power from the chip to waveguide. The geometry benefits the antenna measurement because 1) THz test equipment most commonly has a waveguide interface, such as VDI VNA extenders, and 2) the antenna under test doesn't need to be placed on the test stage and can be rotated flexibly.

Another benefit is that the antenna chips can be replaceable to generate different far fields based on variable demands using a single probe housing. Figure 4.2 shows different applications and demands on antenna design. And this idea gives a flexible solution for these demands, including reconfiguration of radiation patterns and resonance frequency, efficiency improvement, and integration with ICs. Moreover, different THz applications can be achieved using one waveguide-feed probe housing and antennas with different functions. THz antennas have a wide range of applications, including THz communications, spectroscopy, and imaging. For example, the quasi-Yagi chip designed in this work with WR2.2 probe housing is a good end-fire antenna for THz transceivers, and the TSA chip with the same probe housing can be used to receive signals at a certain direction since it has higher gain and less narrow main lobes than the quasi-Yagi antenna.

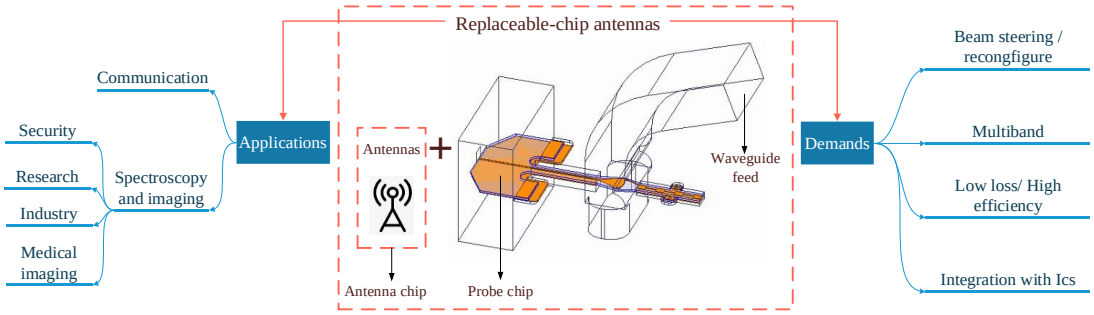

Figure 4.2 Concept of replaceable-chip antennas.

The chapter is organized as follows. First, Section 4.1 explains how the E-plane probes and the proposed geometry work. Section 4.2 approaches silicon and metal micro-machined processing to realize substrate mode reduction. Next, antenna design and simulation are shown in Section 4.3, including quasi-Yagi antenna, tapered slot antenna, and loop antenna. Then the antenna measurements and analysis are shown in Section 4.4, including return loss, gain, and radiation patterns. Finally, conclusions are drawn in Section 4.5.

4.1 Integration Method with Waveguide

THz planar antennas are designed for THz systems and modules, such as ICs and other on-wafer devices. However, devices such as signal detectors and high-quality-factor (HQ) filters based on waveguide technology are also required. Furthermore, THz test equipment most commonly has a waveguide interface due to low loss and simple integration of different devices. Thus, integration between the planar antenna feed and the metallic waveguide is necessary.

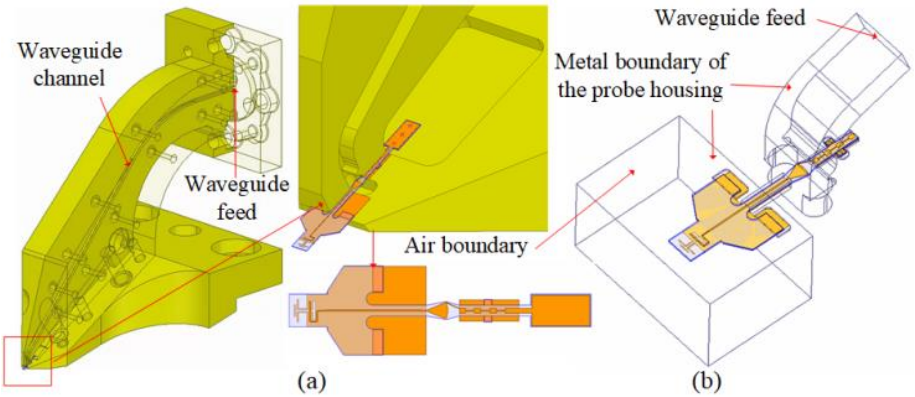

Figure 4.3 Geometry of integration with waveguide by E-plane probe. (a) quasi-Yagi antenna chip at 330-500 GHz with WR2.2 probe housing, (b) HFSS simulation of the whole antenna assembly.

This work shows a method for integration between THz planar antennas and waveguide-fed devices. Figure 4.3 shows how this idea works using the example of a quasi-Yagi antenna at 330-500 GHz and the WR2.2 T-wave probe housing made by Dominion MicroProbes Inc. (DMPI). A WR 2.2 probe housing with the designed antenna is shown in Figure 4.3(a). The antenna chip consists of an antenna working at WR 2.2, the E-plane probe, and the low-pass filter. Figure 4.3(b) shows the HFSS simulation with the boundary of waveguide and air.

Fig. 4 gives a more detailed description of how this integration method works. It shows the simulation of the integration between E-plane probes and waveguides. In Figure 4.4(a), a fan-shaped E-plane probe is designed to integrate with WR 2.2 waveguide. Similarly, Figure 4.4(b) shows the

simulation geometry for the E-plane probe working at 125-200 GHz. The operating frequency of the WR5 waveguide is 140-220 GHz. The integration can start from 120 GHz since the WR5 waveguide cutoff frequency is 110 GHz. In HFSS, the metal probe housing is set up as the metal boundary, and other boundaries are set up as air. The waveguide port of the two simulations is set up as a wave port with 2-inches de-embedding to simulate the actual phase results. For the E-plane probe at 330-500 GHz, it can be seen that the insertion loss is smaller than 4 dB and the return loss of the waveguide port and microstrip port is better than 15 dB. For the E-plane probe at 125-200 GHz, this design has larger than 2.5 dB insertion loss and smaller than 13 dB return loss in this frequency range.

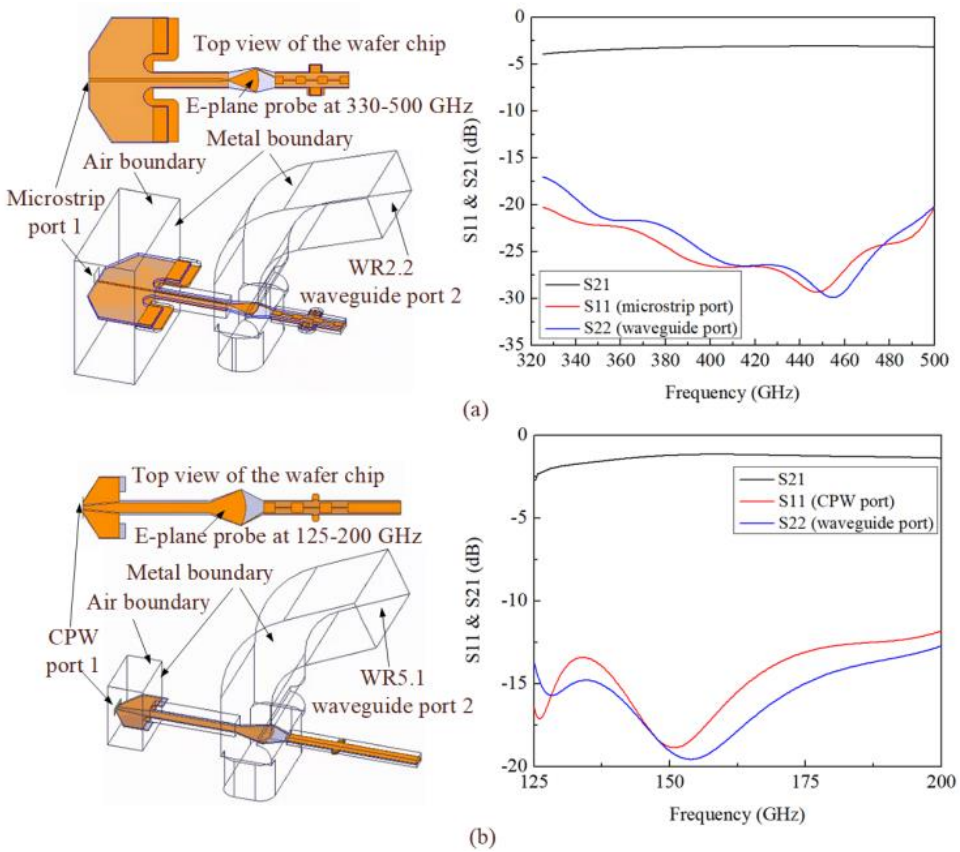

Figure 4.4 Simulation of integration with waveguide by E-plane probe.
(a) E-plane probe at 330-500 GHz, (b) E-plane probe at 125-200 GHz.

This design of the E-plane probe and T-wave probe housing can be a good solution for integration with the waveguide, and this geometry can be a good template for the THz 50Ω-fed microstrip or CPW planar antennas since the CPW port and microstrip port in Figure 4.4 are well matched to 50 Ω based on the HFSS simulation results. Fabrication methods for the silicon chip are shown in the next section.

4.2 THz Antenna Design

In this section, a quasi-Yagi antenna, a tapered slot antenna (TSA), and a loop antenna at WR2.2 (325-500 GHz) are designed based on Marchand balun and fed by a 50Ω microstrip line, and a CPW-fed quasi-Yagi antenna is designed at WR6.5 (110-170 GHz).

4.2.1 Quasi-Yagi Antenna at 130 GHz and 330-500 GHz

The Yagi-Uda antenna was invented in 1926 by Yagi and Uda. Quasi-Yagi antennas comprise a single radiator, a reflector, and one or more directors [174]. These antennas are capable of end-fire radiation with high gain and front-to-back ratio (FBR). In order to maximize the gain and FBR of quasi-Yagi antenna, many researchers work on optimization of the element's geometry and the spacing among elements [175], [176], [177]. Another effort is to improve the bandwidth performance by feeding network design, such as the MS-to-CPS transition [178], CPW-to-CPS transition [179], [180], CPS-to-SL transition [181], and MS-to-SL structure [182].

Before the antenna design, a Marchand balun is designed for conversion between an unbalanced input signal and balanced output signals, a transition between microstrip line and slot lines, and impedance matching. The conventional Marchand balun [183] and the Marchand balun in this project [169] are shown in Figure 4.5(a)&(b). It provides balanced signals across the load impedances Z_L at the two output ports when driven from an unbalanced signal at the input port. The ideal balun operation can be characterized in terms of the S21 and S31 with the same amplitude and 180^o phase difference (See Figure 4.5 (c)&(d)). Similarly, for the transition between CPW and slot line for the CPW-fed quasi-Yagi antenna at 130 GHz, a quarter-wave-long balun is design to generate two outputs with the same amplitude and 180^o phase difference (See Figure 4.6 (c)&(d)).

This work designs a Silicon-based CPW-fed quasi-Yagi antenna at 130 GHz and a microstrip-

fed quasi-Yagi antenna at 330-500 GHz. The CPW-feed quasi-Yagi antenna shown in Figure 4.5(a) consists of a director element, a half-wavelength dipole as a driven element, and the CPW ground as the reflector. One slot line in the CPW is terminated by a quarter of the wavelength open-circuited stub so that the two slot lines have a 180-degree phase difference. Two pairs of via holes are connected at the other side of the substrate to keep the two ground planes at the same potential and suppress parasitic modes generated by discontinuity [184], [185]. The length of the driven, the director and the reflector elements is around $0.5\lambda_{eff}$, $0.16\lambda_{eff}$ and $0.75\lambda_{eff}$ at 130 GHz. The antenna resonances at 130 GHz with the 50 Ω input impedance and at 165 GHz with the 72 Ω input impedance.

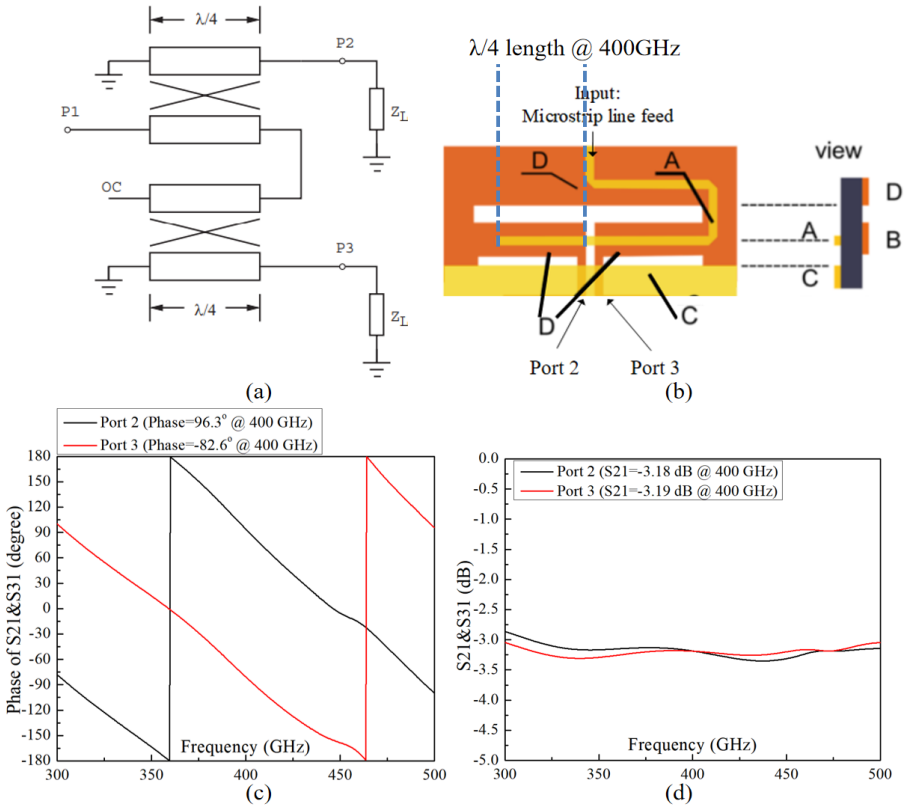

Figure 4.5 Marchand Balun. (a) conventional Marchand balun [183], (b) Marchand geometry, (c) S21&S31 amplitude simulation, (d) S21&S31 Phase difference simulation.

Similarly, the microstrip-fed quasi-Yagi antenna has a $0.5\lambda_{eff}$ driven element, $0.3\lambda_{eff}$ director and $0.6\lambda_{eff}$ ground reflector at 400 GHz. In addition, this antenna is fed by a Marchand balun with an

asymmetric coupling structure proposed by [139]. The balun consists of two sections of quarter-wave-long couplers employed to achieve two outputs with the same magnitude and 180 degrees out of phase. Figure 4.5(b) shows the antenna geometry and S11 simulation, of which the 10 dB bandwidth is 357-500 GHz.

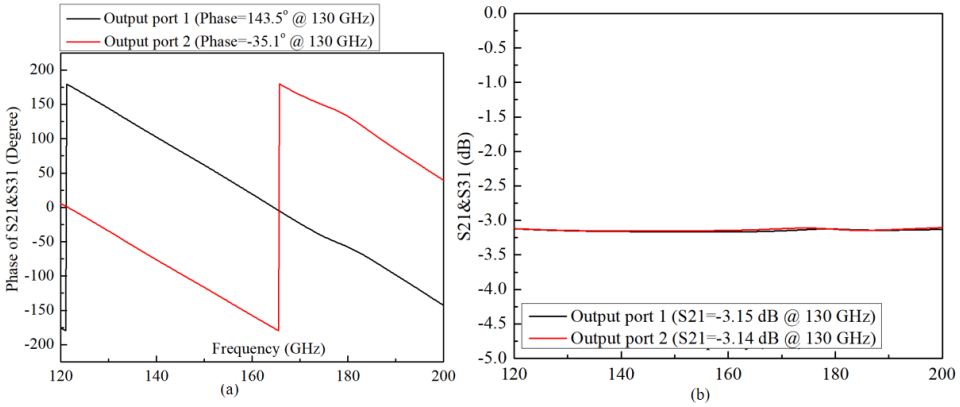

Figure 4.6 Quarter-wave-long Balun. (a) S21&S31 phase difference simulation, (b) S21&S31 amplitude simulation.

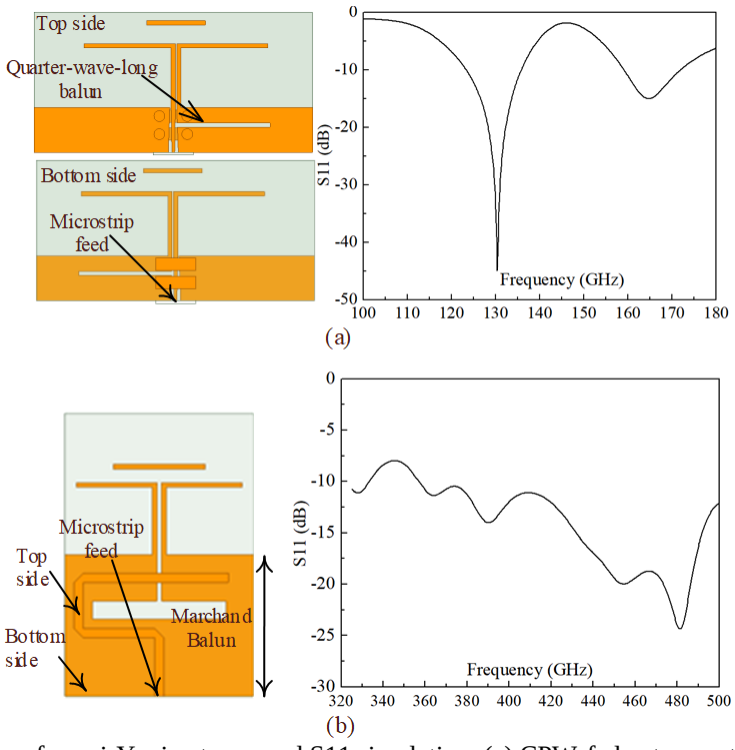

Figure 4.7 Geometry of quasi-Yagi antenna and S11 simulation. (a) CPW-fed antenna at 130 and 165 GHz, (b) microstrip-fed antenna at 330-500 GHz.

4.2.2 Tapered Slot Antenna (TSA) at 330-500 GHz

Tapered slot antennas (TSA) are typical examples of planar antennas for millimeter-wave and THz applications such as phased arrays and focal plane imaging systems due to their compact wide bandwidth and end-fire radiation pattern [186]. TSA was first developed by Gibson [187], and one important improvement was introduced by Sugawara [188] by using Fermi-type tapering to reduce the side lobes. Corrugated edges were also introduced to reduce the width of the TSA without degradation in radiation patterns [189]. There are several types of TSA with different shapes of tapered sections, such as LTSA (Linear Tapered Slot Antenna), Vivaldi (Exponentially Tapered Slot Antenna), and CTSA (Constant Tapered Slot Antenna) [190], [191].

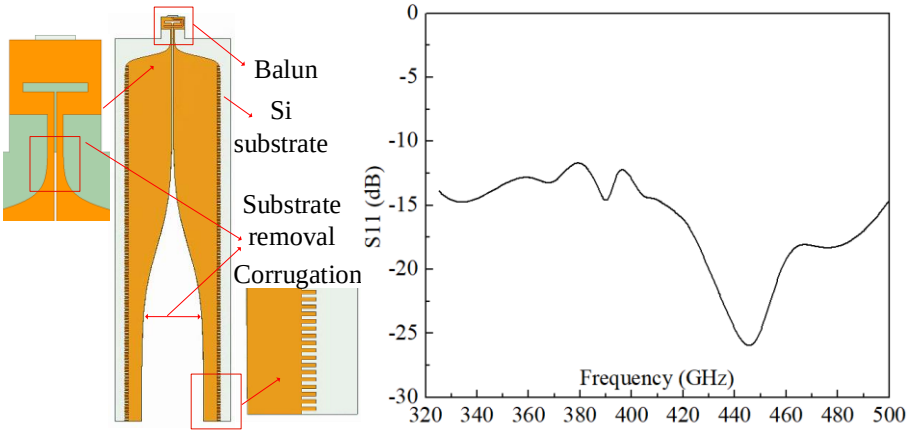

Figure 4.8 Geometry of tapered slot antenna and S11 simulation.

Tapered slot antennas have nearly symmetrical radiation patterns, but the H-plane side lobes for these antennas are higher than those in E-plane. The resulting patterns of the TSA with the Fermi-Dirac function have more symmetrical patterns and have low sidelobe levels than others [189].

The width of the TSA measured from the aperture edge to the substrate edge is suggested to be larger than 2 λ_0, as the E-plane side lobe level of a narrower width TSA was higher than for the wider antenna, and the main beam in the H-plane was broader. This degradation in the radiation pattern,

which is associated with reduced antenna width, is a significant problem for the design of compact TSAs [189]. However, antenna width reduction is necessary when forming antenna arrays, especially for mm-wave and THz imaging applications. Thus, this work uses a corrugation structure that consists of a periodic arrangement of slits on the sides of the TSA radiator. The antenna length is 4 λ_0 with the 0.1 λ_0 length and 0.025 λ_0 width corrugation. As shown in Figure 4.8, the designed TSA is fed by Marchand balun, the same as the balun for the microstrip-fed quasi-Yagi antenna. The Silicon substrate between two tapered slots is etched for the disruption of the substrate for antenna gain improvement. More details on gain simulation and measurement are shown in Section 4.4.

4.2.3 Loop Antenna at 330-500 GHz

Loop antennas are used in a variety of far-field and near-field applications such as communication systems [192], energy harvesting [193], RFID [194], and near electrical field detection [195]. This work designs a loop antenna with 1-λ_0 perimeter at 460 GHz (see Figure 4.9). Half of the antenna loop is fabricated on the front side of the substrate, and the other half is on the backside. The loop is fed by a parallel-plate balun and microstrip line. The Si substrate in the central ring is removed to improve antenna gain. The simulated S11 shows the loop antenna resonance at 330 and 460 GHz.

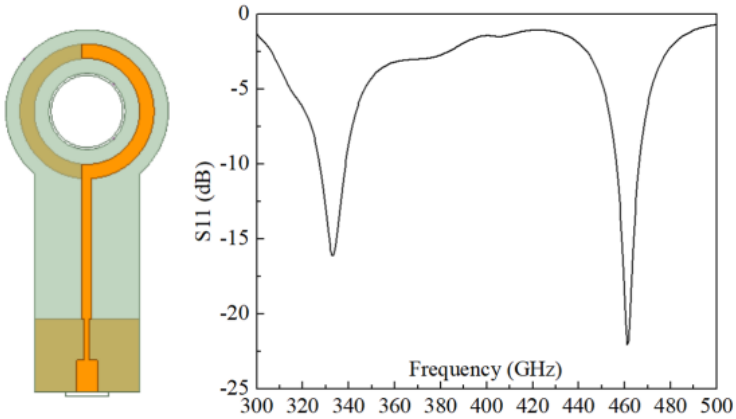

Figure 4.9 Geometry of loop antenna and S11 simulation.

4.3 SOI Processing Fabrication for Antennas

Planar antenna on dielectric substrate suffers from power loss because of substrate modes. The coupling efficiency between the antenna and the substrate medium increases with increasing high-order modes. This work shows several antennas based on micro-machined silicon-on-insulator (SOI) processing to reduce substrate modes. The SOI wafers used in this design consist of a 450μm handle layer, 1μm oxide layer, and 15μm high resistivity (ε_r=11.8) device layer (15μm=0.0065 λ_0@130 GHz=0.02 λ_0@400 GHz). Based on calculations from previous work, this substrate thickness can suppress TM_1, TE_1, and higher-order modes and improve antenna gain and efficiency.

The fabrication process follows the process flow shown in Figure 4.10. On a clean SOI wafer, the via holes and alignment markers are first etched for front-side Au plating and backside lithography patterning (see Figure 4.10(a, b)). AZ4330 photoresist is used for both front-side and backside lithography. It gives about 3.3 μm thick photoresist at 4krpm spin speed. In Figure 4.11, via holes with 12 μm radius are etched in this step.

After a Ti-Au-Ti seedlayer deposition, the front-side Au is plated (See Figure 4.10(c)) up to 1.5μm thick. For the gold plating lithography, it needs to be emphasized that these via holes introduce regional variations in photoresist thickness and make the extra photoresist inside the via holes not able to be developed by the normal UV exposure power. The solution in the cube antenna project in Chapter 3 is to use negative PR in which the photoresist openings are the "dark" part of the lithography mask. Another solution for positive PR AZ4330 is a "two-step" lithography. The first step defines the photoresist patterns for the front-side plating gold circuit. The second step provides extra exposure to the via hole regions using the mask of via hole etching. The front-side gold plating

lithography resolves critical features as small as 12 μm in width (see Figure 4.11). This residue photoresist in the via hole can also be cleaned by an oxygen plasma in the March cleaning tool, but the plasma cleaning makes the PR in the undeveloped area uneven, which makes the plated gold thickness harder to be measured by the step analyzer.

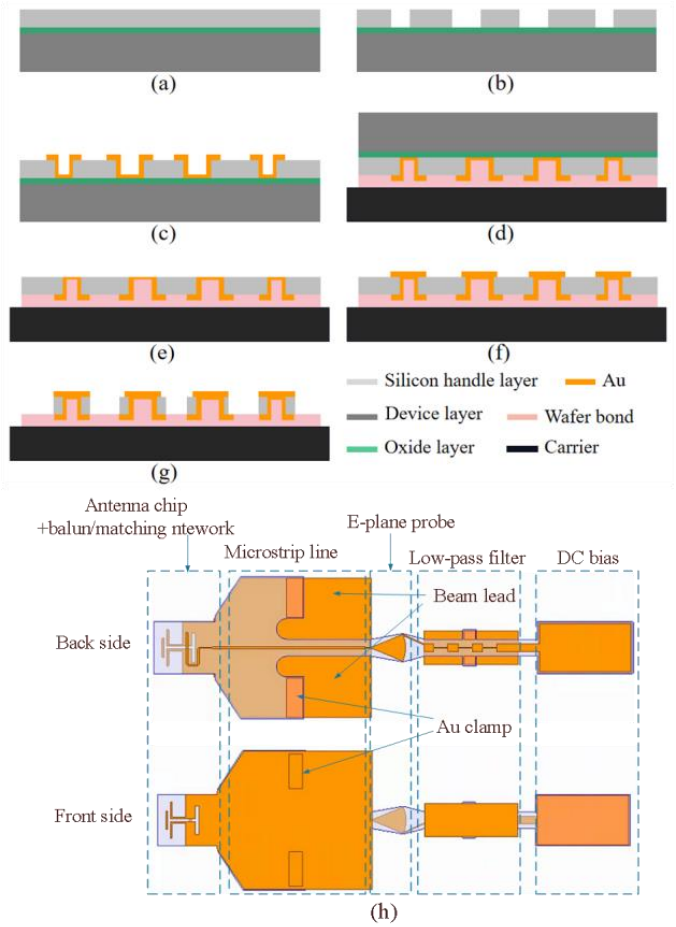

Figure 4.10 Antenna chip fabrication flow using micro-machined SOI processes technologies.(a) wafer cleaning, (b) via hole etch, (c) front-side plating Au antenna definition, (d) backside mounting of the SOI wafer, (e) the handle and the oxide layer removal, (f) backside plating Au antenna definition, (g) extents etch for probe contour definition, (h) antenna chip geometry (Quasi-Yagi antenna is used as an example).

An additional gold clamp is plated after gold plating for the antenna radiator. The reason is that the probe housing does not fully close as designed. The probe inside the block is not firmly clamped by the block and moves slightly during the probing process. The clamp gold (10 μm thickness gold)

and beam lead region are designed to provide extra plated gold to the clamp regions to solve this issue, as well as to avoid thick gold features for both front-side and backside RF circuitry [139]. They provide enough thickness of gold in the clamp regions for the probe to be firmly clamped by the probe block when assembled.

Then the wafer is flipped over and mounted to a carrier wafer with wafer bond and epoxy (See Figure 4.10(d)). The 450 μm thick handle layer removal is achieved by dicing and RIE plasma etching. The dicing tool uses a 0.5 mm wide blade to dice across the whole SOI wafer cut by cut, removing up to 420 μm thickness of the handle layer. Then the wafer is etched using the RIE plasma etching recipe to remove the remaining silicon. The Si etching is very selective between Si and silicon oxide and will stop at the oxide layer. After the handle layer is thoroughly removed, the wafer is soaked in BOE to strip the oxide layer. Similarly, the BOE wet etch is highly selective between silicon oxide and Si.

After the oxide layer removal, the alignment markers and the vias are clearly revealed at the backside of the device Si layer (See Figure 4.10(e)). The backside Au plating for the antenna radiator and clamp is the same as the plating process on the front side (See Figure 4.10(f)). The last step is Si etching to define individual antenna chips, and then all chips are released by wafer bond remover. In this step, the Silicon substrate between two tapered slots of the TSA and the inner loop substrate of the loop antenna is etched to release waves confined in the substrate. Figure 4.10(h) shows a quasi-Yagi antenna at 330-500 GHz chip fabricated using SOI processing.

The images of antenna chips after the substrate etching and the final release under the microscope and Scanning Electron Microscope (SEM) are shown in Figure 4.11~ Figure 4.14. As shown in these figures, gold plating lithography can resolve critical features as small as 12μm in

width. Additionally, the SEM image in Figure 4.11 confirms that the anisotropic silicon etch recipe for via etch gives a straight and clean sidewall. The beamlead region looks crumpled because it is a free-standing 1.5-μm thickness Au film. The misalignment of Au plating lithography shown in Figure 4.11 results in resonance frequency shift. More analysis on antenna measurement will be discussed in the next sections.

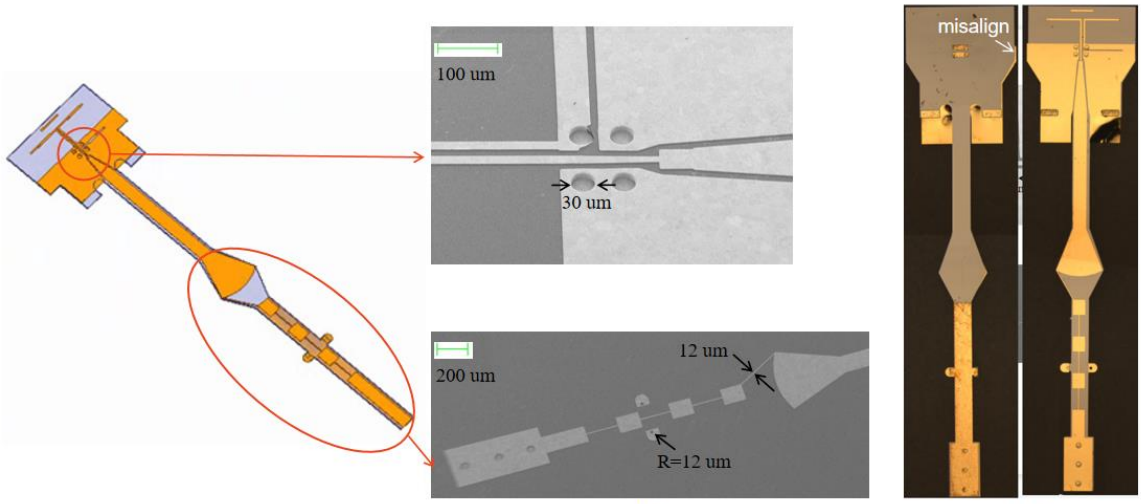

Figure 4.11 130 GHz quasi-Yagi antenna pictures (a) Antenna geometry in HFSS, (b) pictures under SEM, (c) pictures under microscope.

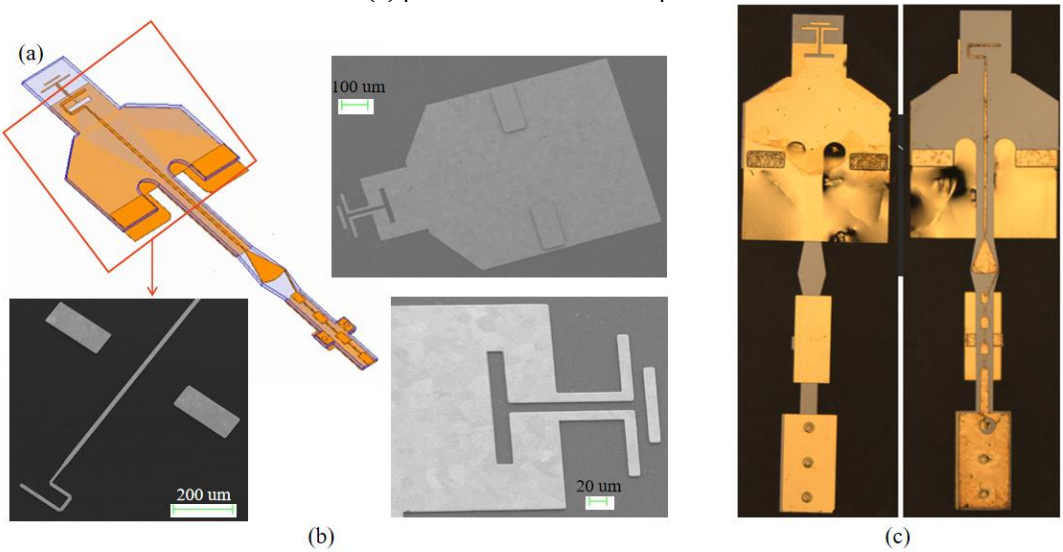

Figure 4.12 WR2.2 quasi-Yagi antenna pictures (a) Antenna geometry in HFSS, (b) pictures under SEM, (c) pictures under microscope.

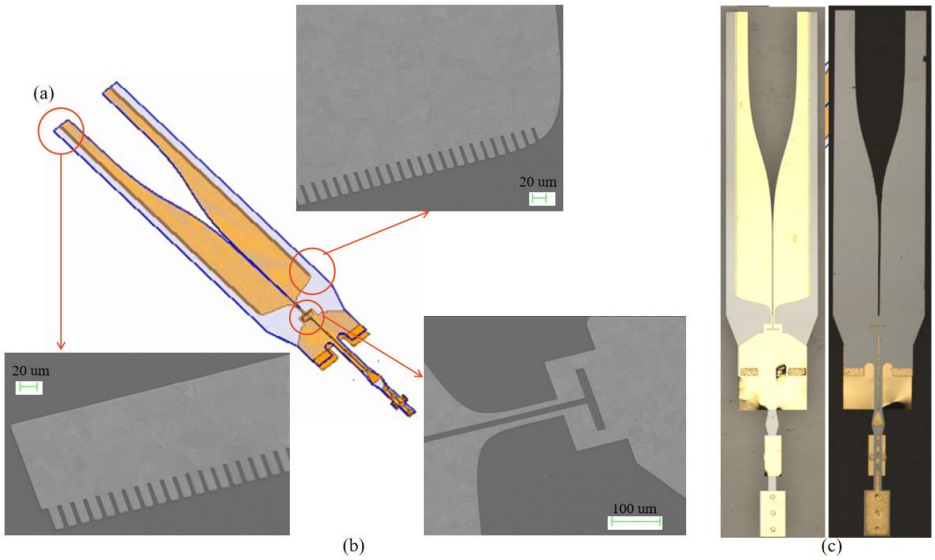

Figure 4.13 WR2.2 tapered slot antenna pictures (a) Antenna geometry in HFSS, (b) pictures under SEM, (c) pictures under microscope.

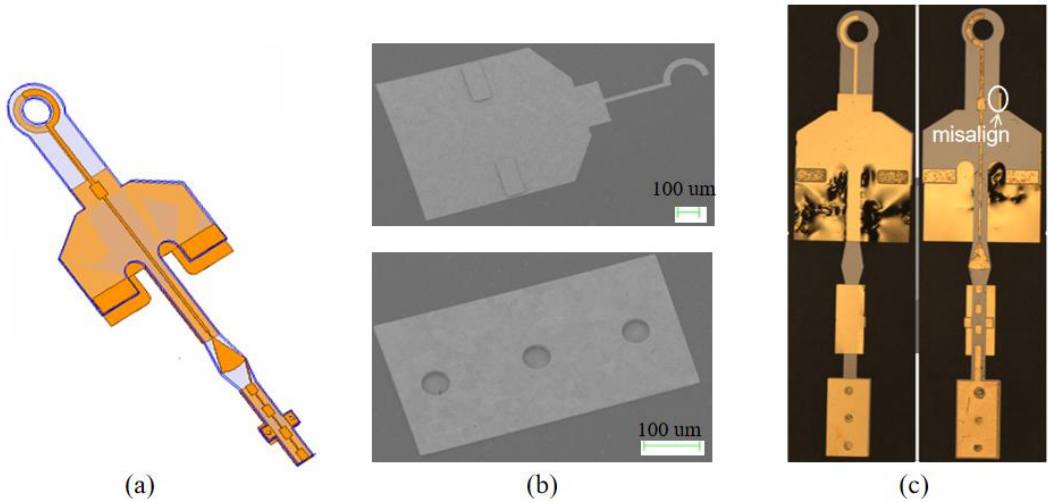

Figure 4.14 WR2.2 loop antenna pictures (a) Antenna geometry in HFSS, (b) pictures under SEM, (c) pictures under microscope.

4.4 Micro-machined Waveguide-fed Planar Antennas Measurement

4.4.1 Antenna Return Loss and Gain Measurement

The S11 and gain are measured using ZVA67 VNA and WR5.1/WR2.2 VDI extender modules after TOSM (Thru/Offset-Short/Short/Match) calibration at the waveguide port of the VDI extenders. As shown in Figure 4.15, the antenna gain can be calculated using S21 based on the Friis formula with a standard gain horn antenna from Virginia Diodes, Inc (VDI). The extender with antenna chip and probe housing is rotated 30 degrees to align the peak gain direction with the horn antenna.

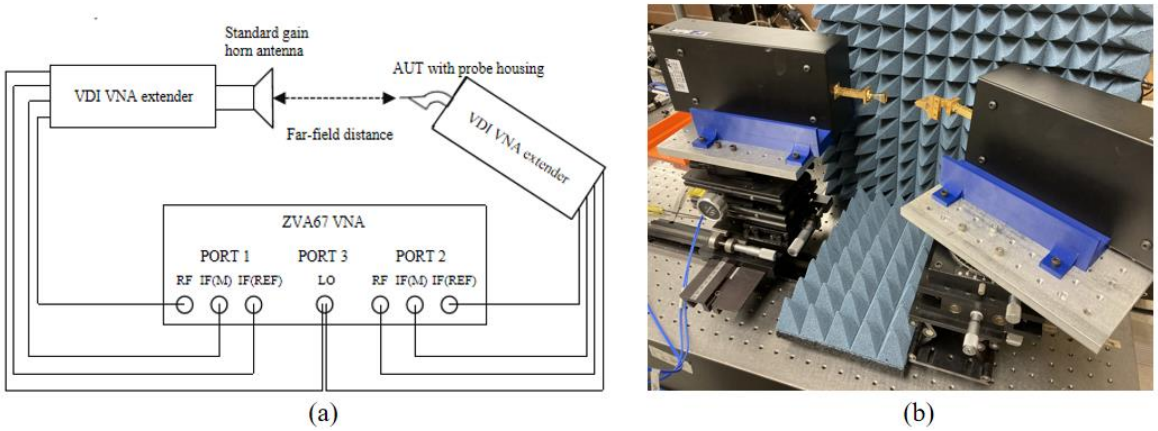

Figure 4.15 Antenna gain measurement setup.

The waveguide loss is the dominant loss in the antenna measurement. Before antenna return loss and gain measurement, the return loss of the WR5.1 probe housing and a WR2.2 probe housing without the antenna chips is measured to calculate the waveguide loss of the 2-inch probe housing, which is the dominant loss in the gain measurement. Half of the measured S11 is the loss (S21) of this 2-port structure since the other side of the probe housing can be viewed as “open”. The WR5.1 probe housing has 1.2 dB loss at 130 GHz and 0.43 dB loss at 174 GHz, and the WR2.2 probe

housing has 1.5-2 dB loss from 330-500 GHz (See Figure 4.16). All measurement plots in this section are the measured antenna gain with the waveguide loss. The metal loss (attenuation) of the TE_{10} mode in a rectangular waveguide with a×b dimension can also be predicted by [196],

$$(\alpha_c)TE_{mn} = \frac{2*8.686/\sigma\delta}{b\eta\sqrt{1-\frac{f_{mn}^2}{f^2}}}\left\{\left(1+\frac{b}{a}\right)\frac{f_{mn}^2}{f^2}+\left(1-\frac{f_{mn}^2}{f^2}\right)\left[\frac{\frac{b}{a}\left(\frac{b}{a}m^2+n^2\right)}{\frac{b^2}{a^2}m^2+n^2}\right]\right\} \quad (4.2)$$

Where m=1, n=0, metal conductivity $\sigma_{Au}=4.52\times10^7$ S/m, δ is the skin depth at WR5 and WR2 frequency range, WR5 rectangular waveguide dimension is 1.295mm×0.648mm (cut-off frequency of TE_{10}: 115.75 GHz), WR2 rectangular waveguide dimension is 0.559mm×0.279mm (cut-off frequency of TE_{10}: 268.15 GHz).

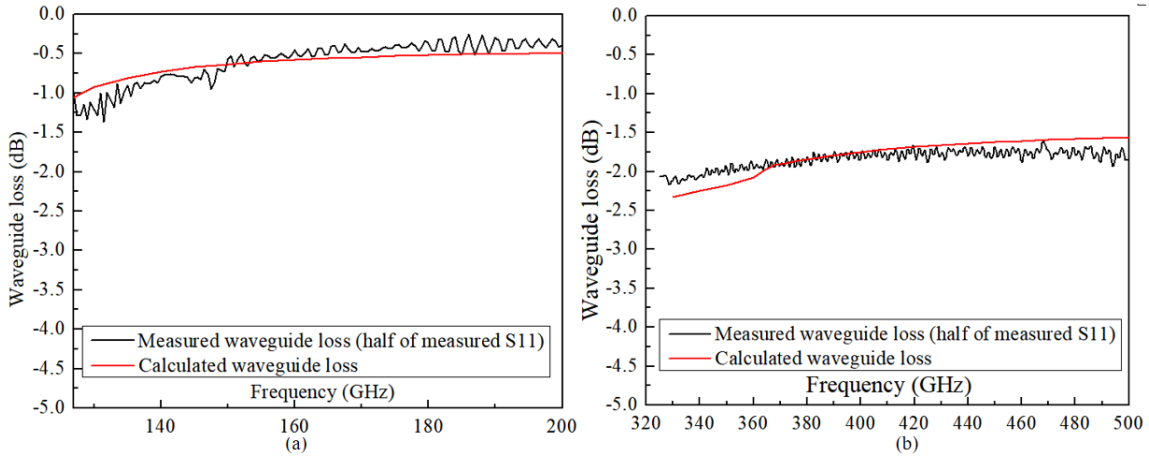

Figure 4.16 Calculated loss and measured S11 of the "Open" probe housing for loss analysis. (a) WR5 probe housing, (b) WR2 probe housing.

The calculated loss of WR5 waveguide is 0.9 dB at 130 GHz and 0.52 dB at 174 GHz, the calculated loss of WR2 waveguide is 1.75 dB at 400 GHz. The measured loss matches the calculation as shown in Figure 4.16 The far-field distance between the 130 GHz quasi-Yagi antenna and the horn antenna is 40 cm. The three-antenna method based on the Friis transmission formula with a pyramidal horn antenna and a conical horn antenna is adopted in Figure 4.17. It requires measuring three combinations of three antennas to provide three equations with three unknowns. The WR6 pyramidal

horn antenna with 32mm×16mm aperture size has 23.4 dB calculated gain [197] and 19.3 dB measured gain at 170 GHz. The WR6 conical horn antenna with 10.8 mm aperture diameter has 23.6 dB calculated gain [197] and 21.5 dB measured gain at 170 GHz, which is close to the data provided by Virginia Diode Inc (21 dB). In Figure 4.18, the S11 10 dB bandwidth of the quasi-Yagi antenna with WR5.1 probe housing is 128-133.5 GHz and 168-181 GHz, and it has 1.76 dB and 3.44 dB gain at 131 GHz and 172 GHz.

For the antennas measured with WR2.2 horn antenna, the S21 is measured three times when the distance between two antennas is 5cm, 8cm, and 10cm to reduce measurement errors. The quasi-Yagi with WR2.2 probe housing has 10 dB bandwidth from 374-500 GHz and has a 3.24 dB peak gain at 465 GHz (Figure 4.19). Figure 4.20 shows the measured return loss of TSA is below -10 dB across the entire band, and it has a 9.31 dB peak gain at 371 GHz and 5 dB lowest gain at 489 GHz. It can also be seen that the antenna gain can be improved by Si substrate removal based on the simulated gain with and without the partial Si removal.

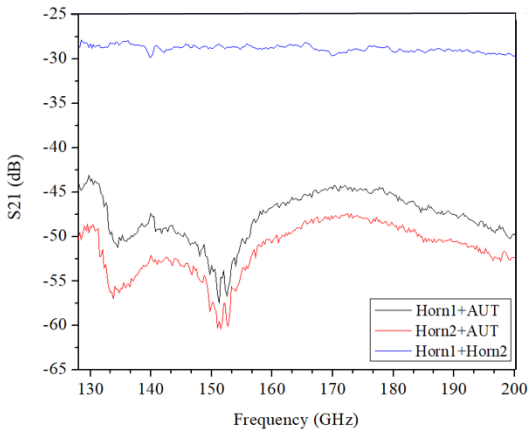

Figure 4.17 Measured S21 of the quasi-Yagi antenna using three-antenna measurement.

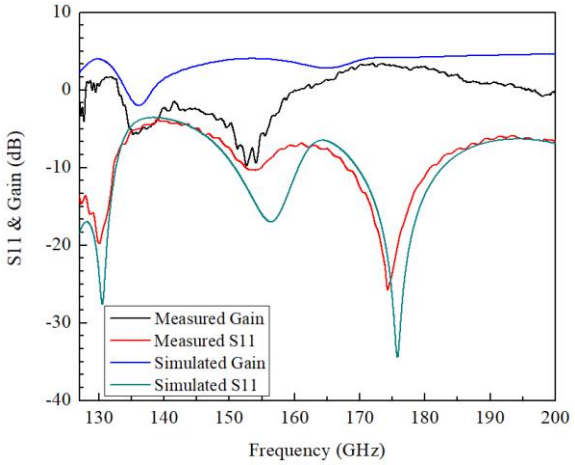

Figure 4.18 S11 and gain of the quasi-Yagi antenna with WR5 probe housing.

Since the loop antenna has a 1-λ_0 perimeter at 460 GHz and its current is not uniform, the direction of the peak gain varies over the WR2.2 band. The radiation patterns are simulated to determine the peak gain direction at 10 GHz steps. Next, the VNA extender with the loop antenna is rotated at the corresponding degrees to align its peak gain direction to the horn antenna for peak gain measurement. As shown in Figure 4.21, the rotation scale is defined from 90°-270° in this peak gain measurement and radiation patterns measurement. For example, the loop antenna resonates at 340 GHz, at which the peak gain degree is 82° on the H plane, and the peak gain degree is 128° on the H plane when the antenna resonates at 450 GHz.

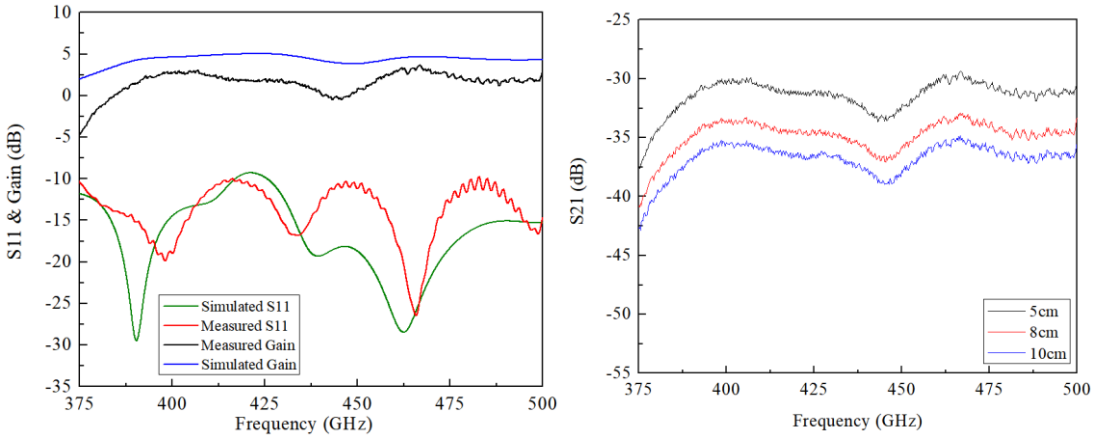

Figure 4.19 S11 and gain of the quasi-Yagi antenna with WR2 probe housing. (a) Simulation and measurement, (b) Measured S21 at three different distances.

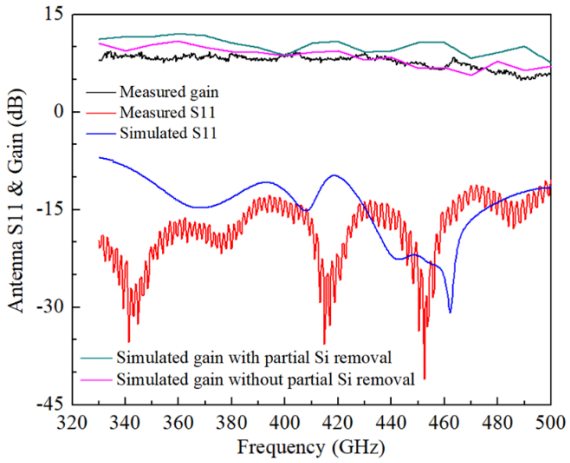

Figure 4.20 S11 and gain of the TSA with WR2 probe housing.

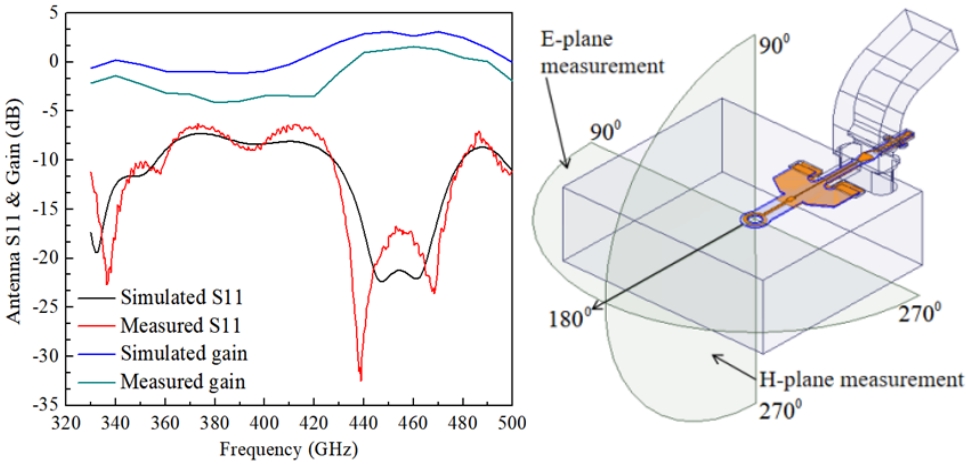

Figure 4.21 S11 and gain of the loop antenna and the corresponding coordinate.

4.2.2 Antenna Radiation Pattern Measurement

This work measures the antenna radiation pattern using amplitude modulation (AM) instead of the antenna under test (AUT) with VNA extenders since the extenders are too large to be rotated around the AUT phase center. In the radiation pattern measurement setup shown in Figure 4.22, a THz carrier frequency with a modulated 1 kHz signal is generated by a VDI WR9 SGX modulator and transmitted by a standard gain horn antenna. VDI WR9 SGX modulator is a 9-times multiplier

with an 80-130 GHz output frequency range. To measure radiation patterns of the CPW-fed quasi-Yagi at 130 GHz, the 130 GHz modulated frequency can be achieved using a 14.44 GHz input signal. Another doubler and a 9.44 GHz input are used to generate a 174 GHz (9.44×9×2=174 GHz) output signal for pattern measurement at another resonance frequency of the CPW-fed quasi-Yagi. Two doublers are adopted for the WR2.2 antennas. The AUT with a signal detector is set up on a rotation stage at the receiving side. The demodulated signal voltage is measured by the SR510 lock-in amplifier. The normalized radiation patterns with 5-degree steps are plotted by rotating the stage. The degree scale for the pattern measurement is the same as the peak gain measurement shown in Figure 4.21.

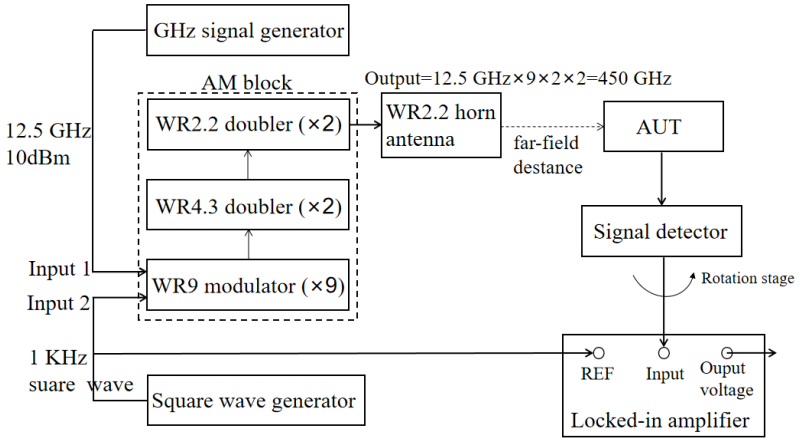

Figure 4.22 Antenna radiation pattern measurement setup using AM modulation with 450 GHz carrier frequency and 1 kHz modulated signal.

Figure 4.23 and Figure 4.24 shows how the rotation stages work. Transmitting and receiving stages are placed on moveable tracks. Stages 1&2, consisting of rotation stages and movement axis for XYZ directions, are used to align AUT with the horn antenna. The AUT with the signal detector is placed on stage 3 by a plastic holder. The AUT phase center is aligned with the center of stage 2 by stage 3. The normalized radiation patterns of the four antennas are shown in Table 4.1. The patterns of quasi-Yagi antennas and TSA are nearly symmetrical. The ripples at the main lobes in some patterns might result from the reflection from the metal housing at back side. Due to the

performance of the large loop antenna with nonuniform current, the loop antenna peak gain direction is not on the horizontal plane in Figure 4.21. Thus, the azimuth plane patterns at 340 GHz and 450 GHz are measured instead of E-plane patterns and are normalized using peak gain. The main lobes of all pattern measurement match the simulation. Table 4.2 shows a summary of the simulation and measurement. The measured gain at some frequencies is higher than the simulation because of the reflection from the metal housing at backside. The metal boundary at backside in HFSS is smaller than the real size.

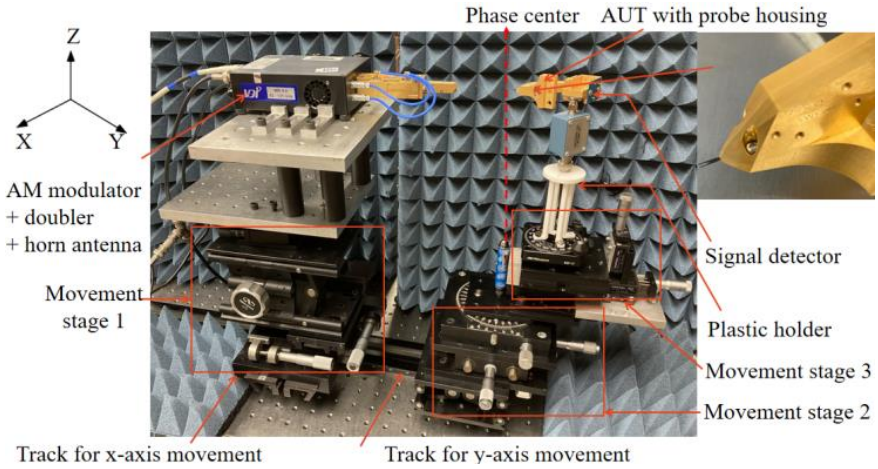

Figure 4.23 Picture of H-plane radiation pattern measurement setup of tapered slot antenna.


Figure 4.24 Picture of E-plane radiation pattern measurement setup of the WR5 quasi-Yagi.

Table 4.1 Measurement of the antenna normalized radiation patterns

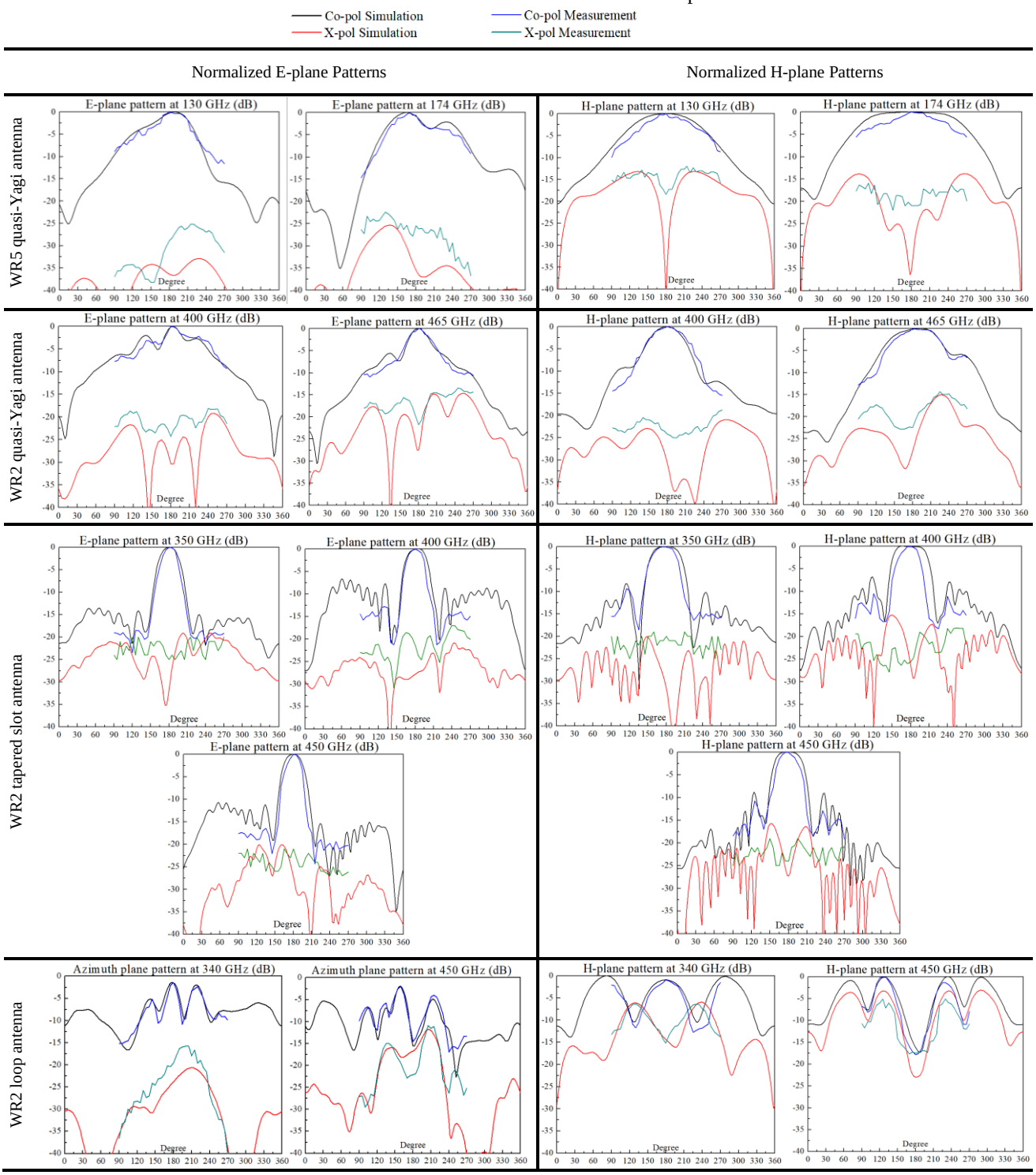

Table 4.2 Summary of the antenna simulation and measurement

Antenna type	Performance	Simulation	Measurement*
WR5 quasi-Yagi	S11 10dB bandwidth	123.8-132.6 GHz, 170-182.7 GHz	128-133.5 GHz, 168-181 GHz
	Gain (dBi)	4.3@ 132 GHz, 4.16@ 172 GHz	3.12@ 132 GHz, 3.9@ 172 GHz
	Co-polarization	Measured main lobes match simulation.	
	X-polarization	15~50 dB< Co-pol	15~35 dB< Co-pol
WR2 quasi-Yagi	S11 10dB bandwidth	369-500 GHz	375-500 GHz
	Gain (dBi)	4.6@ 400 GHz, 4.6@ 465 GHz	4.39@ 400 GHz, 4.77@ 465 GHz
	Co-polarization	Measured main lobes match simulation.	
	X-polarization	15~60 dB< Co-pol	15~25 dB< Co-pol
WR2 TSA	S11 10dB bandwidth	330-500 GHz	330-500 GHz
	Gain (dBi)	10.6@ 400 GHz, 6.7@ 450 GHz	6.64-11.24
	Co-polarization	Measured main lobes match simulation.	
	X-polarization	20~50 dB< Co-pol	20~30 dB< Co-pol
WR2 loop antenna	S11 10dB bandwidth	330-356 GHz, 427-478 GHz	330-360 GHz, 427-480 GHz
	Gain (dBi)	0.17@ 400 GHz, 3.07@ 450 GHz	1.65@ 400 GHz, 4.6@ 465 GHz
	Co-polarization	Measured main lobes match simulation.	
	X-polarization	5~40 dB< Co-pol	8~25 dB< Co-pol

*The antenna gain in this work in Table 2 is the gain added the waveguide loss back.

Besides, there is a 0.7~2.5 dB gain reduction between simulation and measurement. The main reason for the gain difference is the loss in the waveguide discussed above. The WR5.1 probe housing has 1.2 dB loss at 130 GHz and 0.43 dB loss at 174 GHz, and the WR2 probe housing has 1.5-2 dB loss from 330-500 GHz, which matches the gain reduction. The measured surface roughness of the plated Au is less than 100 nm (see Figure 4.25). This result has little impact on the gain decrease in simulation.

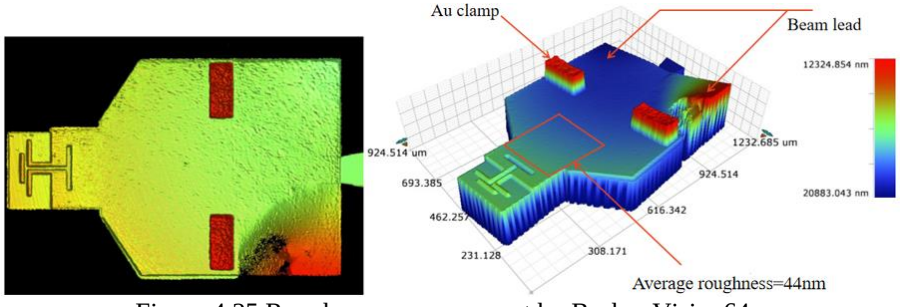

Figure 4.25 Roughness measurement by Bruker Vision64.

4.5 Conclusion

This project shows a quasi-Yagi antenna, tapered slot antenna, and loop antenna design for potential THz applications. THz communication is one typical application for the three antennas because the antenna design in this project has wide bandwidth at THz and is a good platform to be integrated with the front-end chip. There are many previous works on the three antennas for the THz communication SoC design. Papers [198], [199] show the quasi-Yagi antenna design based on CMOS technology at 60 GHz and 100 GHz. Compared to the quasi-Yagi antenna, the tapered slot antenna with wider bandwidth is a better choice for a dual-band communication antenna, for example, a TSA at 120 GHz and 300 GHz with 10 Gbit/s link performance [200]. The TSA for communication is also designed as an antenna array [201] since its main lobe is narrow. For the loop antenna for communication applications, decreasing the loop diameter or adding a phase-delay structure is needed in some designs [202] to ensure that the current in the loop is uniform. Thus, more efforts are needed for the loop antenna in this project to meet the requirements of THz communication. Besides, TSA has an application in the THz imaging and detection system because of its high gain and directivity [203]. Moreover, the loop antenna is widely used in far-field and near-field detection systems. For example, a loop antenna is designed as a thermal detector at 910 GHz [204].

Table 4.3 shows a comparison with previous work on micro-machined mm-wave and THz antennas in terms of three main areas: antenna performance, substrate/substrate modes reduction, and antenna measurement methods. For the antenna performance, this project shows the antenna design from 130 GHz to 500 GHz with return loss, gain, and radiation measurement. The good matching between measurement and simulation shows that the SOI-based micro-machined processing method and the integration method with the E-plane probe are efficient methods in THz

antenna design. Furthermore, these two methods can be extended up to 1.1 THz antenna design since the T-wave probe and its fabrication processing have been developed to 1.1 THz.

For the choice of the substrates and methods of substrate mode reduction, some papers on quasi-Yagi antenna and loop antenna fabricated antenna radiators on low-permittivity substrates or multi-layer substrates to reduce substrate modes [205],[207],[216]. Furthermore, papers [206],[209],[215],[217] generate a membrane-supported substrate using backside etching technology (LBE). High-order substrate modes have also been reduced by replacing the substrate dielectric material with an electromagnetic bandgap (EBG) [213], [214]. Compared to these substrates and methods, the 15μm-thickness high-resistivity SOI wafer has these advantages: 1) Considering the antenna performance improvement in the CMOS technology, the high-resistivity silicon is a good platform to integrate antennas with front-end systems. Some substrates in Table 4.3 cannot be used in CMOS technology (RT/duroid) or have low resistivity (GaAs and silicon nitride), 2) the 15um-thickness high-resistivity SOI substrate and the corresponding micro-machined recipes provide the method of fabrication and substrate mode reduction for antenna from 130 GHz to 500 GHz. It can also be a solution to design an antenna up to 1.1 THz. With the increase of frequency, some substrates in Table 4.3 generate higher numbers of substrate modes and some structures need to be redesigned (EBG). However, based on Equation 4.1 discussed above, the 15μm-thickness substrate is thin enough to suppress higher numbers of the substrate modes (TE1 and TM1) up to 3040 GHz [156].

Besides, the silicon substrate surrounding the slot arms of the tapered slot antenna is etched to improve antenna gain and efficiency. Figure 4.20 shows that substrate removal is an efficient method to improve antenna performance for TSA. The simulated antenna gain increases 4 dB after the silicon substrate removal. The substrate surrounding the loop is also removed. Unfortunately, we didn't see significant gain and efficiency improvement in the loop antenna design. The reason is that substrate

removal has a more significant effect on the electrical length and input impedance of the large loop antenna. It's worth designing an electrically small loop antenna in the future work.

Table 4.3 Comparison with existing works on micro-machined mm-wave and THz antennas

Antenna type	Paper	Gain (dBi)*	Bandwidth (GHz)	Substrate Thickness	Methods on substrate mode reduction	Antenna measurement/Feed
Quasi-Yagi antenna	[205]	5	75-95	525 μm glass wafer	Through glass via technology	+/-90º 2D E plane in free space (End-launch connector)
	[206]	3.5-5.1	135-158	9.8 μm SiO2 400 μm Si	Backside-etching cavity	+/-90º 2D E plane with probe station (GSG probe)
	[207]	7 @94 GHz	91-106	100 μm GaAs	NA	No pattern measurement (GSG probe)
	[208]	6.2 (simulated)	110-170	15 μm ABF polymer 100 μm glass	ABF polymer (Ɛr=3.3) + glass	No pattern measurement (GSG probe)
	[209]	5-10	66-81	0.6 μm silicon nitride 0.8 μm SiO2, 350 μm Si	Membrane-supported bulk Si	No pattern measurement (GSG probe)
	This work	3.12@132 GHz, 3.9@172 GHz	123.8-133.5, 168-181	15 μm SOI	Thin substrate	+/-90º 2D E/H plane in free space (Waveguide feed)
	This work	4.39@400 GHz, 4.77@465 GHz	374-500	15 μm SOI	Thin substrate	+/-90º 2D E/H plane in free space (Waveguide feed)
Tapered slot antenna	[210]	10-12	75-110	10 mil RT/duroid 6002	NA	+/-90º 2D E/H plane in free space (W-band connector)
	[211]	NA	75-110	127 μm RT/duroid 5880	NA	+/-120º 2D E/H plane in free space (Coupling slot, E-plane probe)
	[212]	2.8-10	43-140	PolyStrata processing	NA	+/-120º 2D E/H plane in free space (Recta-coax line (RCL))
	[213]	NA	80-110	1.27 mm RT/duroid5880	Electromagnetic band gap (EBG)	+/-90º 2D E/H plane in free space (CPW, integrated with diode)
	[214]	NA	70-110	100 μm Quartz	Electromagnetic band gap (EBG)	+/-90º 2D E/H plane in free space (CPW, integrated with diode)
	This work	6.64-11.24	330-500	15 μm SOI	Thin substrate, silicon removal	+/-90º 2D E/H plane in free space (Waveguide feed)
Loop antenna	[215]	3.44 @340 GHz	330-360	10 μm SiO2, 300 μm Si	Membrane-supported substrate	+/-90º 2D Azimuth/Elevation plane with probe station (GSG probe)
	[216]	4.1	303-320	9.38 μm SiO2, 300 μm Si	9.38 μm SiO2+300 μm Si	+/-90º 2D Azimuth/Elevation plane with probe station (GSG probe)
	[217]	1.5 @29.5 GHz	26.4-40.1	1 μm SiO2, 400 μm Si	BCB oxide (Ɛr=2.65) Back-etched Si	+/-180º 2D Azimuth/Elevation plane with probe station (GSG probe)
	[218]	4.3 @375 GHz (simulated)	365-375	100 μm Quartz, 280 μm Si	NA	+/-60º 2D Azimuth/Elevation plane with probe station (GSG probe)
	[219]	4 @375 GHz (simulated)	250-325	65 nm CMOS	NA	No pattern measurement (On-chip 2×3 ring array)
	This work	1.65@400 GHz, 4.6@465 GHz	330-360, 427-480	15 μm SOI	Thin substrate	+/-90º 2D Azimuth/Elevation plane in free space (waveguide feed)

* The antenna gain in this work in Table 2 is the gain added the waveguide loss back.

Most of antennas in Table 4.3 are CPW-fed with the GSG probe, and this feeding method gives challenges to antenna pattern measurement since such antennas and probe stations cannot be rotated flexibly. Besides, the probe-station-based measurement is susceptible to EM reflections from the environment, and only the radiation pattern in the upper half-space is measurable due to the metal

stages (See Figure 4.26(a)). Some papers [210], [212] show the measured patterns of TSA fed by connectors or coax cables but SMA connectors and coax cables are not ideal feeding types for THz antenna over 100 GHz [220]. Similar to the pattern measurement method by AM modulation in this work, some papers integrate antennas with diodes and other circuits and get good radiation pattern measurement [213],[214],[219],[220] (see Figure 4.26 (b)), but it's hard for this geometry to measure the antenna S11 and peak gain. This project adopts E-plane probes to provide a good transition between planar antennas and waveguides for the more precise antenna gain and radiation pattern measurement.

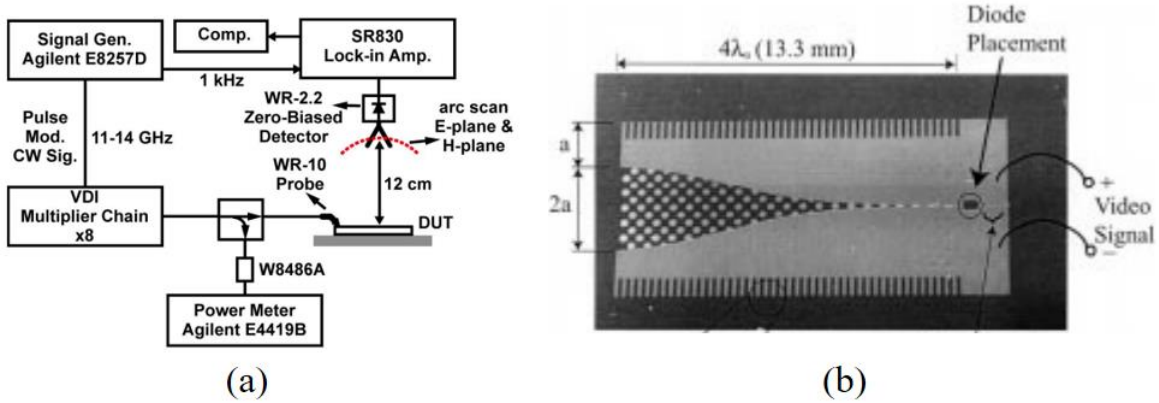

Figure 4.26 Antenna radiation pattern measurement method. (a) [218], (b) [214].

This project designs the micro-machined quasi-Yagi antenna, tapered slot antenna (TSA), and loop antenna at THz frequency. The antennas are fabricated using SOI wafers with 15μm thickness high-resistivity silicon. The thin substrate processing, including substrate etching, reduces the substrate modes, and this 15μm-thickness high-resistivity SOI can be demonstrated as a good platform for the antenna integration for millimeter-wave and THz CMOS technology. Besides, the antenna chips are integrated with T-wave probe housing by E-planes probes for gain and pattern measurement. The measured S11, peak gain, and normalized radiation patterns match the simulation. This integration method with waveguide-fed proves that THz antenna measurement and potential

OTA measurement can get benefit from this geometry. Another beauty of the geometry is that the antenna chips can be replaceable to generate different far fields based on variable demands using a single probe housing.

Chapter 5

5. Conclusion and Future Work

5.1 Conclusion

This work discussed two antenna designs, micro-machined 3D foldable antenna and micro-machined THz antennas. The research in this work is to create antennas needed to extend the capabilities of existing wireless systems and provide them access to the Terahertz region of the spectrum. The core contribution of this work is using micro-machining techniques to create antennas for high-frequency applications, improve antenna performance and develop antenna integration methods.

This work first designs a 3D foldable antenna working for X-band (10 GHz) IoT ICs and provides a packaging solution for the chip. Since this design adopts a combination of 3D geometry and meandered line technology, the omnidirectional antenna in this work is electrically small (antennas with dimensions substantially smaller than a wavelength), and it can conserve overall IoT system volume and mass. The 3D design also helps the antenna to achieve high radiating efficiency while presenting the desired impedance to the transceiver circuits (PA and LNA). The radiation quality factor Q of electrically small antennas is accurately determined by the factor ka discussed in Chapter 3:

$$Q = \frac{1}{k^3 a^3} + \frac{1}{ka} \tag{5.1}$$

The length of each side in this design is 3 mm, so ka=0.54, Q=8, and the fractional bandwidth is 1/Q=12%. This bandwidth is more than sufficient for most microwave applications.

Compared to other "antenna-in-package" integration methods, this design allows maximum use to be made of the available space. Another beauty of this design is that the geometry of the antenna, including 3D shape, antenna arms, balun, and matching line, can be redesigned for ICs with different dimensions. For example, changing the balun and matching line's size will make the input impedance match to 50 Ohm at different frequencies. Thus, this design is ideal for most IC chip dimensions at the microwave frequency range.

This work also designs the micro-machined quasi-Yagi antenna, tapered slot antenna (TSA), and loop antenna at THz frequency. The antennas are fabricated using SOI wafers with 15μm thickness high-resistivity silicon. It has advantages to planar antennas, such as small size and easy fabrication. Meanwhile they also have the capacity for integration with waveguide-fed devices. The thin substrate processing, including substrate etching, reduces the substrate modes, and this 15μm thickness SOI can be demonstrated as a good platform for the packaging and antenna integration for millimeter-wave and THz ICs in the CMOS technology.

In this design, the antenna chips are integrated with T-wave probe housing by E-planes probes for gain and pattern measurement. This integration method with waveguide-fed proves that THz antenna measurement and potential OTA measurement can get benefit from this geometry. Compared with THz antennas fed by the CPW-contact probe, this geometry is more flexible for the radiation pattern. And compared with standard gain horn antennas for OTA, the proposed antenna

has smaller dimensions, which means a smaller measurement distance and smaller test chambers.

Another advantage of the geometry is that the antenna chips can be replaceable to generate different far fields based on variable demands using a single probe housing. Different THz applications can be achieved using one waveguide-feed probe housing and antennas with different functions. THz antennas have a wide range of applications, including THz communications, spectroscopy, and imaging. For example, the quasi-Yagi chip in this work with WR2.2 probe housing is a good end-fire antenna for THz communication, and the TSA chip with the same probe housing can be used to receive signals at a certain direction, such as detection, since it has higher gain and less narrow main lobes than the quasi-Yagi antenna. The loop antenna can also be applied in the THz communication applications. Besides, a loop detector similar to the loop antenna in this work can be used for near electrical field detection because the antenna geometry in this work has the advantages for near field spectroscopy and imaging due to their small size and the capacity to precisely control movement. The spectroscopy and imaging by near field detection include security detection of food, explosives and drugs, wafer and circuit inspection for research, industry detection such as gas sensing, and medical spectroscopy and imaging.

5.2 Future Work

There are still some challenges with the micro-machined 3D antenna and THz antenna in this work. For the assembly of the 3D antenna, the hand assembly by tweezers, including soldering and assembling in a plastic holder, needs to be retired by a more precise method. For example, the silver epoxy soldering generates a piece of irregularly shaped conductor at the antenna feed. Wire bonding technology could be another integration solution to replace silver epoxy. Considering a more precise assembly, it is also worth having a high-precision holder. As shown in Chapter 3, the gap in the 3D printed plastic holder is 60 μm. Due to the resolution limit of the 3D printer in the lab, the actual width of the gap is over 200 μm. This 3D printing resolution results in the assembly error and folding error.

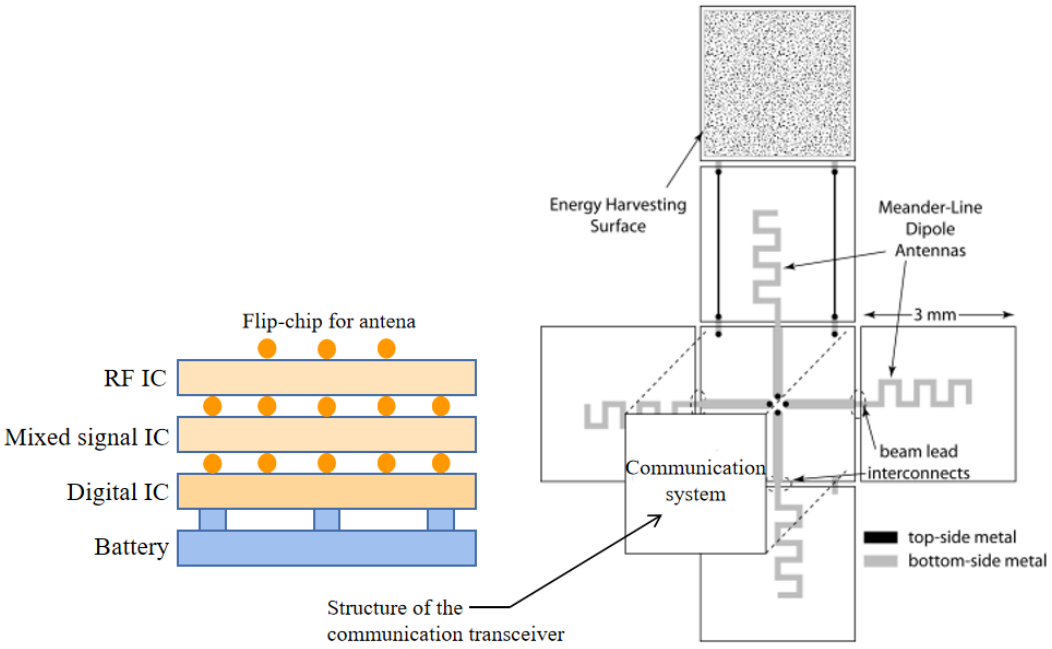

Figure 5.1 A conceptual drawing of the 3D antenna integrated with a communication system.

More efforts are needed to make on antenna geometry and antenna types. In some applications, an end-fire antenna with high directivity has better performance than the meandered-line dipole in

this work. In some communication systems, it is preferred to design an omnidirectional antenna transceiving signals in all directions. Thus, an antenna array and similar structure can have a better performance than a single antenna. Figure 5.1 shows a concept of a future design with the 3-mm cube structure. Also shown are the flip-chip mounted communication systems with RF IC and a 9-mm^2 solar cell for energy harvesting. In order to provide optimal impedances for both the PA and LNA/rectifier, two orthogonally polarized meander-line dipole antennas are integrated onto the cube faces. The beam-lead metal will be used for both electrical interconnects between adjacent sides of the cube as well as mechanical hinges to hold the sides together.

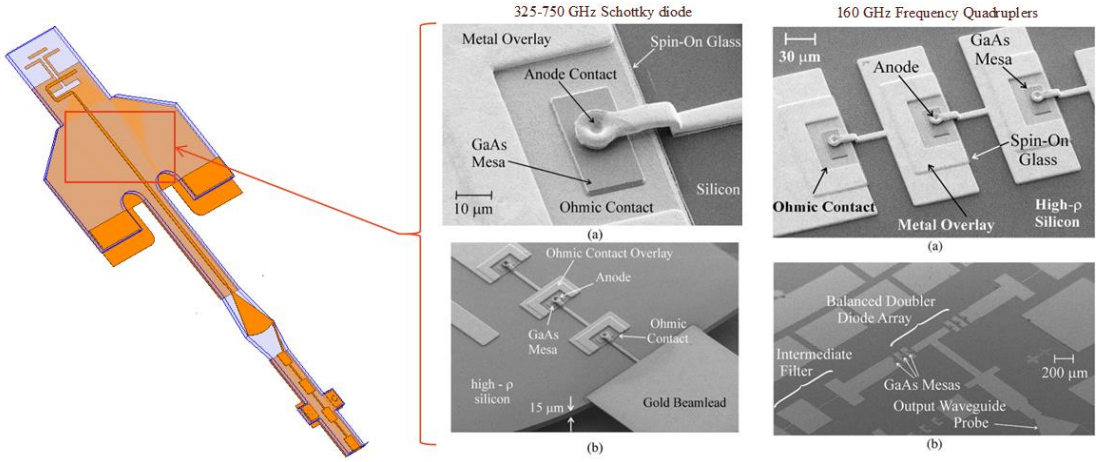

Figure 5.2 Possible integration with GaAs semiconductor devices.

This thesis also provides four antenna design, and the substrate removal has been proved as an efficient method of antenna performance improvement. Thus, it's worthy studying how the substrate removal effects the quasi-Yagi and electrically small loop antenna's performance. Besides, end-fire antenna array is more beneficial than a single end-fire antenna for gain increasing for some THz application, such as THz communication and detection.

One objective of this work is to create the antennas needed to extend the capabilities of existing wireless systems and provide them access to the submillimeter-wave and THz regions of the

spectrum. Thus, another primary task of this work is design and implementation of low-parasitic interfaces between THz antennas and GaAs submillimeter-wave front-ends. GaAs and other III-V semiconductor micro-machining have been researched at the University of Virginia for a number of years and have been used to implement a wide variety of systems and instruments for the submillimeter-wave spectrum. Two examples of integration GaAs devices onto silicon are shown in Figure 5.2, a free-standing directional coupler [221] supported at 300-500 GHz by a 10 μm thick micro-machined silicon membrane and an array of GaAs Schottky diodes bonded to a 15 μm thick silicon membrane and developed for applications at 160 GHz. The antenna chip in this work provides a mechanically-strong ultra-thin micro-machined membrane platform for the integration with GaAs and other III-V semiconductor materials. As shown in Figure 5.2, the antenna chip has enough available area between the antenna feed line and the E-plane probe for the integration and additional matching network.

Through various heterogeneous integration methods (wafer bonding and flip-chip techniques), GaAs and other III-V semiconductor materials can be transferred directly to the silicon, allowing the realization of fully-integrated submillimeter-wave and THz components. The integrated circuits are fabricated on mechanically-strong ultra-thin micro-machined high-resistivity silicon substrates, thus mitigating potential losses due to substrate modes. This integration method has low-parasitic and low-loss transmission lines and interconnects.

Bibliography

[1] IEEE Std 802.15.3d–2017, IEEE Standard for High Data Rate Wireless Multi-Media Networks–Amendment 2: 100 Gb/s Wireless Switched Point-to-Point Physical Layer, Oct. 2017, pp.1-55.

[2] K. Fukunaga, I. Hosako, I. N. Duling III, and M. Picollo, “Terahertz imaging system: a non-invasive technique for the analysis of paintings”, in O3A: Optics for Arts, Architecture, and Archaeology II, Proc. of SPIE, 2009, vol. 7391.

[3] M. A. Jamshed, A. Nauman, M. A. B. Abbasi and S. W. Kim, "Antenna Selection and Designing for THz Applications: Suitability and Performance Evaluation: A Survey," in IEEE Access, vol. 8, pp. 113246-113261, 2020.

[4] Y. He, Y. Chen, L. Zhang, S. Wong and Z. N. Chen, “An overview of terahertz antennas”, in China Communications, vol. 17, no. 7, pp. 124-165, July 2020.

[5] P. H. Siegel, “Terahertz technology”, IEEE Transactions on Microwave Theory and Techniques, vol. 50, no. 3, 2002, pp. 910-928.

[6] Kleine-Ostmann, T., Nagatsuma, T. A Review on Terahertz Communications Research. J Infrared Milli Terahz Waves 32, 143–171 (2011).

[7] FCC online table of frequency allocations. June, 2018. [Online]. Available: https: //transition.fcc.gov/oet/spectrum/table/fcctable.pdf.

[8] H. -J. Song and N. Lee, "Terahertz Communications: Challenges in the Next Decade," in IEEE Transactions on Terahertz Science and Technology, vol. 12, no. 2, pp. 105-117, March 2022.

[9] Tech. Dig. IEEE MTT-S International Microwave Symposium Workshop, WSN/WMD/WFE, Honolulu (2007).

[10] Sengupta, K., Nagatsuma, T. & Mittleman, D.M. Terahertz integrated electronic and hybrid electronic–photonic systems. Nat Electron 1, 622–635 (2018).

[11] G. Scalari et al., "Recent progress on long wavelength quantum cascade lasers between 1-2 THz," LEOS 2007 - IEEE Lasers and Electro-Optics Society Annual Meeting Conference Proceedings, 2007, pp. 755-756.

[12] Nagatsuma, Tadao, Hiroshi Ito, and Tadao Ishibashi. "High-power RF photodiodes and their applications." Laser & Photonics Reviews 3.1-2 (2009): 123-137.

[13] R. Sudo et al., "Pathological diagnosis of an experimental tumor using THz time-domain spectroscopy," 2009 34th International Conference on Infrared, Millimeter, and Terahertz Waves, 2009, pp. 1-2.

[14] Z. D. Taylor et al., "THz Medical Imaging: in vivo Hydration Sensing," in IEEE Transactions on Terahertz Science and Technology, vol. 1, no. 1, pp. 201-219, Sept. 2011.

[15] C. H. Zhang, G. F. Zhao, B. B. Jin, Y. Y. Hou, J. Chen, and P. H. Wu, “Terahertz Imaging on

Subcutaneous Tissues and Liver Inflamed by Liver Cancer Cells.pdf," Terahertz Science and Technology, 2012.

[16] M. Schirmer, M. Fujio, M. Minami, J. Miura, T. Araki, and T. Yasui, "Biomedical applications of a real-time terahertz color scanner," Optics Express, vol. 1, no. 2, pp. 354–366, 2010.

[17] Leahy-Hoppa, Megan R., Michael J. Fitch, and Robert Osiander. "Terahertz spectroscopy techniques for explosives detection." Analytical and bioanalytical chemistry 395.2 (2009): 247-257.

[18] Cooper et al., "THz Imaging Radar for Standoff Personnel Screening," IEEE Trans. Terahertz Sc. Tech., vol. 1, no. 1, Sept. 2011.

[19] Sulovska K, Lehocky M, "Characterization of plasma treated surfaces for food safety by terahertz spectroscopy," Proc. SPIE 9252, 2014.

[20] Walther, M., Fischer, B.M., Ortner, A. et al. Chemical sensing and imaging with pulsed terahertz radiation. Anal Bioanal Chem 397, 1009–1017 (2010).

[21] Naftaly, M.; Vieweg, N.; Deninger, A. Industrial Applications of Terahertz Sensing: State of Play. Sensors 2019, 19, 4203.

[22] Lee, DK., Kang, JH., Lee, JS. et al. Highly sensitive and selective sugar detection by terahertz nano-antennas. Sci Rep 5, 15459 (2015).

[23] G. J. Stacey, "THz Low Resolution Spectroscopy for Astronomy," in IEEE Transactions on Terahertz Science and Technology, vol. 1, no. 1, pp. 241-255, Sept. 2011.

[24] C. Kulesa. Terahertz spectroscopy for astronomy: From comets to cosmology. IEEE Transactions on Terahertz Science and Technology, 1(1):232–240, 2011.

[25] https://eventhorizontelescope.org/blog/astronomers-reveal-first-image-black-hole-heart-our-galaxy

[26] Y. Yang, A. Shutler and D. Grischkowsky, "Measurement of the transmission of the atmosphere from 0.2 to 2 THz," Optics Express, vol. 19, no. 9, pp. 8830-8838, 2011.

[27] A. Tessmann et al., "Terahertz Monolithic Integrated Circuits Based on Metamorphic HEMT Technology for Sensors and Communication," in IEEE Asia-Pacific Microwave Conference Proceedings, Seoul, South Korea, 2013.

[28] H. -J. Song, "Packages for Terahertz Electronics," in Proceedings of the IEEE, vol. 105, no. 6, pp. 1121-1138, June 2017, doi: 10.1109/JPROC.2016.2633547.

[29] I. Mehdi, J. V. Siles, C. Lee and E. Schlecht, "THz Diode Technology: Status, Prospects, and Applications," in Proceedings of the IEEE, vol. 105, no. 6, pp. 990-1007, June 2017, doi: 10.1109/JPROC.2017.2650235.

[30] Y. M. M. Antar, "Overview of some future trends in antenna research," 2017 34th National Radio Science Conference (NRSC), Alexandria, Egypt, 2017, pp. 1-1.

[31] Micromachining Primary Knowledge, Southwest Center for Microsystems Education (SCME).

[32] Venkata Ramesh Mamilla and Kommuri.Sai Chakradhar, "Micro Machining For Micro Electro Mechanical Systems," 3rd International Conference on Materials Processing and Characterisation (ICMPC 2014), 2014, pp. 147-154.

[33] Chang-Wook Baek et al., "A V-band micromachined 2-D beam-steering antenna driven by magnetic force with polymer-based hinges," in IEEE Transactions on Microwave Theory and Techniques, vol. 51, no. 1, pp. 325-331, Jan. 2003.

[34] C.-W. Baek, S. Song, C. Cheon, Y.-K. Kim and Y. Kwon, "2-D mechanical beam steering antenna fabricated using MEMS technology", IEEE MTT-S International Microwave Symposium Digest, San Francisco, CA, pp.211-214, 2001.

[35] C.-W. Baek, S. Song, J.-H. Park, S. Lee, J.-M. Kim, W. Choi, C. Cheon, Y.-K. Kim and Y. Kwon, "A V-band micromachined 2-D beam-steering antenna driven by magnetic force with polymer-based hinges", IEEE Transactions on Microwave Theory and Techniques, vol. 51, no. 1, pp. 325-331, Jan. 2003.

[36] G. Huff, J. Feng. D Zhang, J.T. Bernard, "A Novel Radiation Pattern and Frequency Reconfigurable Single Turn Square Spiral Microstrip Antenna," IEEE Microwave and Wireless Components Letters, Vol. 13, No. 2, February 2003, pp. 57-59.

[37] D. Kumar, A. S. Siddiqui, H. P. Singh, M. R. Tripathy and A. Sharma, "A Review: Techniques and Methodologies Adopted for Reconfigurable Antennas," 2018 International Conference on Sustainable Energy, Electronics, and Computing Systems (SEEMS), Greater Noida, India, 2018, pp. 1-6.

[38] J. Schoebel et al., "Design considerations and technology assessment of phased-array antenna systems with RF MEMS for automotive radar applications," in IEEE Transactions on Microwave Theory and Techniques, vol. 53, no. 6, pp. 1968-1975, June 2005.

[39] G.E. Ponchak, R.N. Simons, M. Scardelletti, "Microelectromechanical switches for phased array antennas," IEEE Antennas and Propagation Society International Symposium, Vol. 4, 16-21 July 2000, pp. 2230-2233.

[40] R. Sorrentino, "MEMS-based Reconfigurable Reflect Arrays", EurAAP and IET The Second European Conference on Antennas and Propagation (EuCAP 2007), Edinburgh, UK, Nov. 2007.

[41] L. Boccia, I. Russo, G. Amendola, and G. D. Massa, "Multilayer antennafilter antenna for beam-steering transmit-array applications," IEEE Trans. Microw. Theory Techn., vol. 60, no. 7, pp. 2287–2300, Jul. 2012.

[42] M. Sazegar, Y. Zheng, C. Kohler, H. Maune, M. Nikfalazar, J. R. Binder, and R. Jakoby, "Beam steering transmitarray using tunable frequency selective surface with integrated ferroelectric varactors," IEEE Trans. Antennas Propag., vol. 60, no. 12, pp. 5690–5699, Dec. 2012.

[43] X. Yang, B. Wang, Y. Zhang, "A Reconfigurable Hilbert Curve Patch Antenna," IEEE Antennas and Propagation Society International Symposium, Vol. 2B, 3-8 July 2005, pp. 613- 616.

[44] Symeon Nikolaou, Ramanan B, and Cesar Lugo, "Pattern and Frequency Reconfigurable Annular Slot Antenna Using PIN Diodes," IEEE TRANSACTIONS ON ANTENNAS AND PROPAGATION, VOL. 54, NO. 2, pp. 439-448.

[45] H. Chen, Z. Shi, L. Wu, D. Guo, "Frequency Reconfigurable Antenna with Micromechanical Patch, IEEE International Workshop on Anti-counterfeiting, Security, Identification," 16-18 April 2007, pp. 18-22.

[46] D. Sievenpiper, J. Schaffner, J. J. Lee and S. Livingston, "A steerable leaky-wave antenna using

a tunable impedance ground plane," in IEEE Antennas and Wireless Propagation Letters, vol. 1, pp. 179-182, 2002.

[47] Clark T.-C. Nguyen, L. P. B. Katehi and G. M. Rebeiz, "Micromachined devices for wireless communications," in Proceedings of the IEEE, vol. 86, no. 8, pp. 1756-1768, Aug. 1998.

[48] T. J. Ellis and G. M. Rebeiz, "MM-wave tapered slot antennas on micromachined photonic bandgap dielectrics," 1996 IEEE MTT-S International Microwave Symposium Digest, 1996, pp. 1157-1160.

[49] Y. P. Zhang, M. Sun, K. M. Chua, L. L. Wai and D. Liu, "Antenna-in-Package Design for Wirebond Interconnection to Highly Integrated 60-GHz Radios," in IEEE Transactions on Antennas and Propagation, vol. 57, no. 10, pp. 2842-2852, Oct. 2009.

[50] W. Cha et al., "Microfabricated Foldable Wings for Centimeter-Scale Microflyers," in Journal of Microelectromechanical Systems, vol. 29, no. 5, pp. 1127-1129, Oct. 2020.

[51] P. Gadfort and P. D. Franzon, "Millimeter-Scale True 3-D Antenna-in-Package Structures for Near-Field Power Transfer," in IEEE Transactions on Components, Packaging and Manufacturing Technology, vol. 4, no. 10, pp. 1574-1581, Oct. 2014.

[52] Theodore J. Reck et al., "Micromachined Probes for Submillimeter-Wave On-Wafer Measurements—Part II: RF Design and Characterization," in IEEE Transactions on Terahertz Science and Technology, vol. 1, no. 2, pp. 357-363, Nov. 2011.

[53] A. Artemenko, A. Maltsev, R. Maslennikov, A. Sevastyanov and V. Ssorin, "Design of wideband waveguide to microstrip transition for 60 GHz frequency band," 2011 41st European Microwave Conference, Manchester, UK, 2011, pp. 838-841.

[54] T. Tajima, et al., "300-GHz step-profiled corrugated horn antennas integrated in LTCC", IEEE Transactions on Antennas and Propagation, vol. 62, no. 11, 2014, pp. 5437-5444

[55] Y. Jiang, et al., "multi-layer corrugated terahertz horn antenna based on MEMS technology", Proc. 2015 IEEE MTT-S International Microwave Workshop Series on Advanced Materials and Processes for RF and THz Applications (IMWS-AMP), 2015, pp. 1-3.

[56] W. Hou, Z. Sun, Y. Jiang, Y. Liu and X. Lv, "A terahertz diagonal multi-layer horn antenna based on MEMS technology," 2015 IEEE MTT-S International Microwave Workshop Series on Advanced Materials and Processes for RF and THz Applications (IMWS-AMP), 2015, pp. 1-3.

[57] Y. He, Y. Chen, L. Zhang, S. Wong and Z. N. Chen, "An overview of terahertz antennas", in China Communications, vol. 17, no. 7, pp. 124-165, July 2020.

[58] N. Llombart, G. Chattopadhyay, A. Skalare, and I. Mehdi, "Novel terahertz antenna based on a silicon lens fed by a leaky wave enhanced waveguide," IEEE Transactions on Antennas and Propagation, vol. 59, no. 6, 2011, pp. 2160-2168.

[59] M. Alonso-DelPino, N. Llombart, G. Chattopadhyay, C. Lee, C. Jung-Kubiak, L. Jofre, and I. Mehdi, "Design guidelines for a terahertz silicon micro-lens antenna," IEEE Antennas and Wireless Propagation Letters, vol. 12, 2013, pp. 84-87.

[60] A. K. M. Z. Hossain, M. I. Ibrahimy, and S. M. A. Motakabber, "Integrated Si lens antenna with planar log spiral feed for THz band," Proc. 2014 International Conference on Computer and Communication Engineering, 2014, pp. 284-287.

[61] P. R. Smith, et al. "Subpicosecond photoconducting dipole antennas," IEEE Journal of Quantum Electronics, vol. 24, no. 2, 1988, pp. 255-260.

[62] A. Garufo, et al., "Norton equivalent circuit for pulsed photoconductive antennas-part I: theoretical model," IEEE Transactions on Antennas and Propagation, vol. 66, no. 4, 2018, pp. 1635-1645.

[63] A. Garufo, et al., "Norton equivalent circuit for pulsed photoconductive antennas-part II: experimental validation," IEEE Transactions on Antennas and Propagation, vol. 66, no. 4, 2018, pp. 1646-1659.

[64] Xu, L.J., Tong, F.C., Bai, X., et al.: 'Design of miniaturised on-chip slot antenna for THz detector in CMOS', IET Microw. Antennas Propag., 2018, 12, (8), pp. 1324–1331.

[65] D. Hou, Y. Xiong, W. Hong, W. L. Goh and J. Chen, "Silicon-based on-chip antenna design for millimeter-wave/THz applications," 2011 IEEE Electrical Design of Advanced Packaging and Systems Symposium (EDAPS), 2011, pp. 1-4.

[66] L. C. Paul, and M. M. Islam, "Proposal of wide bandwidth and very miniaturized having dimension of μm range slotted patch THz microstrip antenna using PBG substrate and DGS," Proc. 2017 20th International Conference of Computer and Information Technology, 2017, pp. 1-6.

[67] M. S. Rabbani and H. Ghafouri-Shiraz, "Liquid Crystalline Polymer Substrate-Based THz Microstrip Antenna Arrays for Medical Applications," in IEEE Antennas and Wireless Propagation Letters, vol. 16, pp. 1533-1536, 2017.

[68] A. Sharma, V.K. Dwivedi, G. Singh, THz rectangular microstrip patch antenna on multilayered substrate for advanced wireless communication systems, in: Progress in Electromagnetics Research Symposium, Beijing, China, March 23–27, 2009, pp. 627–631.

[69] Z. Chen et al., "A survey on terahertz communications," in China Communications, vol. 16, no. 2, pp. 1-35, Feb. 2019.

[70] Y. Yang, O. D. Gurbuz, and G. M. Rebeiz, "An eight-element 370-410-GHz phased-array transmitter in 45-nm CMOS SOI with peak EIRP of 8-8.5 dBm," IEEE Transactions on Microwave Theory and Techniques, vol. 64, no. 12, 2016, pp. 4241-4249.

[71] K. Guo, A. Standaert, P. Reynaert, "A 525-556 GHz radiating source with a dielectric lens antenna in 28-nm CMOS," IEEE Transactions on Terahertz Science and Technology, vol. 8, no. 3, 2018, pp. 340-349.

[72] M. H. Awida, S. H. Suleiman and A. E. Fathy, "Substrate-Integrated Cavity-Backed Patch Arrays: A Low-Cost Approach for Bandwidth Enhancement," in IEEE Transactions on Antennas and Propagation, vol. 59, no. 4, pp. 1155-1163, April 2011.

[73] K. L. Wong, Planar Antennas for Wireless Communications. New York: Wiley, 2003.

[74] D. Liao and K. Sarabandi, "Optimization of low-profile antennas for applications in unattended ground sensor networks," in Proc. IEEE Antennas Propag. Soc. Int. Symp., Jul. 2006, pp. 783–786.

[75] W. Hong and K. Sarabandi, "Design of low-profile omnidirectional antenna for ground sensor networks," in Proc. IEEE Antennas Propag. Soc. Int. Symp., Jun. 2007, pp. 6007–6010.

[76] A. Babar, L. Ukkonen, and L. Sydanheimo, "Dual UHF RFID band miniaturized multipurpose

planar antenna for compact wireless systems," in Proc. Int. Workshop Antenna Tech. (iWAT), Mar. 2010, pp. 1–4.

[77] S. Genovesi, S. Saponara, and A. Monorchio, "Parametric design of compact dual-frequency antennas for wireless sensor networks," IEEE Trans. Antennas Propag., vol. 59, no. 7, pp. 2619-2627, Jul. 2011.

[78] C. G. Kakoyiannis and P. Constantinou, "Co-design of antenna element and ground plane for printed monopoles embedded in wireless sensors," in Proc. IEEE Int. Conf. Sens. Technol. Applicat. (SENSORCOMM '08), Cap Esterel, France, Aug. 2008, pp. 413–418.

[79] Li, Zhuo, Taoran Le, "Rational Design of a Printable, Highly Conductive Silicone-based Electrically Conductive Adhesive for Stretchable Radio Frequency Antennas", Advanced Functional Materials 25, no. 3 (2015): 464-470.

[80] K. F. Brakora, J. Halloran and K. Sarabandi, "Design of 3-D Monolithic MMW Antennas Using Ceramic Stereolithography", in IEEE Transactions on Antennas and Propagation, vol. 55, no. 3, pp. 790-797, March 2007.

[81] B. Zhang et al., "Metallic 3-D Printed Antennas for Millimeter- and Submillimeter Wave Applications", in IEEE Transactions on Terahertz Science and Technology, vol. 6, no. 4, pp. 592-600, July 2016.

[82] T. Le et al., "A novel strain sensor based on 3D printing technology and 3D antenna design", 2015 IEEE 65th Electronic Components and Technology Conference (ECTC), San Diego, CA, USA, 2015, pp. 981-986.

[83] J. J. Adams et al., "Conformal printing of electrically small antennas on three-dimensional surfaces," Adv. Mater., vol. 23, no. 11, pp. 1335–1340, Mar. 2011.

[84] John Kimionis et al., "3D-Printed Origami Packaging with Inkjet-Printed Antennas for RF Harvesting Sensors," IEEE Transactions on Microwave Theory and Techniques, Vol. 63, No. 12, pp. 4521-4531, Dec 2015.

[85] Do Hanh, Ngan Bui et al., "Design and Measurement of 3D Flexible Antenna Diversity for Ambient RF Energy Scavenging in Indoor Scenarios," IEEE Access, Vol 7, pp.17033-17044, Jan 2019.

[86] Amin Enayati, Steven Brebels et al., "3D-Antenna-in-Package Solution for Microwave Wireless Sensor Network Nodes," IEEE Transactions on Antennas and Propagation, Vol 59, no. 10, pp. 3617-3623, Oct 2011.

[87] P. Gadfort and P. D. Franzon, "Millimeter-Scale True 3-D Antenna-in-Package Structures for Near-Field Power Transfer", in IEEE Transactions on Components, Packaging and Manufacturing Technology, vol. 4, no. 10, pp. 1574-1581, Oct. 2014.

[88] Standard ASTM. Standard Terminology for Additive Manufacturing Technologies. 2012.

[89] Alberto B, Luana B. Accuracy prediction in fused deposition modeling. Int J Adv Manuf Technol. 2014.

[90] Bremen S, Meiners W, Diatlov, "A. Selective laser melting: a manufacturing technology for the future", Laser Tech J. 2012;9: 33-38.

[91] H. Zhu, J. Gauthier and K. Wu, "Silicon Probe Measurement and Characterization in Sub-THz Range," in IEEE Transactions on Terahertz Science and Technology, vol. 10, no. 6, pp. 606-616.

[92] Theodore J. Reck et al., “Micromachined Probes for Submillimeter-Wave On-Wafer Measurements—Part II: RF Design and Characterization,” in IEEE Transactions on Terahertz Science and Technology, vol. 1, no. 2, pp. 357-363, Nov. 2011.

[93] A. U. Zaman, V. Vassilev, P. Kildal and H. Zirath, "Millimeter Wave E-Plane Transition from Waveguide to Microstrip Line with Large Substrate Size Related to MMIC Integration," in IEEE Microwave and Wireless Components Letters, vol. 26, no. 7, pp. 481-483, July 2016.

[94] D. W. Porterfield, "High-Efficiency Terahertz Frequency Triplers," 2007 IEEE/MTT-S International Microwave Symposium, 2007, pp. 337-340.

[95] J. L. Hesler and A. W. Lichtenberger, “THz Waveguide Couplers Using Quartz Micromachining,” in Proceedings of 21st International Symposium on Space Terahertz Technology (Oxford, UK, 2010), pp. 358–359.

[96] Ting-Huei Lin and Ruey-Beei Wu, "CPW to waveguide transition with tapered slotline probe," in IEEE Microwave and Wireless Components Letters, vol. 11, no. 7, pp. 314-316, July 2001.

[97] K. M. K. H. Leong et al., "A 340–380 GHz Integrated CB-CPW-to-Waveguide Transition for Sub Millimeter-Wave MMIC Packaging," in IEEE Microwave and Wireless Components Letters, vol. 19, no. 6, pp. 413-415, June 2009.

[98] T. Tajima, H. Song, H. Matsuzaki and M. Yaita, "LTCC-Integrated HH -Plane Bends for THz Antenna-in-Package Solution," in IEEE Microwave and Wireless Components Letters, vol. 27, no. 5, pp. 440-442, May 2017.

[99] Shuyu Bao et al., “A review of silicon-based wafer bonding processes, an approach to realize the monolithic integration of Si-CMOS and III–V-on-Si wafers,” Journal of Semiconductors, Volume 42, Number 2, 2021.

[100] X. Gu, D. Liu and B. Sadhu, "Packaging and Antenna Integration for Silicon-Based Millimeter-Wave Phased Arrays: 5G and Beyond," in IEEE Journal of Microwaves, vol. 1, no. 1, pp. 123-134, Jan. 2021.

[101] K. K. Samanta, D. Stephens, and I. D. Robertson, “Design and performance of a 60-GHz multichip module receiver employing substrate integrated waveguides,” IET J. Microwave Antenna Propagat., vol. 1, no. 5, pp. 961–967, Oct. 2007.

[102] Y. Yin, Z. Zhang, T. Kanar, S. Zihir and G. M. Rebeiz, "A 24-29.5 GHz 256-Element 5G Phased-Array with 65.5 dBm Peak EIRP and 256-QAM Modulation," 2020 IEEE/MTT-S International Microwave Symposium (IMS), 2020, pp. 687-690.

[103] X. Gu, D. Liu, C. Baks, J. Plouchart, W. Lee and A. Valdes-Garcia, "An Enhanced 64-Element Dual-Polarization Antenna Array Package for W-Band Communication and Imaging Applications," 2018 IEEE 68th Electronic Components and Technology Conference (ECTC).

[104] Heterogenous Integration Roadmap, 2019, ch. 8. [Online]. Available: https://eps.ieee.org/hir.

[105] J. M. Edwards and G. M. Rebeiz, "High-Efficiency Elliptical Slot Antennas with Quartz Superstrates for Silicon RFICs," in IEEE Transactions on Antennas and Propagation, vol. 60, no. 11, pp. 5010-5020, Nov. 2012.

[106] M. Rotaru. L. Ying, H. Kuruveettil, Y. Rui, A. P. Popov, and C. Chee-Parng, “Implementation of packaged integrated antenna with embedded front end for bluetooth applications,” IEEE Trans. Adv. Packag., vol. 31, no. 3, pp. 558–567, Aug. 2008.

[107] H. M. Cheema and A. Shamim, "The last barrier: on-chip antennas," in IEEE Microwave Magazine, vol. 14, no. 1, pp. 79-91, Jan.-Feb. 2013.

[108] H. J. Ng, R. Feger and D. Kissinger, "Scalable Mm-Wave 4-Channel Radar SoC with Vector Modulators and Demodulators for MIMO and Phased Array Applications," 2018 IEEE/MTT-S International Microwave Symposium - IMS, 2018, pp. 1472-1475.

[109] W. A. Ahmad et al., “Multimode W-band and D-band MIMO scalable radar platform,” IEEE Trans. Microw. Theory Techn., vol. 69, no. 1, pp. 1036–1047, Jan. 2021.

[110] A. Ali, J. Yun, M. Kucharski, H. J. Ng, D. Kissinger, and P. Colantonio, “220–360-GHz broadband frequency multiplier chains (×8) in 130-nm BiCMOS technology,” IEEE Trans. Microw. Theory Techn., vol. 68, no. 7, pp. 2701–2715, Jul. 2020.

[111] S. Yuan, A. Trasser, and H. Schumacher, ‘‘56 GHz bandwidth FMCW radar sensor with on-chip antennas in SiGe BiCMOS,’’ in IEEE MTT-S Int. Microw. Symp. Dig., Jun. 2014, pp. 1–4.

[112] M. R. Karim, X. Yang, and M. F. Shafifique, ‘‘On chip antenna measurement: A survey of challenges and recent trends,’’ IEEE Access, vol. 6, pp. 20320–20333, 2018.

[113] M. S. Khan, F. A. Tahir, and H. M. Cheema, ‘‘Design of bowtie-slot on-chip antenna backed with E-shaped FSS at 94 GHz,’’ in Proc. 10th Eur. Conf. Antennas Propag. (EuCAP), Apr. 2016, pp. 1–3.

[114] T. Hirano, N. Li, K. Okada, A. Matsuzawa, J. Hirokawa, M. Ando, T. Inoue, and H. Sakane, ‘‘Design of 60 GHz CMOS on-chip dipole antenna with 50% radiation efficiency by helium-3 ion irradiation,’’ in Proc. IEEE Conf. Antenna Meas. Appl. (CAMA), Nov. 2015, pp. 1–2.

[115] W. T. Khan, A. Cagri Ulusoy, G. Dufour, M. Kaynak, B. Tillack, J. D. Cressler, and J. Papapolymerou, ‘‘A D-band micromachined end-fire antenna in 130-nm SiGe BiCMOS technology,’’ IEEE Trans. Antennas Propag., vol. 63, no. 6, pp. 2449–2459, Jun. 2015.

[116] H. J. Ng, J. Wessel, D. Genschow, R. Wang, Y. Sun, and D. Kissinger, ‘‘Miniaturized 122 GHz system-on-chip radar sensor with on-chip antennas utilizing a novel antenna design approach,’’ in IEEE MTT-S Int. Microw. Symp. Dig., May 2016, pp. 1–4.

[117] S. Pan, F. Caster, P. Heydari, and F. Capolino, ‘‘A 94-GHz extremely thin metasurface-based BiCMOS on-chip antenna,’’ IEEE Trans. Antennas Propag., vol. 62, no. 9, pp. 4439–4451, Sep. 2014.

[118] R. Karim, A. Iftikhar and R. Ramzan, "Performance-Issues-Mitigation-Techniques for On-Chip-Antennas – Recent Developments in RF, MM-Wave, and Thz Bands With Future Directions," in IEEE Access, vol. 8, pp. 219577-219610.

[119] Y. Zhang, Y. Gu, V. Vlatkovic, and X.Wang, “Progress of smart sensor and smart sensor networks,” in Proc. 5th World Congress on Intelligent Control and Automation (WCICA 2004), Jun. 2004, vol. 4, pp. 3600–3606.

[120] C. Townsend and S. Arms, “Wireless sensor networks: Principles and applications,” in Sensor Technology Handbook, J. S.Wilson, Ed. Oxford, U.K.: Elsevier Inc., 2005, ch. 22.

[121] K. L. Wong, Planar Antennas for Wireless Communications. New York: Wiley, 2003.

[122] D. Liao and K. Sarabandi, “Optimization of low-profile antennas for applications in unattended ground sensor networks,” in Proc. IEEE Antennas Propag. Soc. Int. Symp., Jul. 2006, pp. 783–786.

[123] W. Hong and K. Sarabandi, “Design of low-profile omnidirectional antenna for ground sensor networks,” in Proc. IEEE Antennas Propag. Soc. Int. Symp., Jun. 2007, pp. 6007–6010.

[124] A. Babar, L. Ukkonen, and L. Sydanheimo, “Dual UHF RFID band miniaturized multipurpose planar antenna for compact wireless systems,” in Proc. Int. Workshop Antenna Tech. (iWAT), Mar. 2010, pp. 1–4.

[125] S. Genovesi, S. Saponara, and A. Monorchio, “Parametric design of compact dual-frequency antennas for wireless sensor networks,” IEEE Trans. Antennas Propag., vol. 59, no. 7, pp. 2619–2627, Jul. 2011.

[126] C. G. Kakoyiannis and P. Constantinou, “Co-design of antenna element and ground plane for printed monopoles embedded in wireless sensors,” in Proc. IEEE Int. Conf. Sens. Technol. Applicat. (SENSORCOMM ’08), Cap Esterel, France, Aug. 2008, pp. 413–418.

[127] Fraga-Lamas, P.; Fernández-Caramés, T.M.; Suárez-Albela, M.; Castedo, L.; González-López, M. A Review on Internet of Things for Defense and Public Safety. Sensors 2016, 16, 1644.

[128] Lee, H.; Yoo, S.; Kim, Y.W. An energy management framework for smart factory based on context-awareness. In Proceedings of the 18th International Conference on Advanced Communication Technology (ICACT), Pyeongchang, Korea, 31 January–2 February 2016; pp. 685–688.

[129] Lee, C.H.; Chung, C.W. RFID data processing in supply chain management using a path encoding scheme. IEEE Trans. Knowl. Data Eng. 2011, 23, 742–758.

[130] Jaideep Kaur, Kamaljit Kaur,"Internet of Things: A Review on Technologies, Architecture, Challenges, Applications, Future Trends", International Journal of Computer Network and Information Security(IJCNIS), Vol.9, No.4, pp. 57-70, 2017.

[131] Samsung ARTIK. Accessed: Sep. 28, 2018. [Online]. Available: https:// www.artik.io/modules/

[132] E. Upton and G. Halfacree, Raspberry Pi User Guide. Hoboken, NJ, USA: Wiley, 2014.

[133] Y. Wang, H. -y. Tsao, N. Sauber, R. M. Weikle, A. W. Lichtenberger and N. S. Barker, "Micro-machined 3D Cube Antenna for X-Band Communication ICs," 2021 IEEE 21st Annual Wireless and Microwave Technology Conference (WAMICON), 2021, pp. 1-3.

[134] M. Fallahpour and R. Zoughi, “Antenna Miniaturization Techniques: A Review of Topology- and Material-Based Methods”, in IEEE Antennas and Propagation Magazine, vol. 60, no. 1, pp. 38-50, Feb. 2018.

[135] G. Marrocco, “Gain-optimized self-resonant meander line antennas for RFID applications”, in IEEE Antennas and Wireless Propagation Letters, vol. 2, pp. 302-305, 2003.

[136] S. R. Best, “On the resonant properties of the Koch fractal and other wire monopole antennas”, in IEEE Antennas and Wireless Propagation Letters, vol. 1, pp. 74-76, 2002.

[137] Ibrahim T. Nassar, Thomas M. Weller, “Development of Novel 3-D Cube Antennas for

Compact Wireless Sensor Nodes", IEEE Transactions on Antennas and Propagation, Vol. 60, No. 2, Feb 2012.

[138] W. Hong and K. Sarabandi, "Design of low-profile omnidirectional antenna for ground sensor networks," in Proc. IEEE Antennas Propag. Soc. Int. Symp., Jun. 2007, pp. 6007–6010.

[139] Chunhu Zhang, " Development of Single-ended and Balun Integrated Probes for THz Applications ", PhD thesis, University of Virginia, 2014.

[140] M. Shearn, X. Sun, M. D. Henry, A. Yariv, and A. Scherer, "Advanced plasma processing: etching, deposition, and wafer bonding techniques for semiconductor applications," 2010.

[141] H. A. Wheeler, "The radiansphere around a small antenna," Proc. IRE, vol. 47, No. 8, pp. 1325–1331, Aug 1959.

[142] Agahi, Darioush, and William Domino. "Efficiency measurements of portable-handset antennas using the wheeler cap." Applied Microwave and Wireless 12.6 (2000): 34-43.

[143] García-García, Quiterio. "Patch-antenna efficiency based on Wheeler cap and measured Q factor." Microwave and Optical Technology Letters 40.2 (2004): 132-142.

[144] T. Le et al., "A novel strain sensor based on 3D printing technology and 3D antenna design", 2015 IEEE 65th Electronic Components and Technology Conference (ECTC), San Diego, CA, USA, 2015, pp. 981-986.

[145] J. J. Adams et al., "Conformal printing of electrically small antennas on three-dimensional surfaces," Adv. Mater., vol. 23, no. 11, pp. 1335–1340, Mar. 2011.

[146] John Kimionis et al., "3D-Printed Origami Packaging with Inkjet-Printed Antennas for RF Harvesting Sensors," IEEE Transactions on Microwave Theory and Techniques, Vol. 63, No. 12, pp. 4521-4531, Dec 2015.

[147] Do Hanh, Ngan Bui et al., "Design and Measurement of 3D Flexible Antenna Diversity for Ambient RF Energy Scavenging in Indoor Scenarios," IEEE Access, Vol 7, pp.17033-17044, Jan 2019.

[148] Amin Enayati, Steven Brebels et al., "3D-Antenna-in-Package Solution for Microwave Wireless Sensor Network Nodes," IEEE Transactions on Antennas and Propagation, Vol 59, no. 10, PP. 3617-3623, Oct 2011.

[149] P. Gadfort and P. D. Franzon, "Millimeter-Scale True 3-D Antenna-in-Package Structures for Near-Field Power Transfer", in IEEE Transactions on Components, Packaging and Manufacturing Technology, vol. 4, no. 10, pp. 1574-1581, Oct. 2014.

[150] Ibrahim T. Nassar, Thomas M. Weller, "Development of Novel 3-D Cube Antennas for Compact Wireless Sensor Nodes", IEEE Transactions on Antennas and Propagation, Vol. 60, No. 2, Feb 2012.

[151] Standard ASTM. Standard Terminology for Additive Manufacturing Technologies. 2012.

[152] S. Pan, F. Caster, P. Heydari, and F. Capolino, ''A 94-GHz extremely thin metasurface-based BiCMOS on-chip antenna,'' IEEE Trans. Antennas Propag., vol. 62, no. 9, pp. 4439–4451, Sep. 2014.

[153] R. Karim, A. Iftikhar and R. Ramzan, "Performance-Issues-Mitigation-Techniques for On-Chip-Antennas Recent Developments in RF, MM-Wave, and THz Bands With Future Directions,"

in IEEE Access, vol. 8, pp. 219577-219610, 2020.

[154] N. Scott Barker, M. Bauwens, A. Lichtenberger and R. Weikle, "Silicon-on-Insulator Substrates as a Micromachining Platform for Advanced Terahertz Circuits," in Proceedings of the IEEE, vol. 105, no. 6, pp. 1105-1120, June 2017.

[155] D. B. Rutledge, D. P. Neikirk and D. P. Kasilingam, "Integrated circuit antennas" in Infrared and Millimeter-Waves, New York: Academic Press, vol. 10, pp. 1-90, 1983.

[156] Constantine A. Balanis, "Advanced Engineering Electromagnetics", pp. 408-417, 2012.

[157] N. Llombart et al., "Silicon Micromachined Lens Antenna for THz Integrated Heterodyne Arrays," in IEEE Transactions on Terahertz Science and Technology, vol. 3, no. 5, pp. 515-523, Sept. 2013.

[158] S. F. Jilani and A. Alomainy, "Planar millimeter-wave antenna on low-cost flexible PET substrate for 5G applications," 2016 10th European Conference on Antennas and Propagation (EuCAP), 2016, pp. 1-3.

[159] M. J. Al-Hasan, T. A. Denidni and A. R. Sebak, "Millimeter-Wave Compact EBG Structure for Mutual Coupling Reduction Applications," in IEEE Transactions on Antennas and Propagation, vol. 63, no. 2, pp. 823-828, Feb. 2015.

[160] Y. -S. Huang, L. Zhou, J. -F. Mao and Q. Xu, "A W-band High Radiation Efficiency with BCB-air Cavity-backed Antenna Based on Through Silicon Ring Trench," in IEEE Antennas and Wireless Propagation Letters, 2022.

[161] K. Van Caekenberghe et al., "A 2–40 GHz Probe Station Based Setup for On-Wafer Antenna Measurements," in IEEE Transactions on Antennas and Propagation, vol. 56, no. 10, pp. 3241-3247, Oct. 2008.

[162] L. Boehm, M. Hehl and C. Waldschmidt, "Influence of the wafer chuck on integrated antenna measurements," 2016 German Microwave Conference (GeMiC), 2016, pp. 274-277.

[163] A. Bisognin et al., "Probe-fed measurement system for F-band antennas," The 8th European Conference on Antennas and Propagation (EuCAP 2014), 2014, pp. 722-726.

[164] J. Qian, M. Tang, Q. Chen, Y. -P. Zhang and J. Mao, "Integration of S /Ka/ DD -Band Antennas in LTCC With a Cylindrical Radome for Triband Applications," in IEEE Transactions on Antennas and Propagation, vol. 67, no. 9, pp. 5781-5789, Sept. 2019.

[165] H. Gulan et al., "Probe based antenna measurements up to 325 GHz for upcoming millimeter-wave applications," 2013 International Workshop on Antenna Technology (iWAT), 2013, pp. 228-231.

[166] Z. Zheng, Y. Zhang, L. Shi, L. Wu and J. -F. Mao, "An Overview of Probe-Based Millimeter-Wave/Terahertz Far-Field Antenna Measurement Setups [Measurements Corner]," in IEEE Antennas and Propagation Magazine, vol. 63, no. 2, pp. 63-118, April 2021.

[167] J. B. Muldavin and G. M. Rebeiz, "Millimeter-wave tapered-slot antennas on synthesized low permittivity substrates," in IEEE Transactions on Antennas and Propagation, vol. 47, no. 8, pp. 1276-1280, Aug. 1999.

[168] J. B. Rizk and G. M. Rebeiz, "Millimeter-wave Fermi tapered slot antennas on micromachined

silicon substrates," in IEEE Transactions on Antennas and Propagation, vol. 50, no. 3, pp. 379-383, March 2002.

[169] C. Zhang et al., "A Differential Probe with Integrated Balun for On-wafer Measurements in the WR-3.4 (220-330 GHz) Waveguide Band," 2019 IEEE MTT-S International Microwave Symposium (IMS), 2019, pp. 1269-1271.

[170] X. Li, T. Kasai, S. Nakao, H. Tanaka, T. Ando, M. Shikida, and K. Sato, “Measurement for fracture toughness of single crystal silicon film with tensile test,” Sensors and Actuators A: Physical, vol. 119, no. 1, pp. 229 – 235, 2005.

[171] K. Hjort, J. Soderkvist, and J. A. Schweitz, “Gallium arsenide as a mechanical material,” Journal of Micromechanics and Microengineering, vol. 4, no. 1, p. 1, 1994.

[172] J. S. Danel and G. Delapierre, “Quartz: a material for microdevices,” Journal of Micromechanics and Microengineering, vol. 1, no. 4, p. 187, 1991.

[173] Theodore Reck, "Submillimeter Wavelength Metrology Components", PhD thesis, University of Virginia, 2010.

[174] J. Huang, ‘‘Planar microstrip Yagi array antenna,’’ in Proc. Dig. Antennas Propag. Soc. Int. Symp., vol. 2, Jan. 2003, pp. 894–897.

[175] Huadong Guo and Wen Geyi, “Design of Yagi-Uda Antenna with Multiple Driven Elements”, Progress In Electromagnetics Research C, Vol. 92, 101-112, 2019.

[176] Cheng, D. K. and C. A. Chen, "Optimum element spacings for Yagi-Uda arrays," IEEE Trans. Antennas Propag., Vol. 21, No. 5, 615-623, Sep. 1973.

[177] Chen, C. A. and D. K. Cheng, "Optimum element lengths for Yagi-Uda arrays," IEEE Trans. Antennas Propag., Vol. 23, No. 1, 8-15, Jan. 1975.

[178] B. Park, M. Jeong and S. Park, "A Miniaturized Microstrip-to-Coplanar-Strip Transition Loaded with Artificial Transmission Lines and 2.4-GHz Antenna Application," in IEEE Antennas and Wireless Propagation Letters, vol. 13, pp. 1486-1489, 2014.

[179] A. Hosseini and F. De Flaviis, "A CPW-fed single-layer printed Quasi-Yagia antenna for 60 GHz wireless communication systems," 2014 IEEE Antennas and Propagation Society International Symposium (APSURSI), 2014, pp. 103-104.

[180] H. K. Kan, R. B. Waterhouse, A. M. Abbosh and M. E. Bialkowski, "Simple Broadband Planar CPW-Fed Quasi-Yagi Antenna," in IEEE Antennas and Wireless Propagation Letters, vol. 6, pp. 18-20, 2007.

[181] P. Wang and C. Cui, "Small-size CPW-fed Quasi-Yagi antenna with round-ended bow-tie CPW-to-slotline transition," 2016 IEEE International Symposium on Radio-Frequency Integration Technology (RFIT), 2016, pp. 1-3.

[182] S. X. Ta, J. J. Han, H. Choo and I. Park, "A wideband double dipole quasi-Yagi antenna using a microstrip-slotline transition feed," 2012 IEEE International Workshop on Antenna Technology (iWAT), 2012, pp. 84-87.

[183] T. Johansen and V. Krozer, "Analysis and design of lumped element Marchand baluns," MIKON 2008 - 17th International Conference on Microwaves, Radar and Wireless Communications,

2008, pp. 1-4.

[184] D. Prieto, J. C. Cayrout, J. L. Cazaux, T. Parra and J. Graffeuil, "CPS structure potentialities for MMICs: a CPS/CPW transition and a bias network," 1998 IEEE MTT-S International Microwave Symposium Digest (Cat. No.98CH36192), 1998, pp. 111-114 vol.1.

[185] K.-P. Ma, Y. Qian and T. Itoh, "Analysis and applications of a new CPW–slotline transition", IEEE Trans. Microw. Theory Tech., vol. 47, no. 4, pp. 426-432, Apr. 1999.

[186] J. B. Rizk and G. M. Rebeiz, "Millimeter-wave Fermi tapered slot antennas on micromachined silicon substrates," in IEEE Transactions on Antennas and Propagation, vol. 50, no. 3, pp. 379-383, March 2002.

[187] P. J. Gibson, "The Vivaldi aerial," in Proc. 9th Eur. Microwave Conf., Brighton, U.K., June 1979, pp. 101–105.

[188] S. Sugawara, Y. Maita, K. Adachi, K. Mori, and K. Mizuno, "A mm-wave tapered slot antenna with improved radiation pattern," in IEEE MTT Int. Microwave Symp., Denver, CO, June 1997, pp. 959–962.

[189] S. Sugawara, Y. Maita, K. Adachi, K. Mori and K. Mizuno, "A mm-wave tapered slot antenna with improved radiation pattern," 1997 IEEE MTT-S International Microwave Symposium Digest, 1997, pp. 959-962 vol.2.

[190] S. Yngvesson, T. L. Korzeniowski, Y. S. Kim, E. L. Kollberg and J. F. Johansson, "The Tapered Slot Antenna - A New Integrated Element for MM Wave Applications", IEEE Trans. Microwave Theory and Tech., vol. 37, no. 2, pp. 365-374, Feb.

[191] K. S. Yngvesson, D. H. Schaubert, T. L. Korzeniowski, E. L. Kollberg, T. Thungren and J. F. Johansson, "Endfire Tapered Slot Antennas on Dielectric Substrates", IEEE Trans. Antennas Propagat., vol. 33, no. 12, pp. 1392-1400, Dec. 1985.

[192] H. Wang et al., "Small-Size Reconfigurable Loop Antenna for Mobile Phone Applications," in IEEE Access, vol. 4, pp. 5179-5186, 2016.

[193] A. W. Damaj, H. M. El Misilmani and S. A. Chahine, "Implantable Antennas for Biomedical Applications: An Overview on Alternative Antenna Design Methods and Challenges," 2018 International Conference on High Performance Computing & Simulation (HPCS), 2018, pp. 31-37.

[194] Y. -L. Ban, Y. -F. Qiang, Z. Chen, K. Kang and J. -H. Guo, "A Dual-Loop Antenna Design for Hepta-Band WWAN/LTE Metal-Rimmed Smartphone Applications," in IEEE Transactions on Antennas and Propagation, vol. 63, no. 1, pp. 48-58, Jan. 2015.

[195] M. Kanda, "Standard probes for electromagnetic field measurements," in IEEE Transactions on Antennas and Propagation, vol. 41, no. 10, pp. 1349-1364, Oct. 1993.

[196] Ramo, Simon, John R. Whinnery, and Theodore Van Duzer. Fields and waves in communication electronics. John Wiley & Sons, 1994.

[197] Volakis, John L. Antenna engineering handbook. McGraw-Hill Education, 2007.

[198] Sultan, Kamel S., Esmat A. Abdallah, and Hadia El Hennawy. "A multiple-input-multiple-output on-chip Quasi-Yagi-Uda antenna for multigigabit communications: Preliminary study." Engineering Reports 2.3 (2020).

[199] M. Sun and Y. P. Zhang, "100-GHz Quasi-Yagi Antenna in Silicon Technology," in IEEE Electron Device Letters, vol. 28, no. 5, pp. 455-457, May 2007, doi: 10.1109/LED.2007.895447.

[200] M. Inoue, M. Hodono, S. Horiguchi, K. Arakawa, M. Fujita, and T. Nagatsuma, ‘‘Ultra-broadband terahertz receivers using polymer substrate,’’ IEEE Transactions on Terahertz Science and Tech., vol. 4, no. 2, pp. 225–231, Mar. 2014.

[201] M. Oka, M. Inoue, N. Nagaoka, M. Hodono, M. Fujita, and T. Nagatsuma, ‘‘300-GHz-band receivers using tapered slot array antenna on polymer substrate,’’ IEICE Trans. Electron. (Japanese edition), vol. J100-C, no. 1 pp. 1--7, Jan. 2017.

[202] S. Li, T. Chi, Y. Wang and H. Wang, "A Millimeter-Wave Dual-Feed Square Loop Antenna for 5G Communications," in IEEE Transactions on Antennas and Propagation, vol. 65, no. 12, pp. 6317-6328, Dec. 2017.

[203] P. -F. Zhao, Q. Li, H. -D. Lu, B. Li, Y. Liu and X. Lv, "Design of terahertz waveguide-fed antipodal hyperbolic-sine tapered slot antenna based on silicon micromachine," 2015 IEEE International Conference on Computational Electromagnetics, 2015, pp. 358-360.

[204] Wang, Xu. "Uncooled antenna-coupled terahertz thermal detector using CMOS process." Microwave and Optical Technology Letters 63.1 (2021): 235-241.

[205] A. H. Naqvi, J. Park, C. Baek and S. Lim, "Via-Monopole Based Quasi Yagi-Uda Antenna for W-Band Applications using Through Glass Silicon via (TGSV) Technology," in IEEE Access, vol. 8, pp. 9513-9519, 2020.

[206] W. T. Khan et al., "A D-Band Micromachined End-Fire Antenna in 130-nm SiGe BiCMOS Technology," in IEEE Transactions on Antennas and Propagation, vol. 63, no. 6, pp. 2449-2459, June 2015.

[207] Le Huu Truong et al., “A high-performance 94 GHz planar Quasi-Yagi antenna on GaAs substrate”, Microwave Opt Technol Lett 51: 2396–2400, 2009.

[208] S. Erdogan and M. Swaminathan, "D-band Quasi-Yagi Antenna in Glass-based Package," 2021 IEEE MTT-S International Microwave and RF Conference (IMARC), 2021, pp. 1-4.

[209] D. Neculoiu et al., "Membrane-supported Yagi-Uda MM-Wave antennas," 2006 First European Conference on Antennas and Propagation, 2006, pp. 1-5.

[210] A. Mirbeik-Sabzevari, S. Li, E. Garay, H. Nguyen, H. Wang and N. Tavassolian, " W-Band Micromachined Antipodal Vivaldi Antenna Using SIW and CPW Structures," in IEEE Transactions on Antennas and Propagation, vol. 66, no. 11, pp. 6352-6357, Nov. 2018.

[211] C. Jarufe et al., "Optimized Corrugated Tapered Slot Antenna for mm-Wave Applications," in IEEE Transactions on Antennas and Propagation, vol. 66, no. 3, pp. 1227-1235, March 2018.

[212] N. Jastram and D. S. Filipović, "Wideband Millimeter-Wave Surface Micromachined Tapered Slot Antenna," in IEEE Antennas and Wireless Propagation Letters, vol. 13, pp. 285-288, 2014.

[213] J. B. Muldavin and G. M. Rebeiz, "Millimeter-wave tapered-slot antennas on synthesized low permittivity substrates," in IEEE Transactions on Antennas and Propagation, vol. 47, no. 8, pp. 1276-1280, Aug. 1999.

[214] J. B. Rizk and G. M. Rebeiz, "Millimeter-wave Fermi tapered slot antennas on micromachined

silicon substrates," in IEEE Transactions on Antennas and Propagation, vol. 50, no. 3, pp. 379-383, March 2002.

[215] X. -D. Deng, Y. Li, W. Wu and Y. -Z. Xiong, "340-GHz SIW Cavity-Backed Magnetic Rectangular Slot Loop Antennas and Arrays in Silicon Technology," in IEEE Transactions on Antennas and Propagation, vol. 63, no. 12, pp. 5272-5279, Dec. 2015.

[216] H. Zhu, X. Li, Z. Qi and J. Xiao, "A 320 GHz Octagonal Shorted Annular Ring On-Chip Antenna Array," in IEEE Access, vol. 8, pp. 84282-84289, 2020.

[217] E. Ojefors, H. Kratz, K. Grenier, R. Plana and A. Rydberg, "Micromachined Loop Antennas on Low Resistivity Silicon Substrates," in IEEE Transactions on Antennas and Propagation, vol. 54, no. 12, pp. 3593-3601, Dec. 2006.

[218] F. Golcuk, O. D. Gurbuz and G. M. Rebeiz, "A 0.39–0.44 THz 2x4 Amplifier-Quadrupler Array with Peak EIRP of 3–4 dBm," in IEEE Transactions on Microwave Theory and Techniques, vol. 61, no. 12, pp. 4483-4491, Dec. 2013.

[219] S. Jameson, E. Halpern and E. Socher, "20.4 A 300GHz wirelessly locked 2×3 array radiating 5.4dBm with 5.1% DC-to-RF efficiency in 65nm CMOS," 2016 IEEE International Solid-State Circuits Conference (ISSCC), 2016, pp. 348-349.

[220] "Introduction to coaxial cables", https://www.rfmicrowave.com

[221] R. M. Weikle et al., "Submillimeter-Wave Schottky Diodes based on Heterogeneous Integration of GaAs onto Silicon," 2019 United States National Committee of URSI National Radio Science Meeting (USNC-URSI NRSM), 2019, pp. 1-2.

[222] L. Xie et al., "Micromachined probes with integrated GaAs Schottky diodes for on-wafer temperature sensing," 2018 IEEE International Instrumentation and Measurement Technology Conference (I2MTC), 2018, pp. 1-6.